Geological and Mineral Potential Mapping by Geoscience Data Integration

Sentayehu Zewdie Mekonnen
April, 2008

Geological and Mineral Potential Mapping by Geoscience Data Integration

by

Sentayehu Zewdie Mekonnen

Thesis submitted to the International Institute for Geo-information Science and Earth Observation in partial fulfilment of the requirements for the degree of Master of Science in Geo-information Science and Earth Observation, Specialisation: Earth Science Data Provision

Supervisors:
Dr. T. Woldai (1st Supervisor)
Dr. E. J. M. Carranza (2nd Supervisor)

Thesis Assessment Board

Prof. Dr.F. vander Meer (Chairman)
Dr. Ir. C. Mannaerts (External Examiner)
Dr. T. Woldai (1st Supervisor)
Dr. E. J. M. Carranza (2nd Supervisor)

Observer :
Drs T.M. Loran (Program Director, AES)

INTERNATIONAL INSTITUTE FOR GEO-INFORMATION SCIENCE AND EARTH OBSERVATION
ENSCHEDE, THE NETHERLANDS

Disclaimer

This document describes work undertaken as part of a programme of study at the International Institute for Geo-information Science and Earth Observation. All views and opinions expressed therein remain the sole responsibility of the author, and do not necessarily represent those of the institute.

Abstract

Spatial data integration and analysis for updating geological map and predicting mineral potential were carried out on the available analogue and digital remote sensing datasets of Magondi Belt, Zimbabwe. In the search for mineral potential areas, accurate and up-to-date geological maps are essential as it represents the most basic information for directing exploration activities. To this end, the existing geological map of the study area, which was published in 1961, is too old to extract up-to-date information for mineral exploration. However, Geological Survey of Zimbabwe (GSZ) has acquired several exploration datasets from different exploration and mining companies. The problem is there is no proper integration of the exploratory datasets in order to update the geological map and prospect and delineate new exploration targets. Moreover, modern exploration techniques and new tools like RS and GIS have not been applied in order to integrate the diverse geological datasets to predict mineral potential map for certain types of mineral deposits in the Magondi Belt. The main objective of this research was to integrate these datasets to update the geological map and produce mineral potential map of the study area. In this research, the various datasets were processed, integrated and modelled using GIS and remote sensing techniques. Landsat TM and ASTER images were interpreted and classified to delineate major lithological units and structural features. Lineaments were interpreted from DEM and vertical derivative total field magnetics. Lithological interpretations made on analytical signal total field magnetics were compiled with results of interpreted multispectral images to produce updated geological map. The map was validated and a total accuracy of 76% was obtained.

Estimation and integration of spatial evidences were conducted in the southern portion of the study area. Evidential belief functions (EBFs) were used to quantify the spatial association between Cu deposit and geological features. Deposit recognition criteria were the basis for extracting spatial evidences based on the characteristic features of strata-bound Cu-Ag-Au mineralization in the study area. The geochemical copper anomaly map, which delineated the potential zone of mineralization, was used as one spatial evidence. Among the lithological units, arkose and dolomite were important spatial evidence. The linear structure, NW trending faults and magnetic anomalies have similar spatial evidence to copper mineralization. The belief function maps were integrated and classified to produce a binary predictive copper potential map. Validations conducted on the predictive map without magnetic evidence indicates that the favourable potential zone correctly delineate 12% of the Cu-anomaly, 58% of the ‘model’ and 60% of the ‘validation’ deposit. Validation conducted on predictive map using magnetic evidences improved the spatial coverage of the favourability zone by 0.3% and delineated 19% of the Cu-anomaly. These indicate that integration of all spatial evidences give satisfactory result for mapping mineral potential of the study area. The result implies the usefulness of the model for further exploration of undiscovered strata-bound copper deposit in the study area.

Acknowledgements

I would like to thank the International Institute for Geo-information Science and Earth Observation (ITC) for offering me the financial and academic support to follow the masters program. The Geological Survey of Ethiopia (GSE) is equally thanked for endorsing my application for ITC grant. I am very grateful to Dr T. Woldai, first supervisor, for his devoted guidance, constructive comments, technical support and advice from the very stage of the research proposal to the final stage of completing this thesis. His encouragement and help during my critical health problem is unforgettable. I am indebted to Dr. E.J.M. Carranza, second supervisor for his critical comment, invaluable suggestions, guidance and helpful technical support through out the thesis period.

I am indebted and grateful to Drs. Tom Loran, Program Director of AES for all his unreserved support and help during my problem and extending my studies for the period I spent in hospital. Great thanks and special appreciation goes to Drs. J. B. de Smeth, whose encouragement, help, kindness and support during my heath problem and studies is invaluable. Great thanks go to all my instructors for giving me enormous knowledge during my MSc. study. I also extend my sincere gratitude to all AES MSc students especially my closest friends not listed her but known for their moral, social and academic support and assistance during my stay in ITC.

I would like to forward my thanks to the administrative staff especially the Facility and ITC Hotel management for providing me the necessary facility.

Table of contents

List of figures

List of tables

1. Introduction

1.1. Research background

Reliable geoscience information in the form of geological and mineral potential maps is very important for exploration and development of mineral resources. In countries like Zimbabwe for example, mineral resource development has played an important role for sustainable economic development. For many years now, the northern parts of Zimbabwe, especially the Magondi Belt, have been a target for gold and base metal exploration. Alaska and Mhangura are the major copper producing mines currently in operation. The Magondi Belt is situated in the Magondi district north-west of the capital city Harare. It covers an area of 8,500 km^2 between 16° 15'S and 17° 30'S latitude and between 29° 50'E and 30° 15'E longitude.

Copper production and exploration in the Magondi Belt started in the 15^{th} century, following the old workings exploited by the local people. Proper exploration activities however, started as the early 1940s with employment of advanced exploration techniques by the Zimbabwean Government and mining companies. During the period 1970 to 1978, the production of copper reached its peak and a maximum of 55,000 tones of copper have been exploited (Kambewa, 1998). Since then, most mines are either exhausted or closed. To substitute the old mines and sustain the country's economy, the Geological Survey of Zimbabwe (GSZ) has conducted a number of exploration surveys. In 1970, ground and airborne geophysical surveys were conducted in the area. Between the years 1983-1995 the GSZ, in collaboration with the Japan International Co-operation Agency, Metal Mining Agency (JICA), has carried out exploration work. The work concentrated on the collection of geochemical, geophysical and geological data in the northern part of the Magondi basin (Kambewa, 1998).

Today, the GSZ has acquired large amounts of geological datasets from various conventional exploration and mining companies. Most of the information is dispersed and kept in analogue format. However, no attempt has been done to convert these data and integrate information to establish a mineral potential map to attract investment in the region. Moreover, the existing geological map is published in 1961, and does not convey detailed information for undertaking mineral potential mapping. At present the area is covered by optical and microwave remote sensing digital datasets, but these datasets have not been processed and integrated with the available geological data.

Conventional geological mapping and mineral exploration are labour intensive and require high investment, and take long periods of investigation. On the contrary, modern exploration techniques are cost effective and quick and can be achieved in less time. In this research, the various datasets available for the Magondi Belt were processed, integrated and modelled using Geographic Information System (GIS) and Remote Sensing (RS). The objective of this research was to integrate the available geological datasets in order to update the geological map and to produce a mineral

potential map. In the research, optical and microwave remote sensing datasets and aeromagnetic remote sensing data were processed, interpreted and integrated for both geological and mineral potential mapping. Ground truth field observation datasets were used to further improve and validate the geological map. Comparisons were made between the old and updated geological map. Geochemical soil sample and aeromagnetic data were processed and analysed. The results of analysis and interpretations were used in spatial data integration and predictive modelling for mineral potential mapping.

The interpreted images were further integrated to produce an updated geological map. The new geological map was used to extract spatial evidences for predicting mineral potential map. Estimation and integration of spatial evidences were conducted using evidential belief functions (EBFs). The belief function maps were integrated and the resulting map was classified to produce a binary predictive mineral potential map. Validations conducted on the binary predictive map using Cu anomaly and deposits indicated a satisfactory result which implies the usefulness of the model for further exploration of undiscovered strata-bound copper deposit in the northern parts of the study area.

1.2. Problem statements

The Magondi Belt of Zimbabwe contains several copper mines, which were discovered as a result of follow up investigation of old workings exploited by local people. Currently, a number of mines are closed and the present ones are depleted due to long period of exploitation (Kambewa, 1998). These mines are considered to be favourable spatial indications for finding new potential areas. Exploration of new potential locations for mineral development commonly takes place in and around areas where mineral deposits have already been found (van Roij, 2006). For this reason, the study area attracts exploration companies to conduct investigation to discover new deposits. However, investors require organized datasets to decide and plan their exploration activity. This indicates that access to such datasets is very important. Mineral potential maps are an important part of such datasets, which help to focus the exploration activities over the most potential areas, thereby increasing the possibilities of finding new deposits by optimizing the exploration expenditure (Andrada de Palomera, 2004).

In the search for mineral potential areas, accurate and up-to-date geological maps are essential as it represents the most basic information for directing exploration activities. To this end, the published geological map of the study area which was published in 1961 needs updating. To the knowledge of the author, this map is too old, produced using conventional mapping techniques. However, GSZ has acquired several exploration datasets from different exploration and mining companies. The challenge is that there is no proper integration of the exploratory datasets such as aeromagnetic, optical and microwave data in order to prospect and delineate new exploration targets. Moreover, modern exploration techniques and new tools like RS and GIS have not been applied in order to integrate the

diverse geological datasets to predict mineral potential map for certain types of mineral deposits in the Magondi Belt.

1.3. Research objective

The main objective of this research is to apply GIS and RS based techniques for interpretation and integration of diverse geologic datasets such as, geological, geochemical, geophysical, and optical RS and microwave datasets, to update the existing geological map and to produce a mineral potential map of the Magondi Belt. The research aimed at testing the capability of the integration model to produce mineral potential map.

In order to achieve the major objectives the following sub objectives were set:

- Interpret the remote sensing images and aeromagnetic data to update the existing geologic map of the area.
- To delineate the host rocks of strata-bound Cu-Ag-Au mineralization.
- To identify geologic features with spatial associations to Cu-Ag-Au mineralizations and extract these features from the available geological, geochemical, remote sensing, and aeromagnetic datasets.

- To quantify the spatial associations of known Cu-Ag-Au mineral deposits with the geological features of the study area and develop models capable of integrating and predicting areas with potential for Cu-Ag-Au mineralizations.

1.4. Research Question

1. How can remote sensing, geomagnetics, geochemical and geological datasets be used for updating geological map and modelling the mineral potential of the study area?
2. Which tectonic structures have spatial association with Cu-Ag-Au mineralization in the study area?
3. Which simple approaches are useful for integrating the geological datasets in order to predict the mineral potential of the area?

1.5. Hypothesis

It is possible to interpret and integrate various geological datasets such as geological, geochemical, geophysical, remote sensing and known mineral deposit data in order to update the geological map and produce a mineral potential map of the research area using RS and GIS. There may be unidentified host rocks and tectonic structures which controlled mineralization in the study area. To predict where these mineral deposits of interest might occur, it is necessary to study spatial association between known deposit occurrences and certain geological features that control their occurrence. GIS-based predictive modeling such as evidential belief functions (EBFs), involves analysis of spatial associations between multi-layered geological features and known deposit occurrences to predict where deposits of interest are likely to occur.

1.6. Methodology

Updating the geological map and producing a mineral potential map is the general purpose of this research. In both methods, several steps were undertaken. In the first instance literature review was done for extracting information concerning the general geology of the study area. Data preparation and pre-processing of optical and microwave remotely sensed images, such as Landsat TM, ASTER, SRTM and aeromagnetic data were conducted using ILWIS and ERDAS software. Various image enhancement techniques were employed to clearly visualize the image. Radiometric and geometric corrections were applied in order to remove the influence of the atmosphere and to get surface reflectance. Images were georeferenced and subset into one projection system.

The existing 1:1,000,000 scale geological map of the research area was digitized from the existing geological map of Zimbabwe at a scale of. Additional geological features in northeastern parts of the study area were digitized from interpreted maps of Landsat TM and low resolution aeromagnetic data at a scale of 1:500,000 (Carballo Lopez, 1998).

Mean values digital numbers (DN) of lithological units in individual Landsat TM and ASTER bands were calculated and the values were plotted to see which band best discriminate the lithologies. Based on the selected individual bands an image classification was carried out using maximum likelihood classification.

Appropriate band combinations were chosen for lithological and structural interpretations. The band combinations were variously fused with the SRTM data in order to further enhance lithological boundaries. The shaded-relief image of the SRTM was used for interpretation of lineaments. Analysis and extraction of lithology, lineament and faults were supported by sample datasets and information obtained from the existing geological maps. Geological features extracted from the fused images were integrated with the sample datasets into one digital format in GIS. The extracted geological features were digitized in order to produce an updated geological map.

Four major steps were followed for creating a mineral potential map: 1) spatial data input, 2) conceptual data development, 3) spatial data processes, and 4) integration and validation. The first step consists of input of spatial data like, geological, geophysical, geochemical data and occurrences of known mineral deposits in the study area. Development of conceptual exploration model was based on literature review of strata-bound Cu-Ag-Au deposit of study area. Here, information regarding the deposit model in sedimentary basin environment was referred from literature. Study of general characteristics of sedimentary Cu deposits in the area and establishment of criteria for the recognition of potential zones for the occurrence of these deposits was carried out. Based on the conceptual exploration model, spatial data analyses were carried out. Extraction of geological features that have spatial association with Cu-Ag-Au mineralization in the study area was the third step, which results in evidential maps to be used in the predictive mapping of Cu-Ag-Au mineralization potential

of the study area. Integrating the evidential maps for Cu-Ag-Au mineralization and validation of the predictive maps were the last step undertaken.

1.7. Justification

The Magondi Belt of Zimbabwe, which has a favourable geological setting for gold and base-metal mineralization, there are adequate geological datasets obtained from past geological mapping and exploration surveys. The datasets includes geological map, aeromagnetic and geochemical data; remote sensing images and several mine data. These datasets and the favourable geological setting attract mining companies to explore potential areas for development. In order to increase the chance of mineral discoveries and optimize the exploration expenditure, mining companies require geoscientific knowledge which indicates the type of mineralization and locations of potential areas (Andrada de Palomera, 2004; Thurmond *et al.*, 2006). However, the lack of up-to-date geological maps and absence of mineral potential maps holds back the investment and development activities in the region.

There may be unidentified host rocks and tectonic structures which controlled mineralization in the study area. The challenge is how to map these features in order to know potential areas for mineralization. At present, it is difficult for the GSZ to use the conventional methods of geological mapping and mineral exploration to find target areas for mineral deposit along extensive area, since these techniques are labour and capital intensive, and require long period of investigation.

Today, powerful tools of RS and GIS have contributed a lot in modern geological mapping and mineral exploration by enhancing, interpreting and integrating of various geologic datasets. Integration of remotely sensed data and airborne magnetic data with other geological datasets is a promising and cost effective method to add new structural and lithological features to the geological map in a diverse geological province like the present research area, Magondi Belt (Isabirye Mugaddu, 2005), (Le Thi Chau, 2001). Mineral potential mapping involves delineation of potentially mineralized zones based on geological features that are characterized by a significant spatial association with target mineral deposit (Porwal *et al.*, 2006). A systematic exploration program for geological and mineral potential mapping therefore involves the integration of geological, geochemical and geophysical techniques (Carranza *et al.*, 1999). All the geoscience information together with pre-processed remotely sensed data can be used as evidence to delineate potential areas for further investigation (Chang-Jo and Fabbri, 1993).

GIS together with traditional geoscience datasets are used to obtain effective predictors of mineral potential (Harris *et al.*, 2006). Different researches revealed that enhancing, integrating and analysis of geoscience data together with interpretations of remotely sensed datasets could help in predicting mineral potential. To this end, Evidential Belief Functions theory (EBFs), which has been widely used in mineral potential mapping (Carranza and Hale, 2003), was used to predict the potential for Cu mineralization in the Magondi Belt. It was chosen because the method uses both knowledge and data driven approaches and requires a number of representative mineral deposits to compute the spatial association between the deposits and the geological features. The Magondi area therefore fulfils all

these criteria. This is the first time that EBFs were applied for mineral potential mapping t therefore this study would help support the previous prediction techniques, which were totally based on simple overlay methods (Carballo Lopez, 1998; Kambewa, 1998).

1.8. Organization of the thesis

This thesis deals with integration of geological datasets for updating the geological map and mapping of mineral potential of Magondi Belt. The first chapter introduces the research background, the problem definition, the scope and objective, and the questions and hypothesis of the research. Information about the study area, such as location, access, general geology and previous works are given in chapter two. Part of chapter two introduces tectonic setting, metamorphic history and mineralization of the rocks in the study area.

The detailed methodologies employed for the geological mapping and mineral potential mapping of the belt are described with the help of flow charts in chapter three. Data inputs, organization and processes, spatial analysis, validation of results are the main steps followed in this chapter. The available input data and software used for processing and analysis are mentioned in the same chapter. Data processing and interpretation of analogue, aeromagnetic, optical and microwave remote sensing data are clearly mentioned in the chapter. The data processing techniques mainly focused on multispectral images, high resolution aeromagnetic data and geochemical stream sediment analysis. Pre-processing of Landsat TM, ASTER and SRTM images are part of this chapter. Chapter four deals with data integration and analysis for lithological and lineament mapping. The geochemical and geophysical anomaly maps are integrated together with multispectral processed images to produce an updated geological map. In chapter five, the method of EBFs for mineral potential mapping is described. Conceptual model of mineral deposit, the deposit recognition criteria and spatial evidence extractions done based on the geo-exploration data are discussed in detail. In this chapter, the spatial association analyses were done between the evidence maps and copper mineralization followed by spatial data integration for predictive mineral potential modelling. Here, generation and combining of the predictor patterns and validation of the predictive model were undertaken to produce a predictive Cu-Ag-Au potential map. Finally, the results are discussed and conclusions are made on chapter six. Recommendations are also made on the same chapter.

2. Study area

The northern part of Zimbabwe, especially the Magondi Belt, has been a target for gold and base metal exploration for many years (Figure 2.1). Alaska and Mhangura, in the central part, and Shamrock in northern parts of the country, are some of the explored base metal mines currently under operation (Kambewa, 1998; Woldai *et al.*, 2006). The Mhangura mine consists of two strata-bound, sediment-hosted copper-silver deposits of Mangula and Norah. The main copper production of Zimbabwe comes from these mines with by-products of gold and silver.

2.1. Location and access

The research area is situated in Zimbabwe about 187 km north-west of the capital city Harare. It is bounded by 16^0 15'S and 17^0 30'S latitudes and by 29^0 50'E and $30^0$15'E longitudes with center at about interception of 17^0 00'S latitude and 30^0 00' E longitude (Figure.2.1). The area extends 170 km north-south and 50 km east-west, covering a total area of 8,500 km^2.

Access to the area is possible through the town Chinhoyi, about 130 km west of the capital city Harare. The two operating base metal mines, Mahngura and Shamrock are accessible from Chinhoyi. Mhangura mine is 70 km north of Chinhoyi (Figure 2.1).

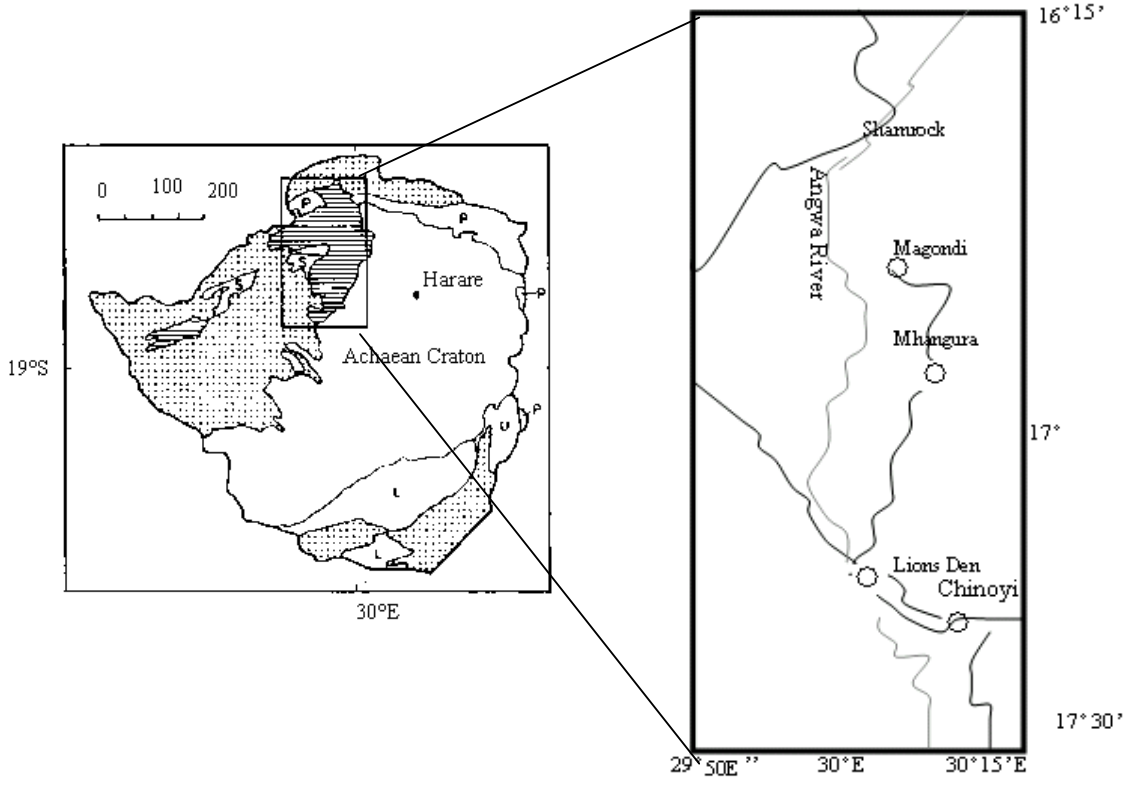

Figure 2-1 Location map of the research area

2.2. Previous work

Magondi basin is a known Cu-Ag-Au mining province since 15th century. Copper metal was mined for production of ornamental and cutting objects by local smelters (Kambewa, 1998). Following the old workings by local people, a continuous exploration survey was conducted since late 1940's to mid 1970's. Stagman (1952) was among the first researchers to map the geology of the area around the Mangula Mine, Lomagundi and Guruve district (Stagman, 1978; Kambewa, 1998). Later on he tried to classify the geology of the area into basement and Magondi supergroup in 1978. The Magondi Belt had been studied by Master (Master *et al.*, 1989; Master, 1991) from 1987-1991. In 1989, he studied the mineralization of copper and silver in red beds of early Proterozoic alluvial fans of the Mangula Mine, while in 1991, his research concentrated on the origin and controls on the distribution of copper and precious metal mineralization at Mhangura and Norah Mines.

During the year 1993 to 1995, the Geological Surveys of Zimbabwe and the Japan International Co-operation Agency, Metal Mining Agency, have conducted exploration work in northern part of Magondi Basin. Geological, geochemical and geophysical surveys were conducted during the joint exploration program (Kambewa, 1998).

Master *et al*. (1996) have integrated geological, geophysical, geochemical and Landsat TM data to identify the Highbury impact structure in the Magondi copper belt (Master *et al.*, 1996). Kambewa (1998) and Carballo Lopez (1998) have conducted a research on the use of GIS and integration of remote sensing and geochemical data for mineral exploration in Magondi Basin. Both researchers were focused on integration of geological datasets with emphasis on geochemical data analysis in order to produce mineral potential map based on simple overlay techniques. Master (2003) has also explained the mineralization, host rock and tectonic structures of Norah Mine (Master, 2003). Validation and sensitivity analysis for mineral potential mapping were also done on the Magondi datasets (Woldai *et al.*, 2006)

2.3. Geological setting

2.3.1. Magondi Supergroup

The Magondi Mobile Belt, which flanks the Zimbabwe Archaean craton to the NW, consists of volcanics and sediments of the Magondi Supergroup deposited during the early Proterozoic ~1850 Ma (Treloar, 1988). The Archean rocks, capping the basement beneath the Magondi Supergroup, consist of the Midlands and Chinoyi Greenstone Belts, the Biri and Mangula granites and the Hurungwe gneiss in the study area (Carballo Lopez, 1998). The rocks of Magondi Supergroup, which were deposited in the Magondi Basin, extends under younger cover towards Botswana (Woldai *et al.*, 2006) The belt at the northwest rim of the Craton extends over a length of 250 km from the Munyati River area in the south to the Shamrock Mine area in the north. The Magondi Supergroups subdivided into the Deweras, Lomagondi and Piriwiri Groups (Hahn, 2002).

The Deweras Group, in the southern part of the belt, shows a good stratigraphic correlation with those of the Silverside Mine area located between the middle and the northern part of the belt (Hahn, 2002). The Deweras Group is predominantly composed of continental sediments and basalts deposited in a rift-related basin margin environment marked by crustal instability. The bottom of the Deweras Group rests unconformably on Archean and earliest Proterozoic granite-greenstone belt rocks and gneisses (Figure 2.2-3). Field relations suggest that the amphibolite sills of the Doma west area are same as that of the Deweras metabasalts occurring in the Silverside, in the southern part of the belt

The Formations of the Lomagondi Group, Mcheka and Nyagari are characterized by lithologies formed in stable depositional environments reflecting shelf margin conditions. The Magondi belt rocks are normally not affected by subsequent Pan-African deformation and metamorphism. The evolution of the belt seems to fit the emerging pattern of cratonisation of the African plate, within which pattern the Magondian Mobile belt may be correlated with other 'Eburnian' cycle belts in South Africa but not with any of the tectonothermal provinces to the north of the Pan-African Zambezi-Damara belt (Treloar, 1988). Metamorphism in the northern part of the belt is explained by thermal relaxation after the overthrusting of hot early Proterozoic rocks from the west effectively sandwiching the Magondi rocks between Archaean basement below and early Proterozoic basement above. The metamorphic facies in the belt varies from low-grade greenschist-facies in the south to middle and upper amphibolite-facies in the north (Munyanyiwa and Maaskant, 1998). In the extreme north and north western part, granulite-facies rocks are developed.

.

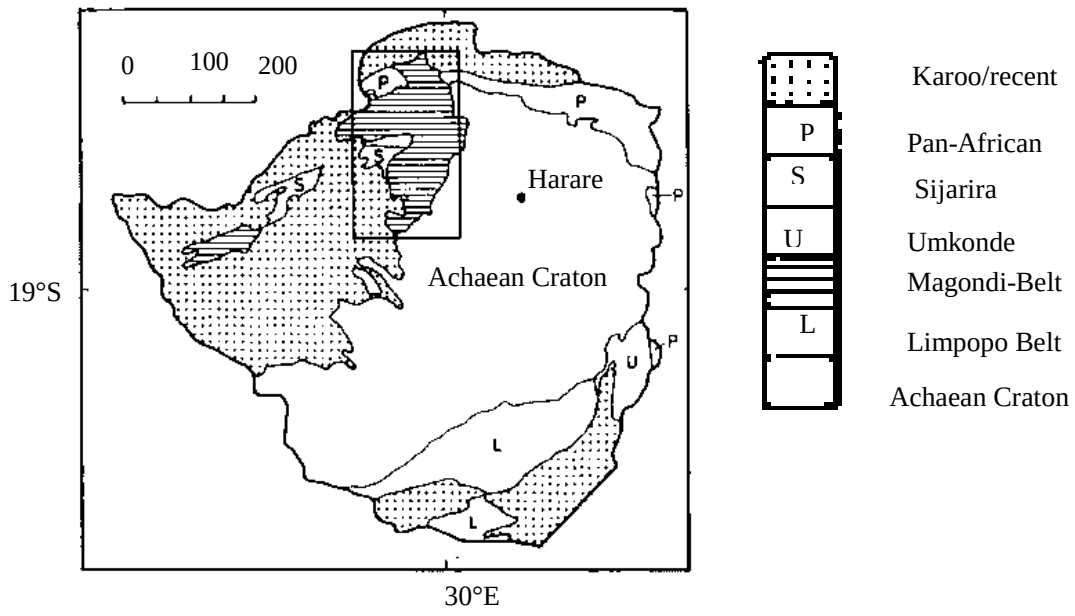

Figure 2-2 Simplified geological map of Zimbabwe showing the mobile belts and cover surrounding the Archaean craton (after Stagman, 1978). Box shows the Magondi mobile belt, study area, enlarged on Figure. 2.2.

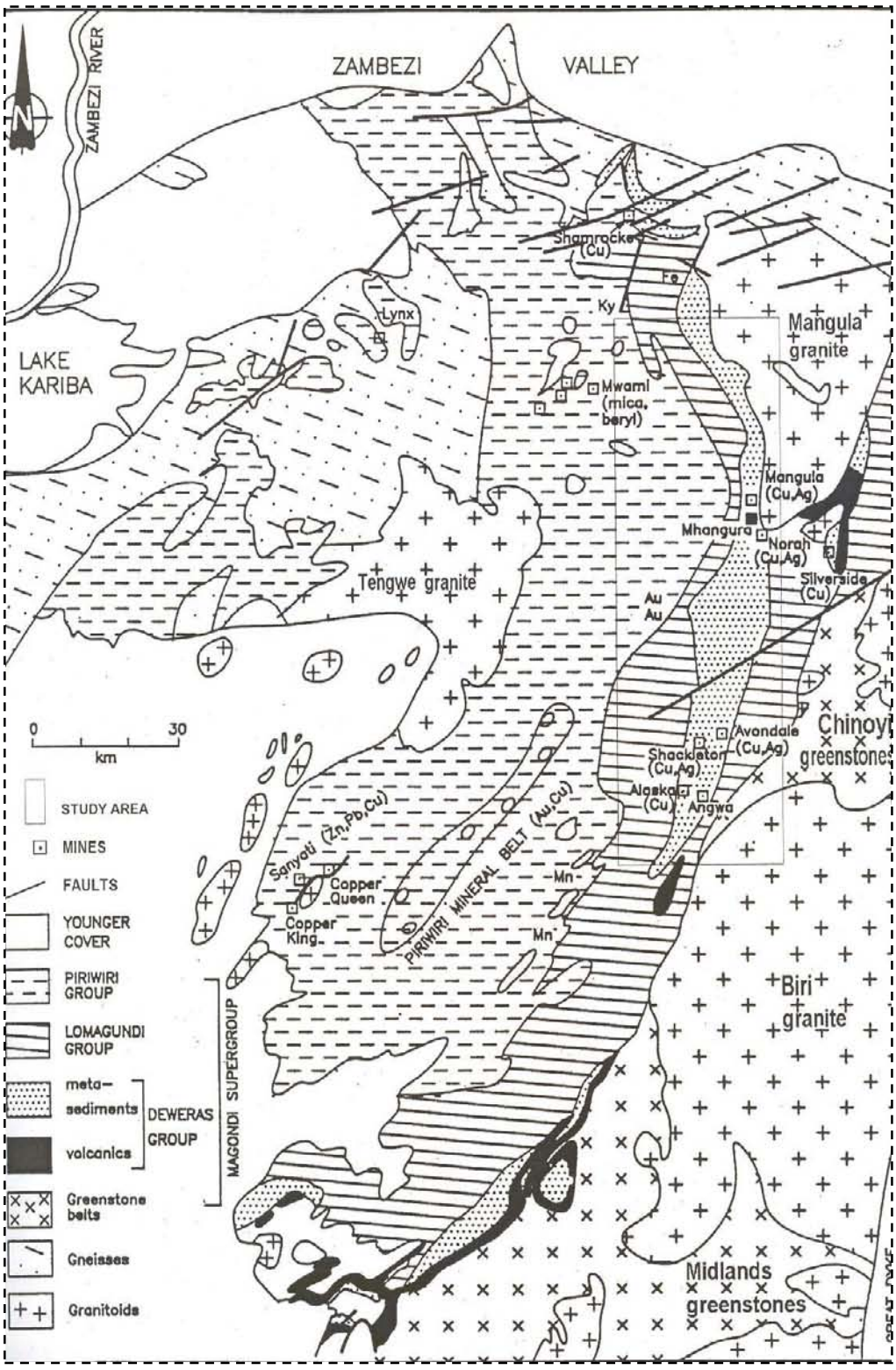

Figure 2-3 Geological map of north-west Zimbabwe; showing the Magondi Supergroup, the basement gneisses, granitoids of the Archaean craton and the surrounding cover (after Stagman, 1978).

2.3.2. Basement Complex

The Archean and earliest Proterozoic granite-greenstone belt rocks and gneisses of the Zimbabwe Craton form the basement complex underlying the Magondi Supergroup. These rock units are exposed in the south-eastern, north and north-eastern parts of the study area (Figure 2.3). The larger portion of the basement consists of granite with relatively small greenstone rocks (Stagman, 1978). The greenstone rocks comprise lavas of basaltic and andesitic composition. The gneissic rocks are rare and mainly quartzo-feldspathic gneisses, which are predominantly medium to coarse-grained biotite gneisses, locally migmatised during partial melting. The gnessic rocks are mainly composed of alkali and plagioclase feldspars, biotite with less abundant hornblende, garnet, clino- and orthopyroxene. Preliminary Rb-Sr and U-Pb radiometric data suggest that the gneisses are Paleoproterozoic to NeoArchaean in age (Munyanyiwa and Maaskant, 1998). Single zircons analyzed for U-Pb isotope from granite indicated that the intrusions took place during Paleoproterozoic Orogenesis (Majaule *et al*., 2001).

2.3.3. Deweras Group

The rocks of the Deweras Group crop out in two main parts of the belt (Figure 2.4).They are exposed around the Munyati and Mupfure rivers. In the north, this extends from Alaska mine to Shamrock mine. The group consists of metamorphosed conglomerates, arkoses, feldspathic sandstones, greywackes, mafic tholeiitic lavas and subordinate quantities of evaporates (Munyanyiwa and Maaskant, 1998). The Deweras Group in the northern part of the Magondi basin, which is the area of interest of the present study, is divided into Mangula, Norah, Suiwerspruit and Chimsenga Formations (Figure 2.4). These formations consist of host rocks of the copper mineralization in the Magondi Belt.

The Norah Formation comprises mainly thinly bedded anhydrite-bearing dolomite and argillite with interbedded pink ripple marked arkoses. The Norah copper deposit is found within dolomitic argillites and grits overlain by grey chlorite quartz wackes with thin interbedded evaporate beds consisting of anhydrite, barite, celstite, chlorite, tourmaline and copper sulphides (Kambewa, 1998). The Suiwerspruit Formation has mafic lava flows separated by interflow sediments, which overlie a mafic pyroclastic sequence of tuffs, volcanoclastics and agglomerates. The Chimsenga Formation consists of arkoses and argillites that overly volcanics of the Suiwerspruit Formation and forms the upper part of the Deweras Group in Mhangura area. Basic intrusions consist of metadolorites such as dykes and sills are common in Deweras Group. The Mangula Formation comprises the lower-most portion of the Deweras Group at Mhangura and unconformably overlies the Mangula granite. It consists of cross bedded and plane-bedded meta-arkosic red beds, together with conglomerates, greywackes, argillites and basalt. The arkoses of the upper arenaceous formations of the Deweras Group are host rocks of the copper mineralization in the area. Except in the vicinity of some mines, where silicification prevents weathering, there are only small out-crops, often several kilometres apart and separated by fine, pale sandy soil (Stagman, 1978). It is one of these areas which the research is interested in to identifying the covered host rock by using the integrated remote sensing and aeromagnetic datasets.

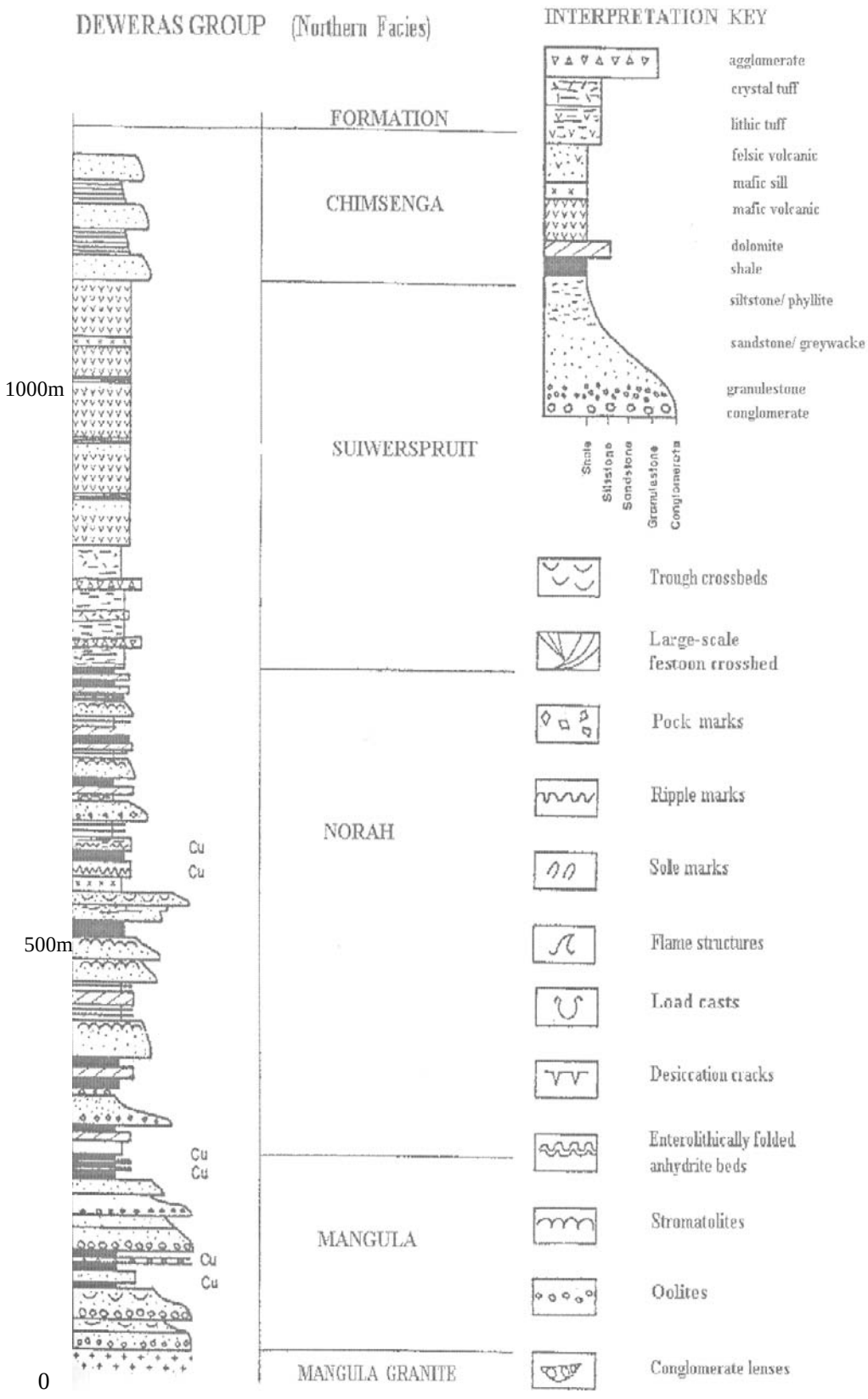

Figure 2-4 Generalized lithostratigraphy of northern part of Deweras Group (after Master, 1991).

2.3.4. Lomagundi Group

The out-crops of this group extend from the Ummiati River in the south to the Zambezi escarpment for about 250 km (Stagman, 1978). This group comprises mainly quartzites, dolomites and phyllites. The Lomagundi Group unconformably overlies the Deweras Group, and transgresses onto the Archean basement in some places. This group consists of three formations namely: Mcheka, Nyagari and Sakurgwe (Figure 2.5).

The Mcheka Formation consists of basal pebbly grits overlain by a lower dolomite, phyllite, quartizite, upper dolomite and sandy argillites. The basal unit is represented by conglomerate up to 30 m thick consisting of clasts of vein quartz, arkoses and lavas of the Deweras Group; quartzite and phyllite. The nature and composition of the clasts indicates that the conglomerate was derived from the underlying Deweras Group and greenstone rocks. The Nyagari Formation consists of argillaceous sediments, slate and graphitic shales interbedded with sandstone and arkosic grits, overlain by a volcanic sequence consisting of andesitic lava and pyroclastic rocks with associated cherts. The uppermost Sakurgwe Formation consists of a succession of poorly bedded greywackes, with the occasional narrow intercalated shale or feldspatic quartzite horizon. The greywacke are poorly sorted and contain angular quartz, plagioclase and lithic fragments as well as chlorite and sericite.

The rocks along the eastern belt of Lomagundi dip generally 30^0 and 40^0 to the west. All the rocks particularly the argillaceous sediments trend parallel to bedding strike having sub vertical foliation of schistosity (Stagman, 1978). The calc-arenite and stromatolite structures of the dolomite indicate a shallow water evaporitic environment.

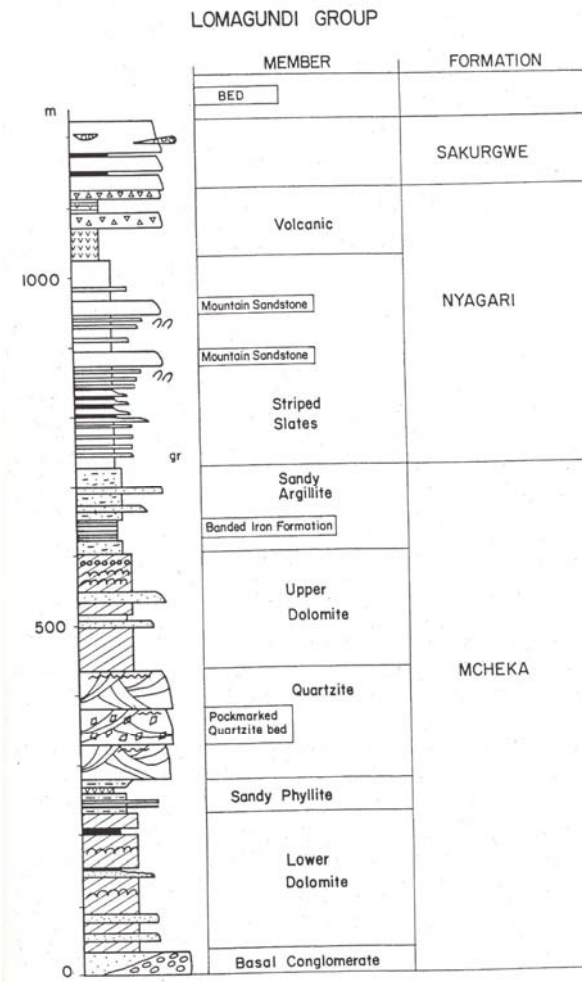

Figure 2-5 Lithostratigraphic units of Lomagundi Group (after Master, 1991). See Figure 2.3 for legend.

2.3.5. Piriwiri Group

This group conformably overlies the Lomagundi Group. The monotonous succession of this group form a belt of 50 km wide in Zimbabwe west of Sinoia (Stagman, 1978). It consists of phyllites, greywacke, black graphitic and ferruginous slates, cherty quartzite and subordinate argillaceous and arenaceous with rare volcanic and pyroclastic rocks. It comprises three formations namely: Umfuli, Chenjiri and Copper Queen (Figure 2.6). The basal part Umfuli Formation consists of black graphitic slates and breccias and pyritiferous slates with narrow bands of cherty quartzite. It consists of agrillites and phyllites with minor interbedded greywacke. The Chenjir Formation consists of phyllite and greywacke, with thin beds of tuffs, chert and pyritiferous slate, and thicker beds of micaceous quartzite. The upper most Copper Queen Formation consists of sequences of phyllites and micaceous

feldspathic quartzite, with a thin beds and lenses of agglomerate, tuff and associated narrow, cherty albitite dykes.

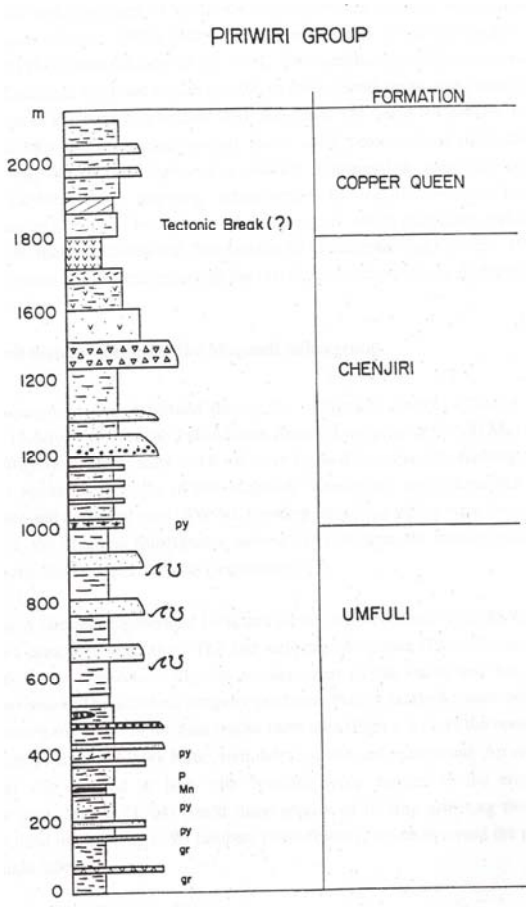

Figure 2-6 Generalized lithostratigraphy of the Piriwiri Group (after Master 1991). See Figure 2.3 for legend.

2.4. Metamorphism

The Magondi Supergroup was deformed and metamorphosed during the Ubendian orogenic cycle, about 2.0-1.8 Ga ago, and is now part of a large east vergent fold and thrust belt along the western margin of the Zimbabwe Craton. The metamorphism grade increases along strike to the north and northwest, from greenschist-facies near and south of the Shackleton and Avondale copper mines near the craton margin, through mid-amphibolite facies around Karoi, to upper amphibolite and granulite facies north and northwest of Karoi (Munyanyiwa and Maaskant, 1998).

2.5. Tectonic settings of Magondi Supergroup

The Magondi rocks were deposited in a back-arc continental basin developed in response to an easterly directed subduction zone (Munyanyiwa and Maaskant, 1998). The subduction zone was tectonically set in a rift related basin which formed on the continental side of an Andean-type magmatic arc under the Zimbabwe Archean Craton (Figure 2.7). The distribution of the supracrustal rocks of Magondi Belt was interpreted to record the transition of a passive-margin setting into geosynclinal flysch-type deposits. The magmatic arc was part of a continental scale magmatic arc produced during the "Ubendian" cycle (2.2-1.8 Ga), involving the collision of two Archaean age continents, immediately after the consumption by subduction of the intervening oceanic crust (Master, 1991; Carballo Lopez, 1998). The sedimentary rock in the Magondi supergroup were formed within the rift valley by sedimentation, which was later extended by left lateral fault parallel to Great Dyke. A strike slip fault forms parallel faults and an anticline fold axis which cross obliquely to the rift valley. These structures were formed before compaction of sediments and were pathways to metal solution to the present strata-bound disseminated copper deposit (Kambewa, 1998). As a result of compression and shortening during the second phases of deformation, N-S and NNE-SW trending folds were developed. Folding of the Priwiri Group mainly on NN easterly axes curving N and eventually NNW are common example (Stagman, 1978). Here, three phases of folding were encountered. Tight folds with axial plane trending NE-SW, asymmetric folds trending NE and NNE and open folds with NW trending axial plane are the first, second and third phases of folding respectively (Kambewa, 1998). The first phase of folding, which has NE folds trending N65°E to N55° in Deweras Group, was affected by cross folds trending S140° E. An axial plane and fracture cleavages are manifested on early folds on argillaceous psammitic rocks. The rocks of the Lomagundi Group were deformed by three phases of folding; the first phase has NE, eastward-verging folds, refolded to N-W trending folds with NE trending cleavages indicating the third phases of deformation.

The Deweras group stratigraphy indicates that it was deposited in a continental rift basin, which was faulted with the Archean basement to the east. It is an elongated fault bounded trough parallel to the sinistral strike slip faults traversing the Archean craton of Zimbabwe in SSW-NNE direction. The basin fill pattern was one of the transverse alluvial fans and transverse braded plains, within distal playa lakes. In the Deweras Group, the amphibolite sills were folded together with the enclosing sediments during the Magondi Orogeny (2000 and 1800 Ma). The refolding of these group rocks occur around 530 Ma, in the Pan-African Orogeny. Deformed amphibolites are also observed in the Lomagundi Group, in the northern most part of the belt (Shamrock and Makuti-East areas) (Hahn, 2002).

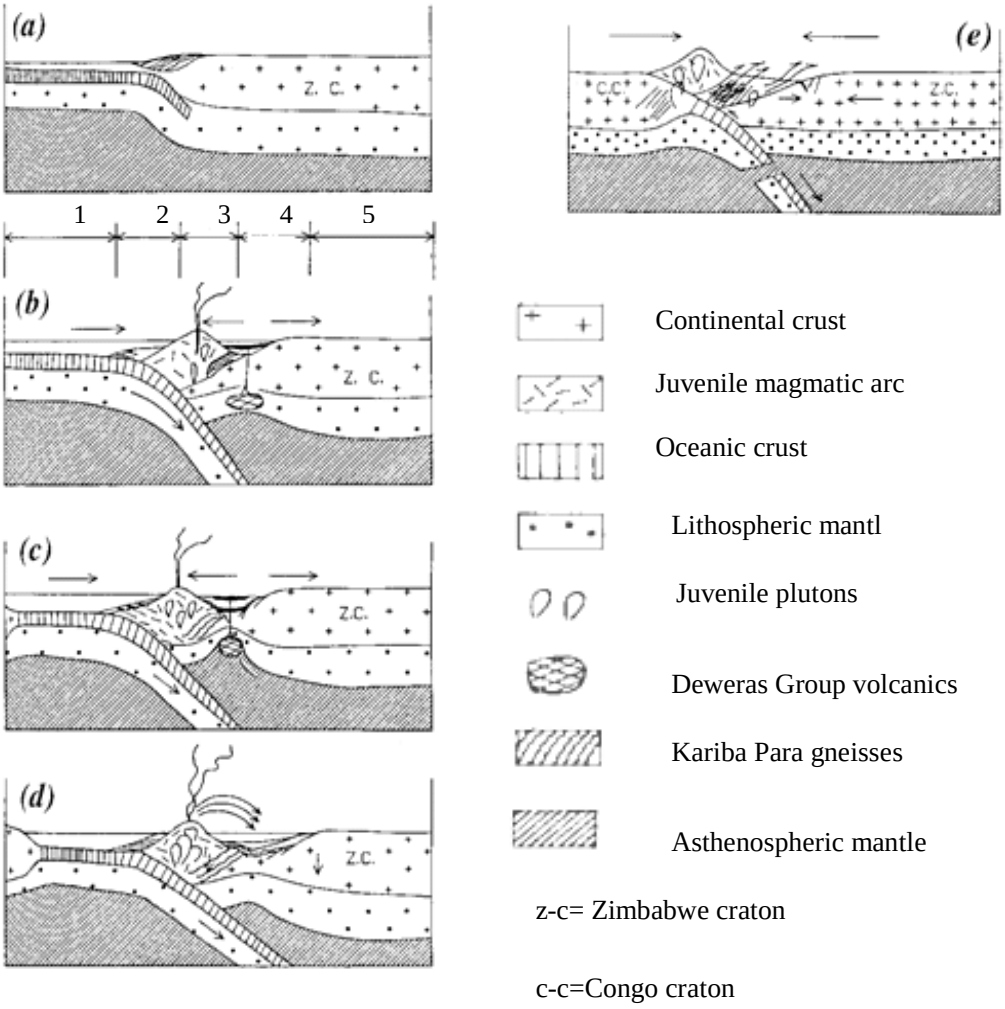

1=ocean basin; 2=fore-arc; 3=magmatic-arc;
4= Magondi back-arc basin; 5=Zimbabwe
Achaean basin

a) 2.2 Ga. Initiation of subduction
b) 2.1 Ga. Early back-arc rifting. Deweras Group deposition
c) Later rifting. Deweras Group deposition
d) Thermal subsidence stage. Lomagundi and Piriwiri group deposition
e) Collisional stage, Magondi orogeneny

Figure 2-7 Schematic summary of the evolution of the Magondi Basin between 2.2 to 1.8 Ga, from the initiation of back-arc rifting, and the deposition of the Deweras, Lomagundi and Priwiri groups, to the Magondi Orogeny (after Master, 1991).

2.6. Mineralization

2.6.1. Deweras Group

The Magondi Belt is known by its base metal mineral potential sources. The two currently operating mines, Alaska and Mhangura, produce copper with silver and gold as a by product. The Mangula mine, the largest known deposit, with original deposit reserve of 60 million tons at an average grade of 1.2% copper and 20 g/t silver with by products of gold, platinum and palladium. It is a strata-bound copper silver deposit hosted in rocks of the Deweras Group (Kambewa, 1998; Master, 2003; Woldai *et al.*, 2006). Rocks such as arkoses, conglomerates and semipelitic schist, which have a total stratigraphic thickness of about 200 m, are host rocks of the copper mineralization in Mangula Mine.

2.6.2. Lomagundi Group

Alaska and Shamrock mines are the major economic copper deposits found in highly sheared dolomite and sandstone and siltstones intercalations in the Lomagundi Group. The mineralization mainly consists of oxidized malachite ore, chalcocite and minor chalcopyrite. Malachite occurs as coatings along the cleavages and fracture planes. The Lovel Gold Mine is the only gold mine found in the Lomagundi Group. It is quartz vein type found in the lower dolomite of the Mcheka Formation and contains abundant hematite, calcite, and red ochre and minor copper sulphide.

2.6.3. Piriwiri Group

The Sanyati massive sulphide deposit (Zn-Pb-Cu-Ag) in the Piriwiri Group is found 100 km south west of Chinoyi. This deposit is characterized by malachite stains and ferruginous gossans extending from the Copper King Dome to Copper Queen Dome, over a strike length of about 25 km. (Master, 1991). Besides the base metal sulphide mineralization, the rocks of Piriwiri group are known to contain industrial minerals such as graphite, kyanite muscovite and beryl and gemstones like tourmaline, aquamarine and topaz.

The massive sulphide deposits in the Piriwiri Group were probably “sedimentary exhalative” deposits, which formed diagenetically during basin evolution (Woldai *et al.*, 2006). Minor Cu-Au occurrences of the “Piriwiri mineral belt” are related to the intermediate volcanics and pyroclastic rocks in the Piriwiri Group. The ore-forming minerals are chalcocite, bornite, chalcopyrite and pyrite with minor molybdnite and native silver. Traces of native gold, argentite, uraninite and wittichenite are also common. The ore is characterized by a chalcocite core surrounded by bornite rich and disseminated pyrite zones.

3. Datasets and Methodology

3.1. Datasets used

In this research various types of datasets were processed. ASTER, Landsat TM, SRTM and aeromagnetic geophysical data were used for identifying geological features like, lithology, lineaments, faults and folds. Deep seated structures and intrusions were easily identified using aeromagnetic geophysical data. The geochemical data were used to produce geochemical anomaly maps. The datasets of known mineral deposit was used for training in the prediction of mineral potential. Mineral occurrences and deposits of copper, which were not involved in the spatial analysis, were used to validate the predicted mineral potential map.

The geological feature in the research area were digitized from the Geological Maps of Zimbabwe (after Surveyor-General, 1985) at a scale of 1:1,000,000 and a Geological Map of Magondi north (after, Carballo Lopez, 1998) at scale of 1:500,000. These maps were used as input datasets in remote sensing image interpretations and integration in order to identify major lithologic units in the study area. Field observation data were used as cross-references during image interpretations and integration of geological data. The dataset were also used in validating the updated geological map of the study area.

The high resolution aeromagnetic data, total field magnetics, were used in interpreting subsurface geology in the soil covered south central parts of the study area. Multispectral remote sensing images, ASTER and Landsat TM, were used as input datasets in the interpretation of the lithology and tectonic structure in the study area. During the interpretation of tectonic structures such as lineaments, folds and faults, SRTM and ASTER digital elevation models (DEM) were used. In the image data integration, both DEM images were alternately fused with Landsat and ASTER images to in order to produce a lithological map. The updated maps and interpreted geochemical copper anomaly and analytical signal total field magnetic maps were finally used as spatial evidence map for predicting mineral potential.

3.2. General Methodology

Two methodologies were employed in updating the existing geological map and in producing map of mineral potential of the study area. The updated geological map was used as one set of input data in the methodology of mineral potential mapping. Flow charts indicating the general methodologies of both groups are shown in figures 3.1 and 3.2.

3.2.1. Updating geological map

The methodologies applied in updating the geological map of the research area involved several steps. Literature review was the first step in deriving information about the general geology of the study area. This was followed by data preparation and pre-processing of remotely sensed images, such as Landsat TM, ASTER, SRTM and aeromagnetic total field magnetic data. Pre-image processing such as radiometric and geometric corrections and image enhancement were employed in order to clearly visualize the image. During the image processing, all images were georeferenced into one projection system. Images were subset to the bounding coordinates of the research area. Appropriate band combinations were chosen for lithological and structural interpretations. The band combinations were variously fused with the SRTM data in order to further enhance lithological boundaries. The shaded-relief image of the SRTM and ASTER DEM were used for interpretation of lineaments. Analysis and extraction of lithology, lineament and faults were supported by aeromagnetic data. Geological features extracted from geophysical interpretations and fused images were integrated into one digital format in GIS (Figure 3.1). The extracted geological features were digitized to produce the updated geological map.

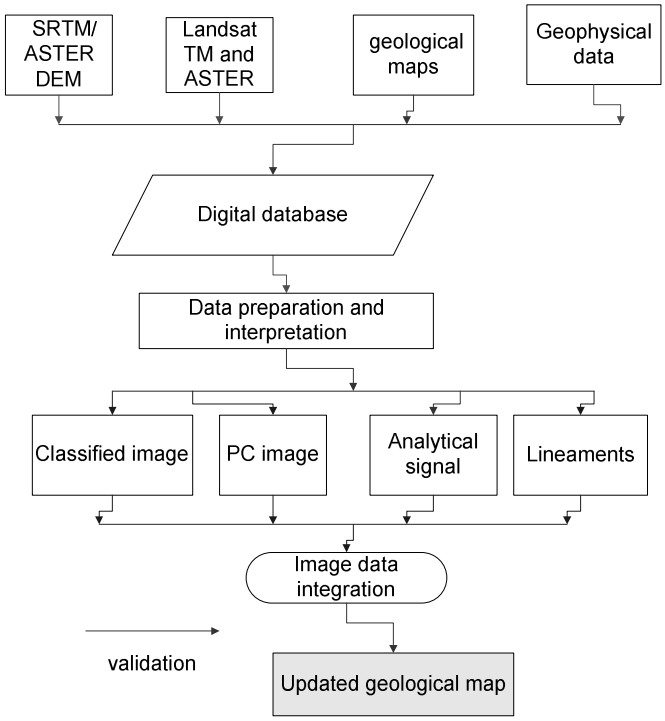

Figure 3-1 Flow chart for updating geological map of the research area.

3.2.2. Mineral potential map

The general steps of the research methodology for predicting mineral potential includes four major steps: spatial data input, conceptual data development, spatial data analysis, integration and validation (Figure 3.2). The first step consists of input of spatial data like, geological, geophysical, geochemical data and occurrences of known copper (Cu) deposits. Development of conceptual exploration model was based on literature review of strata-bound copper silver and gold (Cu-Ag-Au) deposit of study area and elsewhere in similar region. Here, information regarding the deposit model in sedimentary basin environment was referred from literature. Literature study of general characteristics of Cu-Ag-Au deposits in the area and establishment of criteria for the recognition of favourability zones for the occurrences of these deposits were carried out. Based on the conceptual exploration model, spatial data analysis takes place. Extraction of geological features that have spatial associations with Cu-Ag-Au mineralization in the study area was the third step. This results in evidential maps that were used in the predictive mapping of potential for Cu-Ag-Au mineralization. Integrating the evidential maps for Cu-Ag-Au mineralization and validation of the predictive map were the last step undertaken.

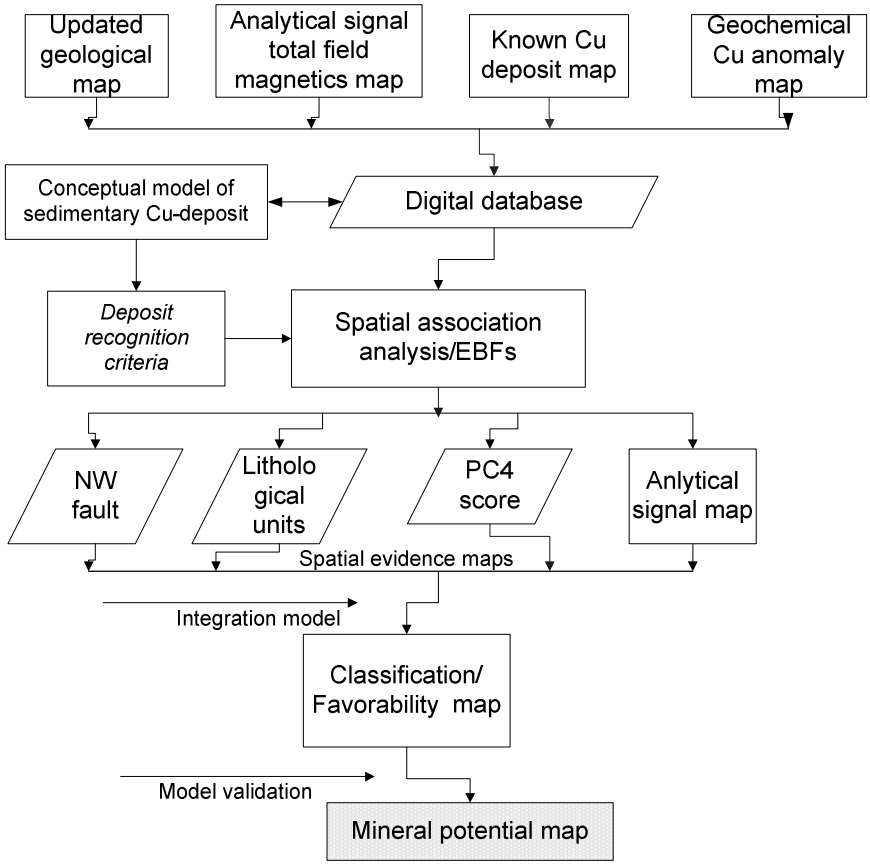

Figure 3-2 Flow chart for methodology of Mineral potential map

3.3. Processing and Interpretations of mapped and remotly sensed datasets

3.3.1. Analogue geological maps

The analogue geological map of Zimbabwe was published in 1961 by the Geological Survey Office of Zimbabwe at a scale of 1:1,000,000 (Surveyor-General, 1985). This geological map was used as an input dataset updating the geological map of the Magondi belt. The map was scanned and the raster image was georeferenced to UTM zone 36S projection using WGS84 datum. Ground control points were assigned based on the printed coordinates obtained on the raster map. Vector data were created using on screen digitizing of selected features within the bounding coordinates of the study area. (Figure 3.3). A raster scanned geological map, which covers the eastern and south-eastern parts of the study area, was also digitized using the same georeference and coordinate system. The geological map was a result of interpretation of Landsat TM and low resolution qualitative magnetic map produced by Lopez, 1998 (Figure 3.4).

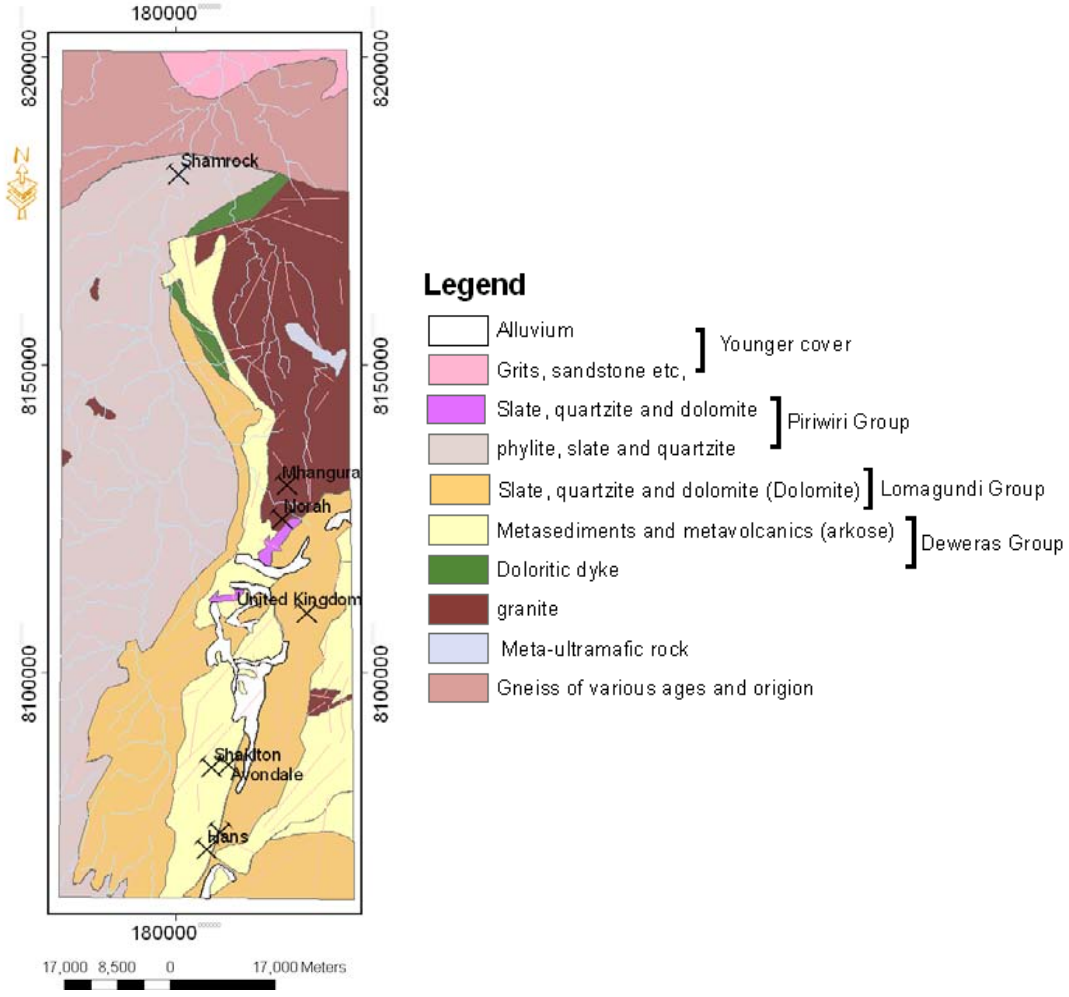

Figure 3-3Geological map of Magondi Belt digitized from Geological map of Southern Rhodesia, Surveyor-General (1985), UTM Zone 36S projection, WGS 84 Datum.

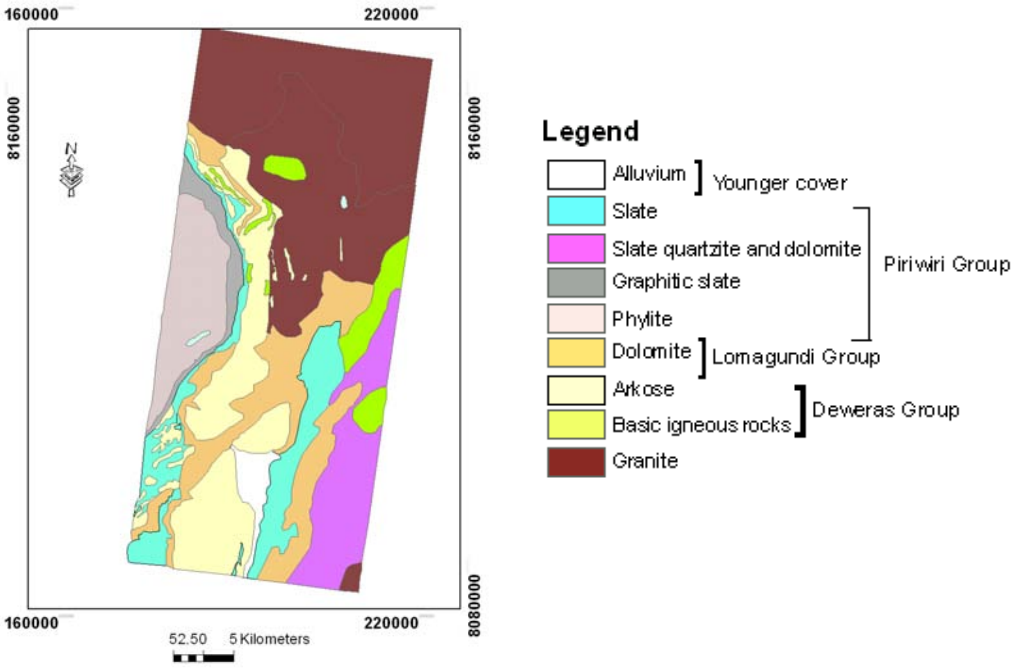

Figure 3-4 Geological map covering south eastern parts of the study are, digitized from Carballo Lopez (1998), UTM Zone 36S projection, WGS 84 Datum.

3.3.2. Multispectral image processing and interpretations

ASTER IMAGE

The accessibility of inexpensive, satellite-borne, multispectral ASTER data has created new opportunities for the regional mapping of geological structure and rock types including alteration products (Hewson *et al.*, 2005). Different spectral bands of ASTER imagery are acquired at different spatial resolutions; the visible and near infrared bands (VINR bands 1, 2 and 3), which are very close spectrally to the comparable spectral bands of Landsat, 15 meter resolution (Figure 3.5). There are six bands in the shortwave infrared (SWIR) with 30m resolution, and five bands in thermal infrared (TIR) with 90 m resolution. ASTER near infrared bands 3N and 3B can generate along-track stereo image pairs which can be used to generate high quality digital elevation model (DEM) (Lips *et al.*, 2002). The VNIR, SWIR and TIR wavelength regions provide complementary data for lithological mapping. The three VNIR bands are important sources of information about absorption in transition metals, especially iron and some rare-earth elements (REE) (Hewson *et al.*, 2005). In the six SWIR bands, carbonate and hydroxyl mineral spectra display absorption features related to overtones and combination tones. Rock-forming minerals such as quartz and feldspar do not exhibit absorption features in the VNIR and SWIR regions. Most of these minerals exhibit fundamental absorption features in the TIR wavelength region. Some of these minerals representing specific lithological units

can be distinguished in standard color-infrared images and in decorrelation-stretch image because of their reflectance, color and textural characteristics (Kalinowski and Oliver, 2004).

There are two scenes available covering almost all part for the study area. The images were projected to UTM zone 36S projection using WGS84 datum. A mosaic was generated from the two scenes at a resolution of 15 m (VINIR), 30 m (SWIR) and 90 m (TIR). The images were variously enhanced and resampled at a resolution of 30 m. A DEM was generated from the near infrared bands of 3N and 3B.

LANDSAT TM IMAGE

Landsat TM images are useful for much wider range of applications. The image has an improved spatial association with increased number of bands. The TM and subsequent Landsat sensors have 7 spectral bands and one panchromatic high resolution band (band 8). Three bands are within the wavelength of visible energy (bands 1, 2 and 3) and three bands of reflected infrared (bands 4 near infrared, 5 and 7 mid infrared) having spatial resolution of 30 meters (Figure 3.5). Band 6 records in thermal infrared at a resolution of 60 m. Band 8 has a relatively high resolution (15 m).

The image covers almost all parts of the study area. Atmospheric corrections and normalization of image were done. The image was projected to UTM zone 36S projection using WGS84 datum. It was subset based on the bounding coordinates of the study area. Different band combinations and band ratio were implemented to increase the interpretability of the image for lithological and structural features.

3.3.2.1. Principal components transformation and interpretations

Images generated by digital data from various wavelength bands in multispectral image often appear similar and mainly transfer the same information. The principal component (PC) is one technique designed to reduce such redundancy in multispectral images. It is a multivariate statistical technique that selects uncorrelated linear combinations (eigenvector loadings) of variables in such a way that each successively extracted linear combinations have smaller variances (Ranjbar *et al.*, 2003). The PC images are uncorrelated linear combinations of the original spectral bands (Kalinowski and Oliver, 2004). Because of the uncorrelated nature of the PC images more colourful colour composite bands are produced.

The Crôsta technique is one of the known techniques for image enhancement based on PC (Crôsta and Rabelo, 1993). The method involves identifying the PC image that has information related to the theoretical spectral signature. According to the sign and magnitude of the eigenvectors, the target material is indicated by dark or bright pixels in the PC image (Carranza and Hale, 2002).

ASTER IMAGE

PCs were calculated using ASTER VNIR and SWIR input spectral bands of the study area (Table 3.1). Statistics were computed and the percentages of data variations were produced. The largest variation is recorded was in the first PC image (98.33%). Very little variance was recorded by PCA which for the most part account to noise. The resulting PC images were generated and enhanced linearly to apply a simple transform.

Table 3-1 Eigenvector loadings of principal components for ASTER VNIR and SWIR data and their variance

Eigenvector	Band 1	Band 2	Band 3	Band 4	Band 5	Band 6	Band 7	Band 8	Band 9	Variance %
PC 1	0.44	0.37	0.35	0.39	0.29	0.31	0.28	0.27	0.24	98.33
PC 2	0.35	0.03	0.71	-0.1	-0.21	-0.29	-0.29	-0.34	-0.19	0.92
PC 3	0.49	-0.58	0.46	0.42	0.09	0.13	0.09	0.03	0.01	0.35
PC 4	-0.5	0.67	0.04	0.36	-0.18	0.03	-0.11	-0.11	-0.32	0.19
PC 5	-0.39	0.22	0.4	-0.64	-0.04	-0.01	0.19	0.38	0.23	0.13
PC 6	0.06	-0.07	0.05	-0.29	-0.06	0.85	-0.1	-0.14	-0.37	0.03
PC 7	-0.17	0.12	0	-0.03	0.18	0.2	-0.45	-0.44	0.7	0.02
PC 8	-0.11	0.08	0.03	-0.19	0.8	-0.16	0.23	-0.36	-0.3	0.01
PC 9	-0.01	0.02	-0.01	-0.01	-0.38	0.05	0.72	-0.55	0.19	0.01

In Table 3.1 PC3 and PC4 show significant high band ratio of 2/1 which enhances rocks containing ferric iron minerals. PC4 and PC5 enhance carbonate minerals. There is major absorption of Mg (OH) bearing (chlorite, talc) and carbonate (calcite, dolomite) minerals in band 8 and 9 and reflectance in band 4. The band ratios 4/8 and 4/9 probably enhances dolomitic rocks in the study area. PC6 represents rocks containing Al-OH (clay) represented as the ratio of band 4 and band 6 (Figure 3.5).

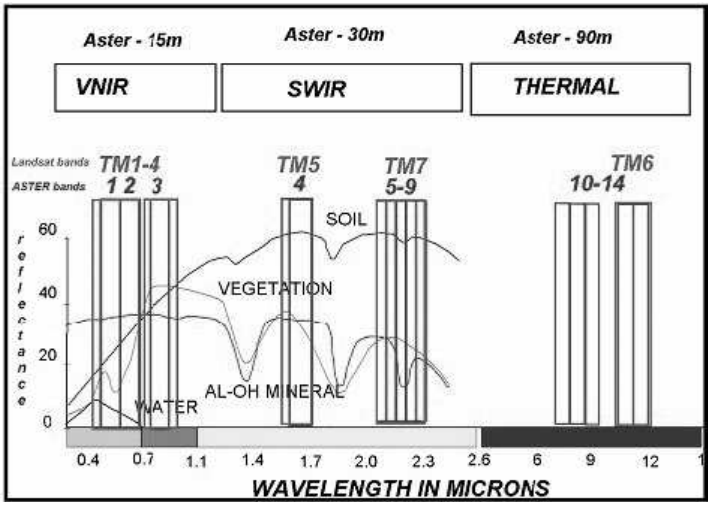

Figure 3-5 Distribution of ASTER and Landsat channels with respect to the electromagnetic spectrum (after Kalinowski and Oliver, 2004).

The combinations of PC bands 2, 3, 4 in RGB order were selected to discriminate surface geology. Red and orange pixels in the east represent dolomite (Figure 3.6). In the southwest, orange pixels correspond to graphitic phyllite. The yellowish brown color pixel to the west and greenish pixels in the north east indicate granitic intrusion. Soil covered areas, in the central part are indicated by purple and green pixels. The green, purple and brown pixels to the west are interpreted as undifferentiated phyllite, graphitic slate, and quartzite.

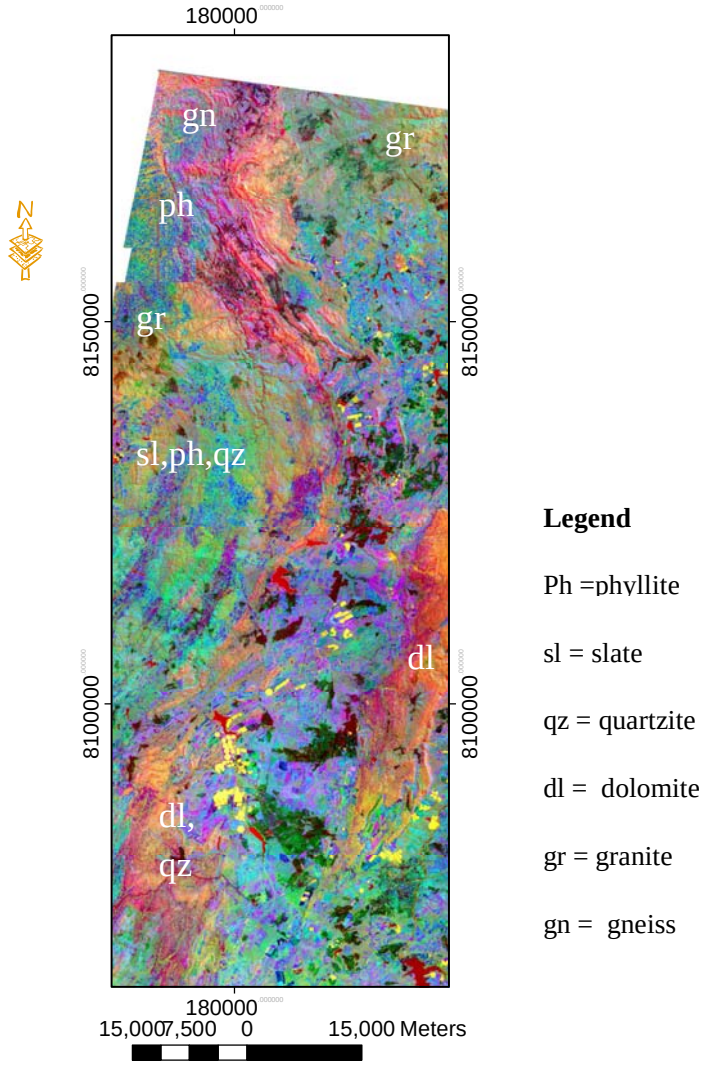

Figure 3-6 PC bands of 234 (RGB) discriminating the lithology of the study area UTM Zone 36S projection, WGS 84 Datum.

LANDSAT TM IMAGE

Principal component analysis was also computed on six bands of Landsat TM (Table 3.2). The first principal component (PC1) represents 88.34% of the total variance of all bands. PC2 contains high

positive loadings on band 3 (0.58) and negative loadings on band 1 (-0.60). Band ratio 3/1 enhances iron oxide minerals (Figure 3.7c). PC4 enhances hydroxyl minerals explained by band 5/7 (Figure 3.7a). The high loadings of band 4 (0.72) and a negative loadings of band 5 (-0.26) also enhances iron oxide minerals (Figure 3.7b). PC band composite of 234 RGB enhance lithological units in the area. Granite, phyllite and dolomitic rocks are discriminated in the PC band combinations (Figure 3.7d).

Table 3-2 Eigenvector loadings of principal components for Landsat TM data and their variance

Eigenvector	Band 1	Band 2	Band 3	Band 4	Band 5	Band 7	Variance %
PC1	0.31	0.11	0.32	0.14	0.71	0.52	88.34
PC2	-0.60	0.40	0.58	0.36	-0.10	-0.04	5.18
PC3	-0.74	-0.27	-0.37	-0.20	0.35	0.30	2.93
PC4	-0.02	-0.14	-0.17	0.48	0.51	-0.68	2.51
PC5	0.05	0.12	-0.49	0.72	-0.26	0.41	0.72
PC6	0.00	0.85	-0.39	-0.27	0.19	-0.13	0.32

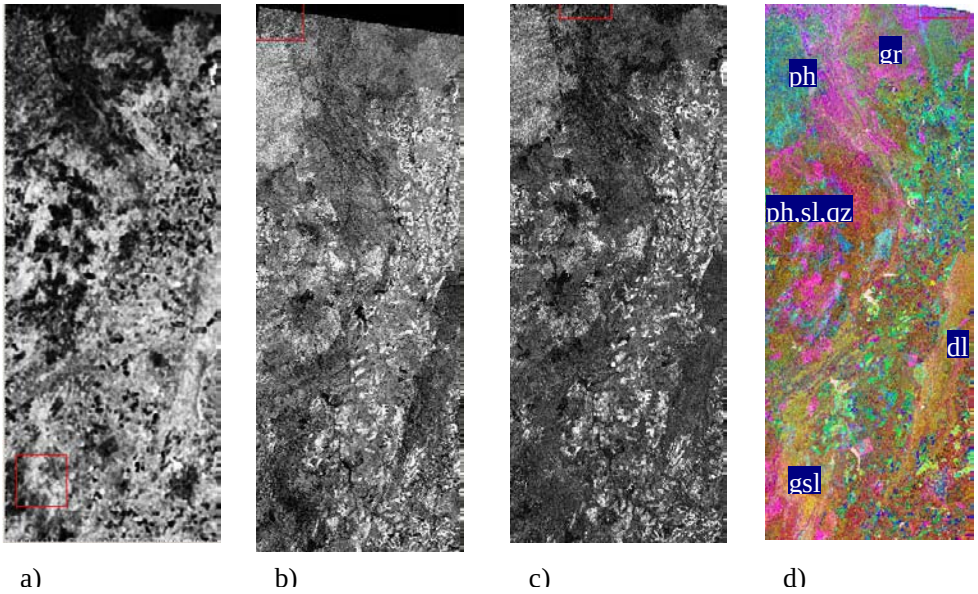

Figure 3-7 PC band images used for lithological interpretation. a) PC4 enhanced clay minerals or Al-OH; b) PC3 enhanced ferrous oxide minerals; c) PC2 enhanced ferric oxides and d) Colour composite PC band image 234 RGB discriminate lithological units in the research area. (Bright pixels shows areas of strong reflectance) (dl= dolomite, sl = slate, ph = phyllite, gsl = graphitic slate, gr = granite).

Rocks containing iron oxides have strong reflectance spectra in the wavelength regions covered by Landsat TM 1 and 2 (Figure 3.8). In vegetated area, these bands show similar reflectance spectra for vegetation. Clay minerals have strong reflectance in band 5 and absorption in the spectral region covered by Landsat TM band 7. In band 3, both iron oxide and clay show strong reflectance spectra and vegetation shows absorption feature. In band 4, vegetation show strong reflectance spectra but absorption feature on clay and iron oxide. Therefore, bands 3 and 4 can be used to differentiate iron oxides and clay rich zone from vegetation in the study area.

Iron oxide probably limonite and clay alteration/weathering zones can be mapped using Landsat TM bands 1, 3, 4 and 5 and 1, 4, 5 and 7 respectively (Crôsta and Rabelo, 1993). The PCA calculated on Landsat TM bands 1, 3, 4 and 5 showed that PC3 represent high positive loadings of band 5 and high negative loadings of band 4 (Table 3.3). Bands ratio 5/4 enhances iron oxide probably limonite (Figure 3.8 and Figure 3.9a). This component discriminate granite, graphitic slate, phyllite and dolomite. These rocks contain iron bearing mineral such as biotite which could weather into iron oxide. The PCA conducted on Landsat TM bands 1, 4, 5 and 7 indicate PC4 contain high positive loadings on band 5 and negative loadings of band 7 (Table 3.4). The ratio between these bands enhanced clay rich rocks (Figure 3.8 and Figure 3.9b). Arkose, granite, and slate which could weather into kaolin are discriminated. The ratio also enhances carbonate rock like dolomite in the eastern parts of the area.

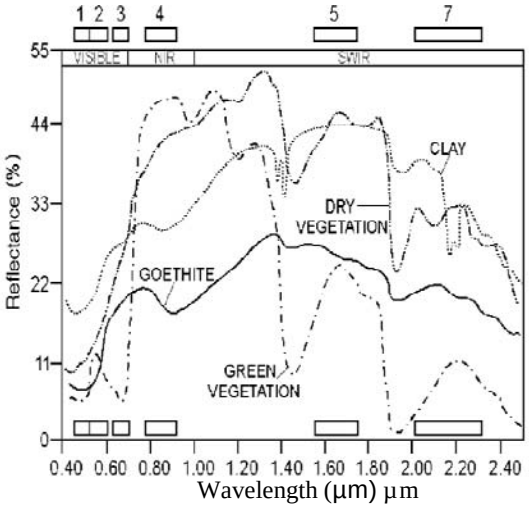

Figure 3-8 Generalized reflectance spectra of vegetation, iron oxides and clays (Fraser and Green, 1987)

Table 3-3 Eigenvector loadings of principal components for Landsat TM bands 1, 3, 4 and 5 data and their variance

Eigenvector	Band 1	Band 4	Band 5	Band 7	Variance%
PC 1	0.34	0.55	0.49	0.58	89.17
PC 2	-0.80	-0.24	0.29	0.47	4.77
PC 3	-0.11	0.31	-0.82	0.47	4.09
PC 4	0.48	-0.74	-0.06	0.48	1.97

Table 3-4 Eigenvector loadings of principal components for Landsat TM bands 1, 4, 5 and 7 data

Eigenvector	Band 1	Band 4	Band 5	Band 7	Variance%
PC 1	0.33	0.46	0.57	0.60	87.22
PC 2	0.24	0.74	-0.07	-0.63	7.53
PC 3	-0.89	0.27	0.36	-0.06	4.18
PC 4	0.21	-0.41	0.73	-0.50	1.07

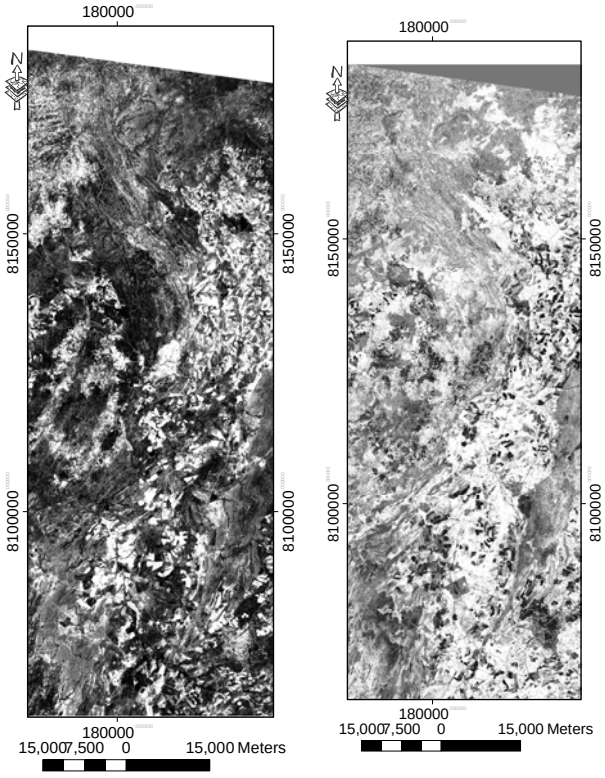

Figure 3-9 PC band images used for lithological interpretation a) PC3 image enhancing iron oxide/limonite b) PC4 enhances clay rich zone (bright pixels shows areas of strong reflectance). UTM Zone 36S projection, WGS 84 Datum.

3.3.2.2. Band combination and lithological interpretations

ASTER IMAGE

ASTER greatly improves the ability for the identification of geological materials with remotely sensed data. However, extracting band combinations that give the best results for lithological information in most cases is difficult (Ren *et al.*, 2001). A total of 364 color combinations (RGB) of 14 bands of ASTER data overlays are obtained using optimum index factor (OIF). It is a statistical approach to rank all possible 3-band combinations based on total variance and correlation coefficient between bands (Ren *et al.*, 2001). The best three-band combinations for lithological mapping were selected by calculating this factor (Chavez *et al.*, 1994). The ratio between the summation of standard

deviation and absolute value of the correlation coefficient between any two of the three bands were calculated. Band combinations 7, 4, 2 and 3, 6, 11 (RGB) with high OIF were selected (Figure 3.10a and b). These band combinations were expected to have the maximum extractable lithological information since they have the least redundancy in the remotely sensed data.

The color composite images of 7, 4, 2 and 3, 6, 11 in RGB mode (Figure. 3.10a and b), discriminate the lithology of the research area. In these images, the granites (north-west and north-east), gneiss and phyllite in the north-west were discriminated. Dolomite is better discriminated from graphitic slate in color composite image 7 4 2 (RGB) than in color composite image 3, 6, 11 (Figure 3.10a and b).

LANDSAT TM IMAGE

Band combinations used for lithological interpretations for Landsat TM images generally include combinations of red, green and blue (RGB) color composites in short wave infrared (SWIR) between 2.08-2.35 micrometer. A color composite image which has high standard deviation with less redundancy (less correlation) is chosen based on OIF calculation. Among ten highest ranked band combination obtained from OIF, band combination 453 (RGB) was found to be the best color composite for lithological mapping (Figure 3.10c).

The color composite image, 453 (RGB) (Figure 3.10c) clearly identifying the geologic units in the study area. Brown pixels in the south-east indicate dolomite. The greenish color pixels to the west represent Late Pre-Cambrian slate, quartzite and phyllite of the Priwiri Group. The darker tone to the north represents the Pre-Cambrian gneissic rocks. In the central and eastern portions, bright white features with green background indicate cultivated areas. These areas were mapped as arkose to the south and granite to the northeast. The contact between these two units using both band combinations was difficult due to mixed spectral features contributed by surface activities.

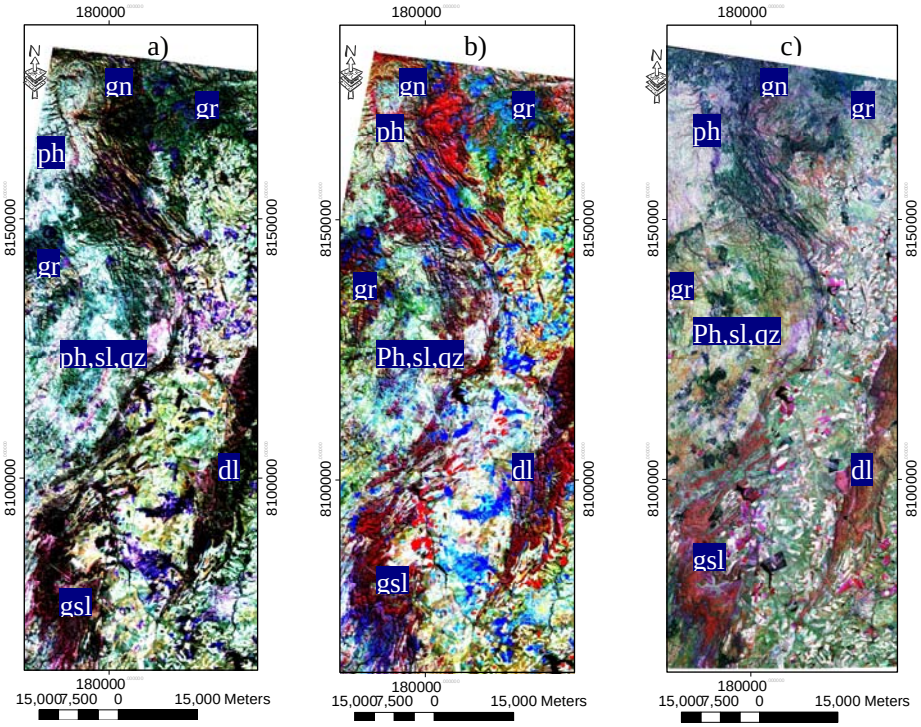

Figure 3-10 Interpreted images of band combination a) ASTER 7, 4, 2 (RGB); b) ASTER 3, 6, 11 (RGB) ; and c) Landsat TM 4, 5, 3 RGB UTM Zone 36S projection, WGS 84 Datum). (dl= dolomite, sl = slate, ph = phyllite, gsl = graphitic slate, gr = granite, gn = gneiss).

3.3.2.3. Band ratio images and interpretations

Detection of spectrally similar features can be enhanced by the use of band ratios. Band ratio is one type of techniques the enhancement of image resulting from division of digital number (DN) values in one spectral band by the corresponding values in another band. Ratio images convey the spectral or colour characteristics of image features, regardless of variations in scene illumination conditions, which is the major advantage of band ratio (Lillesand and Kiefer, 1987). Band ratios 5/7, 5/4 and 3/1 enhances clay minerals (pyllosilicates), ferrous and iron oxides, respectively (Sabins, 1987). There is iron oxide absorption between 0.85-0.92 in band 4 and no absorption in band 5. The ratio between these bands therefore enhances rocks rich in iron oxide. Color composite image of these band ratio discriminate granite, gneiss, basic igneous rocks, dolomite and arkose in the study area (Figure 3-11d). Clay/kaolinite can be obtained from weathering products of feldspar bearing arkose, gneiss and granite (Figure 3.11a). Biotite bearing quartzite, gneiss and granite can easily weather into iron oxide (Figure 3.11b and c). Combinations of band ratio 3/1 red, 5/4 green and 5/7 blue were used to identify lithological units in the area. The blue pixels represent dolomite and graphitic slate and orange phyllite and green granite and gneiss (Figure 3.11d).

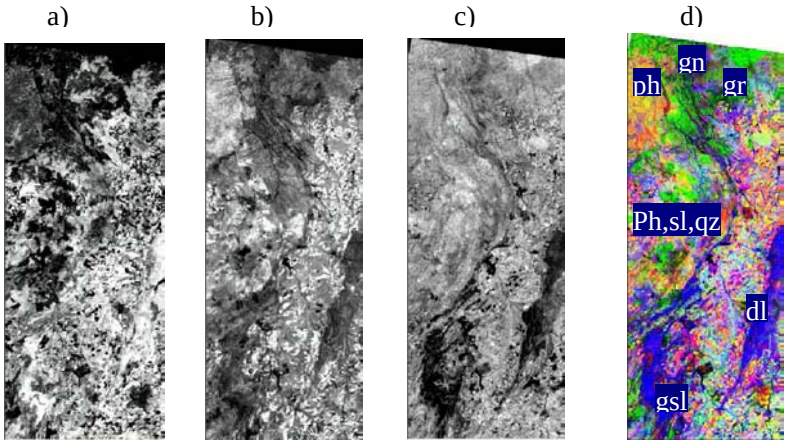

Figure 3-11 Showing different band ratio and band combinations of Landsat TM a) Band ratio 5/7 indicating clay rich minerals; b) ratio 3/1 enhancing iron oxide rich rocks; c) ratio 5/4 enhances iron oxide and d) color composite ratio images of combination of ratios 5/7, 3/1 and 5/4 RGB discriminating lithology(bright pixels shows areas of strong reflectance) (dl= dolomite, sl = slate, ph = phyllite, gsl = graphitic slate, gr = granite, gn = gneiss)

3.3.3. Digital Number for multispectral image

Individual multi spectral bands can be used to identify lithological units based on their spectral characteristics. Mean digital number (DN) values of both Landsat and ASTER images were calculated and the statistical results were plotted (Figure 3.12 and3. 13). As can be seen from the graphs in Figure 3.12, slate (sl) and graphitic slate have highest and lowest DN values in Landsat TM, respectively. In ASTER image, on the other hand, phyllite (ph) and dolomite (dl) have lowest and highest DN values respectively. According to the graphs in Figure 3.12 and 3.13, Landsat TM bands TM1, TM3, TM5 and TM 7 and ASTER bands 3,5,6,7 and 11 are relatively the most useful bands for discriminating major lithologic units and can thus be used for classification of major lithological units.

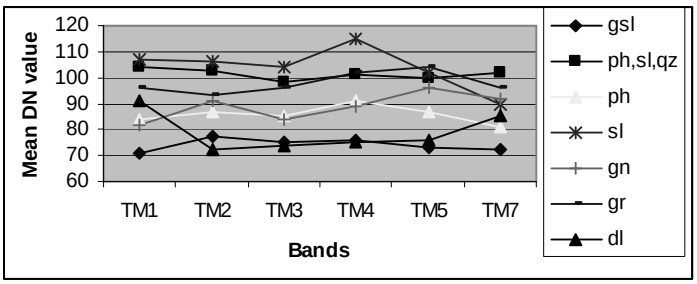

Figure 3-12 Mean DN values of lithologic units in individual spectral bands of Landsat TM

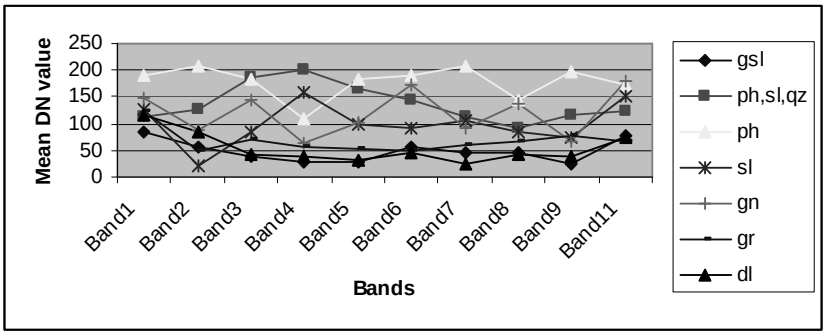

Figure 3-13 Mean DN values of major lithologic unit in ASTER 11 bands VNIR, SWIR and TIR (Band 11)

3.3.4. Image classification

Image classification is the most common analysis of multispectral remotely sensed data in order to produce thematic maps that provide representation of the spatial distribution of a particular theme (Foody and Mathur, 2004). Multispectral classification is useful to obtain information with respect to ground cover and surface characteristics. It helps translate continuous variability of image data into map patterns that provide meaning to the user.

Supervised classification techniques were used to map lithological units from the Landsat TM and ASTER images of the research area. A maximum likelihood classification was used since this classifier considers the shape, size and orientation of the cluster as well as variability with in the cluster. Training sets for nine classes of lithological units were used based on the available field observation datasets (Appendix B). Input bands determined in the above mean DN values for lithological units were used. TM1, TM3, TM5 and TM7 for Landsat TM and bands 3, 5, 6, 7 and 11 for ASTER images were used in the classification (Figure 3.14). The results indicate that the classification discriminates major lithological units in both images. The individual lithological units are better discriminated in ASTER than in Landsat TM. Dolomite and graphitic slate, which were classified as one unit in the Landsat TM image (Figure 3.14a), were separately classified in ASTER image (Figure 3.14b).

Accuracy assessments conducted on both classified images indicate 32% and 38% overall accuracy for Landsat TM and ASTER images, respectively. These low values are due to the fact that the areas, especially the south central part are extensively covered by agriculture (soil cover); the Piriwiri rocks in the western part are undifferentiated, and the northern parts are relatively vegetated and have different topography. Due to all these factors, the rock units are spectrally less separable.

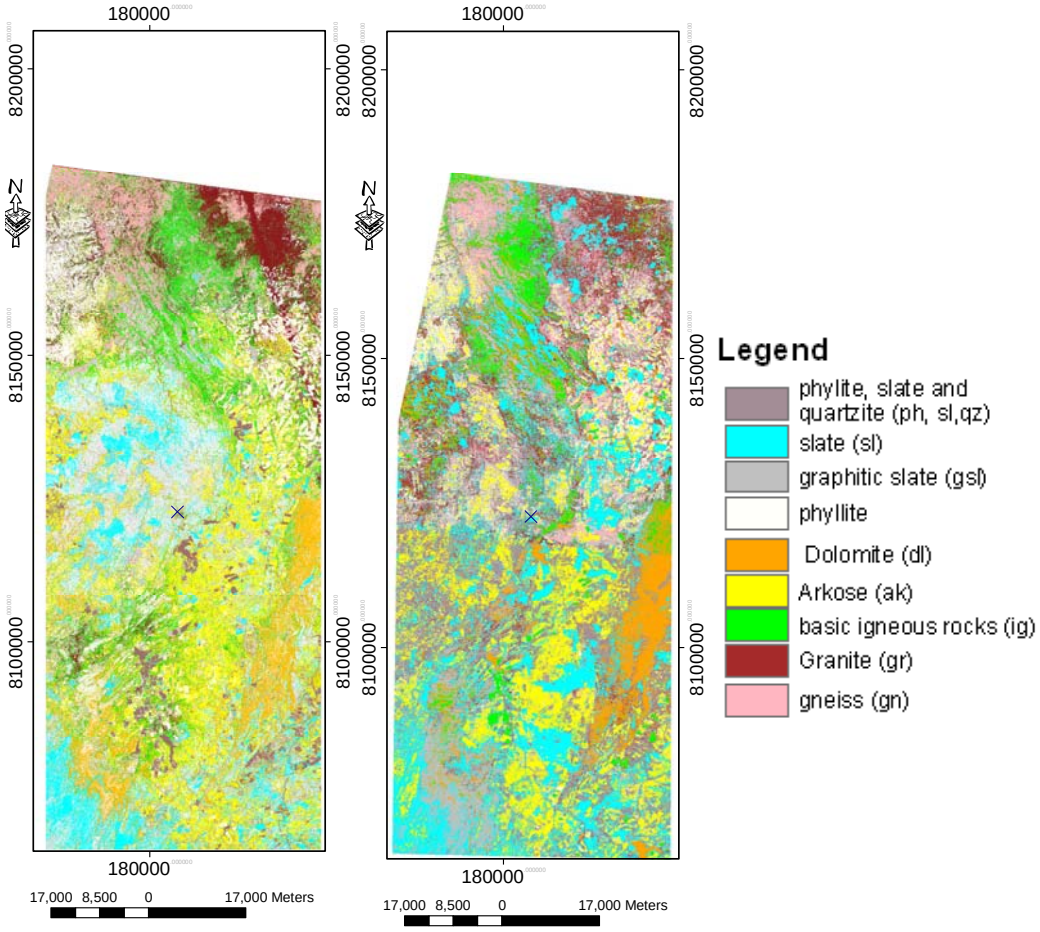

Figure 3-14 Classified images using supervised classification (Maximum likelihood classifications); a) Landsat TM and b) ASTER, UTM Zone 36S projection, WGS 84 Datum.

3.3.5. Processing and interpretation of Shuttle Radar Topography Mission (SRTM) and ASTER DEM images

The Shuttle Radar Topography Mission (SRTM) obtained elevation data on a near-global scale to generate the most complete high-resolution (90 m) digital topographic database of the Earth. ASTER DEM was generated from the near infrared bands of 3N and 3B at a resolution of 30m. The images were projected to WGS 84 datum, UTM zone 36S projection. Due to the difference in resolution between the two images topographic features are seen at different scale. As can be seen from Figure 3.15a, finer details can be observed on the ASTER DEM than on the SRTM DEM. Major structural features, such as faults, topographic differences are easily seen on SRTM; since these features cover large areas (Figure 3.15b). ASTER DEM image covers almost all the study area as compared to SRTM (Figure 3.15).

Predominantly NW and NE lineaments were interpreted in rocks of arkose, dolomite slate, basic igneous rocks and gneisses. In the south western area tight folded structures in quartzite are clearly seen on hill-shaded image of ASTER DEM (Figure 3.15a). The structures can easily be seen in large scale to the north folding the NE trending general lineaments to NW. Major lineaments/fractures probably faults, are clearly seen on SRTM (Figure 3.15b). All interpreted features were compiled to produce lineament map of the study area (Figure 3.15c). These tectonic structures are comparable with those structures stated in Section 2.5.

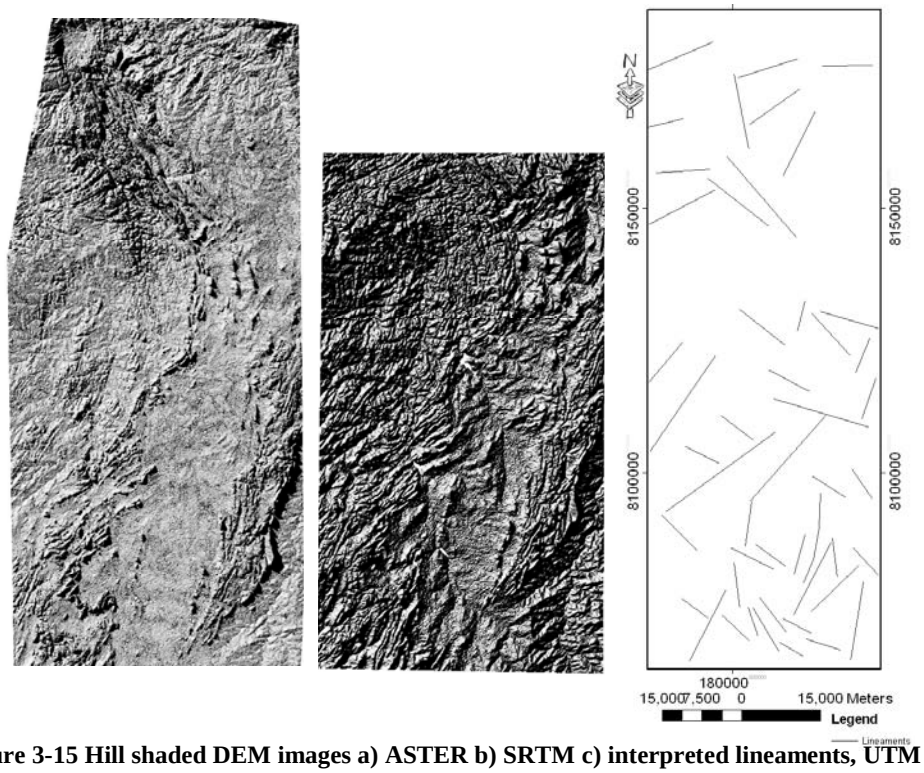

Figure 3-15 Hill shaded DEM images a) ASTER b) SRTM c) interpreted lineaments, UTM Zone 36S projection, WGS 84 Datum.

3.3.6. Processing and interpretation of aeromagnetic data

The capability of high resolution aeromagnetic data to accurately map a single geological feature over a wide and covered area makes it suitable for structural and lithologic mapping at various scales. The residual total magnetic field map is useful for geological mapping because it reflects physical properties of the underlying rocks.

Airborne magnetic survey was conducted on May 1976 in southern parts of the study area, where lithologies are extensively covered by soil. A high resolution aeromagnetic grid covers 530 km^2 areas in the southern parts of the study area (Figure 3.16). The data were collected by helicopter at a speed of 140 km/h with constant flight-line orientations, and at one second sampling interval. It was flown at an altitude of 61 m above ground level with a line spacing of 150 m. Magnetic total field grid, profile map and different raster maps of color shaded relief were produced to help visualize and interpret the

aeromagnetic data of the study area. The profile map represents all data recorded along the lines showing the shape and source of the magnetic anomalies (Figure 3 16a).

3.3.6.1. Aeromagnetic database and generation of grid

The aeromagnetic data obtained in xyz ASCII file format were imported and a database was generated in Oasis Montaj. Before generating the magnetic total field grid, the data were sorted to remove back tracks. A non-linear filtering was also conducted to remove data spikes (undesired high-amplitude short-wavelength features) from the original data. The girding process was carried out in two principal steps. First, each line was interpolated along the original survey line to yield data values at the intersection of each required grid line with the observed line. The intersected points in each line were then interpolated in the across-line grid direction to produce a value at each required grid point. Geological trends in the data can be emphasized by the appropriate orientation of the grid so that the second interpolation is in the direction of strike. Peak on the profile indicate high magnetization (Figure 3 16a).

3.3.6.2. Applying filters to enhance aeromagnetic images

Magnetic anomalies are displayed as color composite and intensity-hue-saturation images. By displaying anomalies as color and grey-scale images, contour and profiles can be achieved by filtering and enhancing through a series of processing techniques applied on data. In this research studies, color image of unfiltered total magnetic grid (Figure 3.16b) and filtered color shaded vertical derivative and analytical signal were used for interpretation.

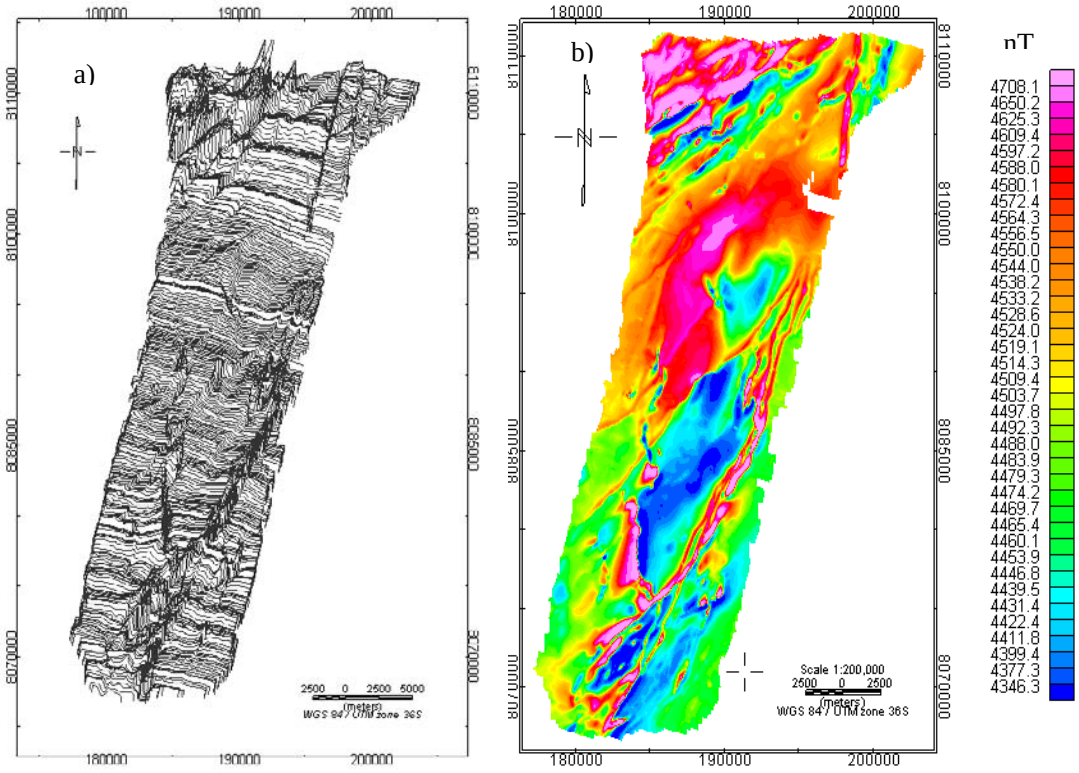

Figure 3-16 Magnetic total field image a) profile map showing the shape of the magnetic anomalies; and b) unfiltered total magnetic grid of Magondi-Belt, Zimbabwe

Vertical derivative

Vertical derivative is commonly applied to total magnetic field data to enhance shallow geological features. It suppresses the deeper features and helps to identify closely spaced sources by giving a better resolution. Color and grey scale shaded images of the vertical derivative help to identify and interpret linear features like faults and joints/fractures (Figure 3.17a). They are useful in outlining the boundaries of linear structural features, which are not clearly visible in the total magnetic grid. Faults are recognized by relative shifts and interruptions along the continuity of linear geologic features. Based on these characteristics linear features like fault and dykes are interpreted from the color shaded relief image of vertical derivative (Figure 3.17a).

Analytical signal

The analytical signal calculates the analytic signal of a channel. It can be useful in locating edges of remanently magnetized bodies in areas of low magnetic latitude. It is also useful for structural and lithological interpretation. The analytical signal of total magnetic field of the study area identifies the lithological boundaries (Figure 3-17b). The lithologic units were recognized from the changes in the

characteristics of the aeromagnetic field from one lithology to another. High magnetizations are due to rocks containing ferromagnesian minerals. Doloritic dikes and basic igneous rocks, which are associated with the Deweras Group, were interpreted as rocks containing these minerals. Intermediate and low magnetizations were interpreted as rocks of arkose and dolomite (Figure 3.17b and Figure 3.18). Previous works (Carballo Lopez, 1998) showed that these rocks occur together in the study area and the former has minerals which have relatively moderate magnetic response (Telford *et al.*, 1990).

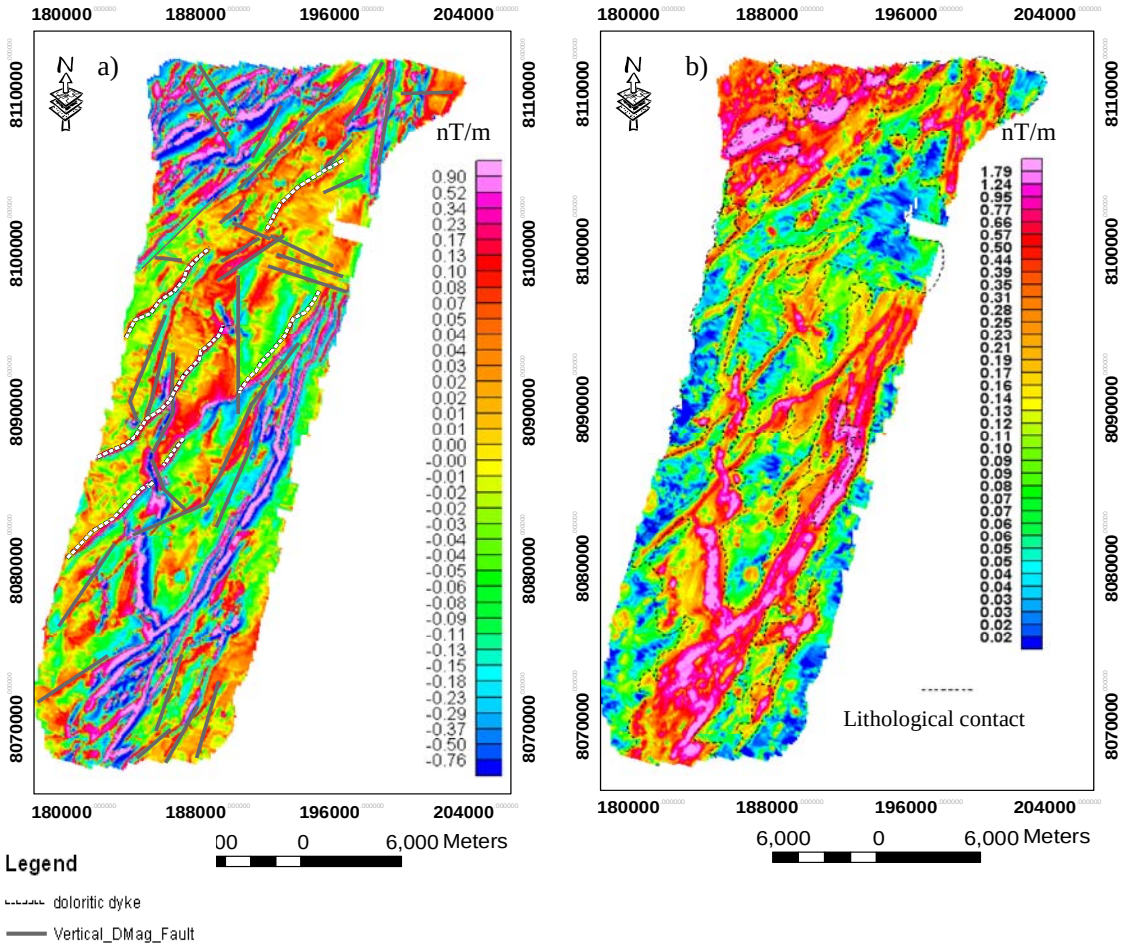

Figure 3-17 Color shaded relief image of the total magnetic field a) first vertical derivative indicating interpreted lineaments and doloritic dykes b) analytic signal showing interpreted lithologic boundaries (illumination inclination, I=45 and declination 315).

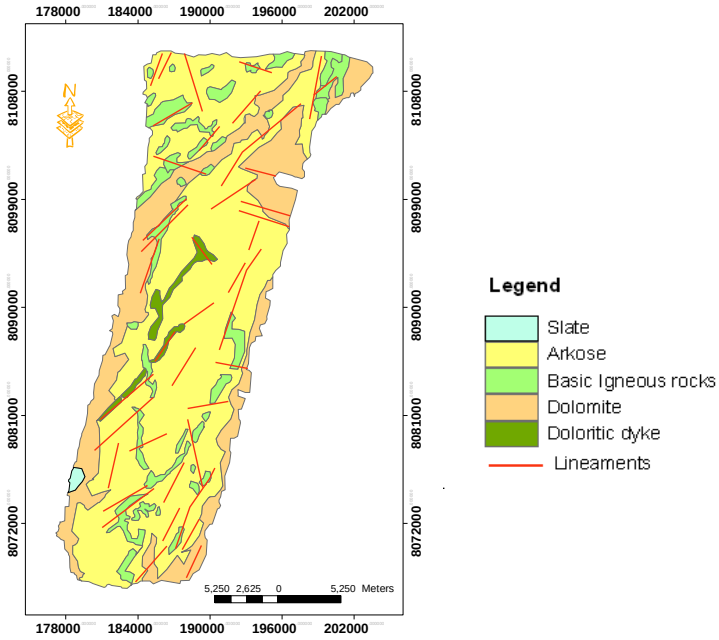

Figure 3-18 Interpreted lithology and lineaments from aeromagnetic data

3.3.7. Geochemical data processing and interpretations.

Geochemical soil sampling has long been a technique to indicate the distribution of background and anomalous element concentration of underlying lithology in order to predict the possible potential of mineralization (Govett, 1976). Geochemical soil survey was conducted in Magondi Belt. The area extends from Shamrock, in the north, to Alaska in the south. The survey was carried out in four areas namely: Alaska, Umboe, Mhangura and Shamrock (Figure 3.19). A total of 3,676 soil samples were collected covering an area of 919 km^2. Sampling was conducted at grids of approximately 500X500 meters. Soil samples, each weighing about one kilogram, were collected at a depth of one to six meters. The samples were chemically analysed for nine elements (Cu, Pb, Zn, Fe, Co, Ni, As, Au, and Ag). Statistical analyses of all element concentration data were carried out for each dataset to determine anomalous areas. Threshold values were calculated to determine the anomaly. These values are values above which values are considered anomalous. Soil samples which contain censored values of elements were set to half of their detection limit (Kambewa, 1998). Bivariante and multivariate analysis were not conducted for As, Au and Ag because of these values below detection limit (Kambewa, 1998).

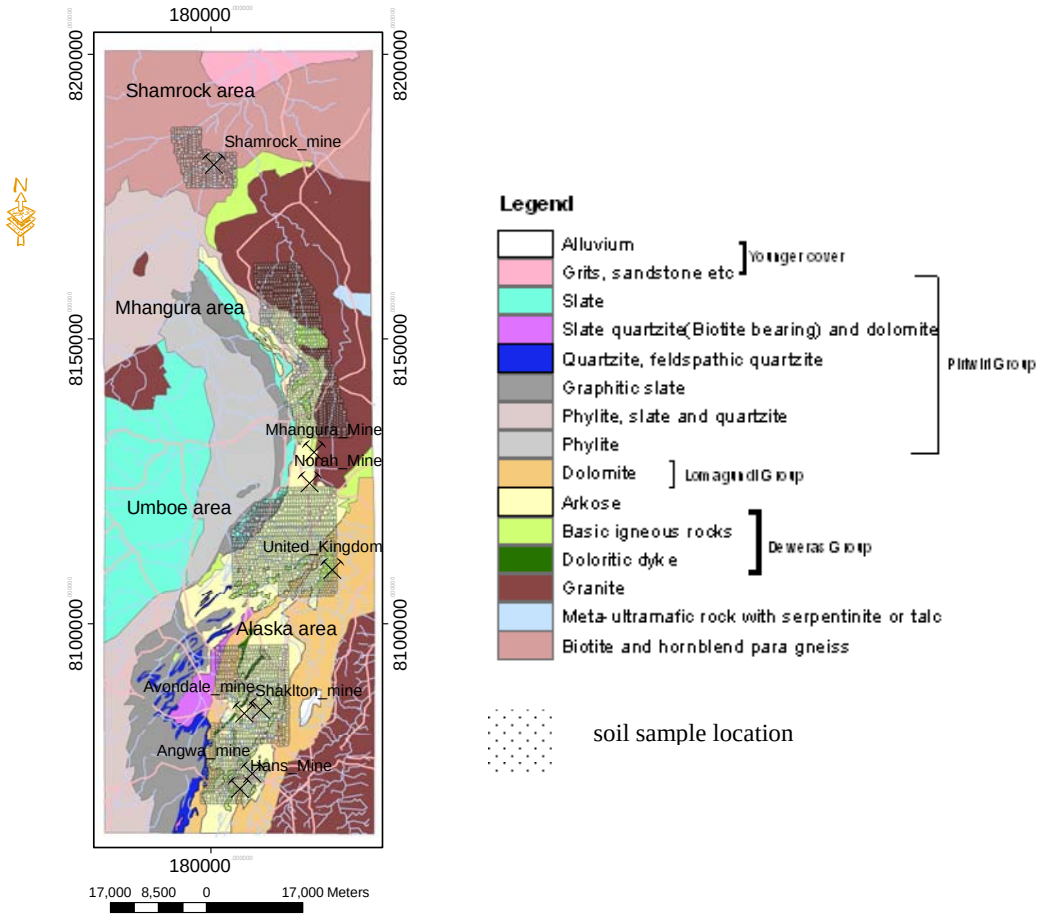

Figure 3-19 Geochemical soil sample location map of Magondi Belt

3.3.7.1. Univariate statistics

A graphical inspection of geochemical data is necessary as the first step in data analysis (Reimann *et al.*, 2005). Graphical techniques are used to examine the shape of the distribution of univariate data to give the first impression to the distribution of the data (Reimann and Filzmoser, 2000). The geochemical soil sample data of the research area were first plotted as frequency histogram to inspect the distribution. The result indicates that most of the elements show one to two population, positively skewed, containing relatively large maximum values with respect to the mean. The data were then log transformed to improve the distribution close to normal. More than half of the total samples of As, Ag and Au, in all four areas contain values below detection limit. Analysis of these elements were carried out after removing censored data, since normal distribution can not be approached if there are more values (>25%) below detection limit (Reimann and Filzmoser, 2000).

Histogram and box plots were used to visualize the distribution and determine the outliers. The box plots for Cu, Zn, Ni, Au and Ag indicate significant outliers which could determine the anomaly concentrations. Outliers in such geochemical datasets can be used as indicative of ore deposit (Reimann and Filzmoser, 2000). Box plot is used as a method to select the anomaly threshold (Yusta *et al.*, 1998; Bounessah and Atkin, 2003; Reimann *et al.*, 2005). Figure 3.20 shows different parts of an idealized population standardized to the anomaly threshold. The median for each dataset indicate the line in the middle of the box plot (Q2). First and third quartiles are the edge of the box represented by Q1 and Q3 and is known as inter quartile range (IQR). The extreme values, within 1.5 IQR are the

end of the lines extending from IQR. Extreme values plotted with different symbols can represent potential anomalies.

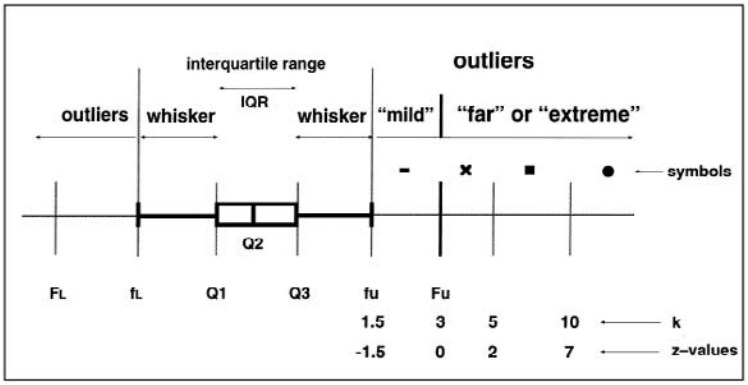

Figure 3-20 Indicating Box plot of an idealized population standardized to the anomaly threshold Fu and the spread Measure (after Yusta *et al.* 1998).

Values above inner and outer fences are represented as 'fu' and 'Fu' respectively (Figure 3.20). Outliers determined as inner and outer fences are defined by the following equation:

Inner fences fl=Q1-kIQR; fu=Q3+kIQR with k = 1.5 *[A]*

or simply *fl=2.5 Q1-1.5 Q3; fu=2.5 Q3-1.5Q1*

Outer fences: Fl=Q1kIQR; Fu=Q3+kIQR, with k = 3 *[B]*

or simply Fl=4 Q1-3 Q3; Fu=4 Q3-3 Q1

Where *Q1* and *Q3* are the lower and upper quartiles of the data, equal to the 25th and 75th percentiles, and the inter quartile range *IQR* is *Q3-Q1; 3* is adopted for outer fences as constant k. The Equation Fu is therefore taken in this research to determine positive anomalies in the study area (Yusta *et al.*, 1998).

Distribution of copper

The summary statistics are computed on log transformed data based on box plot using equation *[B]*. The graphical inspection of data made on frequency histogram and box plot shows, all datasets except Umboe have one population and are normally distributed (Figure 3.21). Outliers on high end represent anomalous values. The thresholds were calculated as 123, 166, 153.8 and 162 ppm for Alaska, Umboe, Mhangura and Shamrock areas respectively (Table 3.5). About 54 samples of Alaska have values greater than the anomaly threshold, which is 5% of the total samples. The number of samples with Cu value above threshold for Umboe, Mhangura and Shamrock are 14, 37 and 10, respectively. In both Mhangura and Shamrock, 4% of the total samples Cu values above the threshold values.

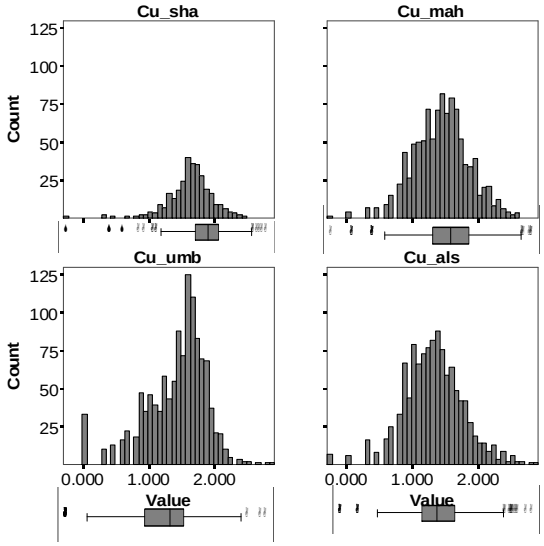

Figure 3-21 Frequency histogram and box-plot showing distribution of Cu on log transformed data Circles in box plot represents outliers representing values above threshold. For a better representation see Appendix A. als=Alaska, umb=Umboe, mha=Mahangura and sha=Shamrock.

Table 3-5 Summary statistics of Cu on box plots on log transformed data

Area	Number of samples	Minimum value (ppm)	Maximum value (ppm)	Geometric mean (ppm)	lower quartiles Q1 (ppm)	upper quartiles Q3 (ppm)	threshold (ppm)
Alaska	1143	0.5000	757	21	11	39	123
Umboe	1189	1.000	819.000	26.2	14	52	166
Mhangura	1032	0.500	411.000	27.1	15	49.7	153.8
Shamrock	312	0.500	290.000	42.3	30	63	162

Anomaly map for copper indicate that all anomalous samples in the Alaska area lie on arkoses and basic igneous rocks of the Deweras Group (Figure 3.23). In Umboe, anomalous values are concentrated along the contact zone of arkose, graphitic phyllite and slate. The anomalies of copper in Mhangura are found in arkoses and granitic intrusion along the contact (Figure 3.23). In Shamrock area, the copper anomalies occur within biotite and hornblende para-gneiss and along the contact with basic-igneous rock.

Distribution of zinc (Zn)

The frequency histogram of Zn in all four areas indicates more than one population. The Umboe data represent three population and the other three areas contain two populations (Figure 3.22). The threshold values chosen for Alaska, Umboe, Mhangura and Shamrock are 164, 271, 281 and 43, 8

respectively (Table 3.7). In Alaska, Mhangura and Shamrock, 6% samples have Zn values above the threshold. About 9% of the samples in Umboe have Zn values above the threshold.

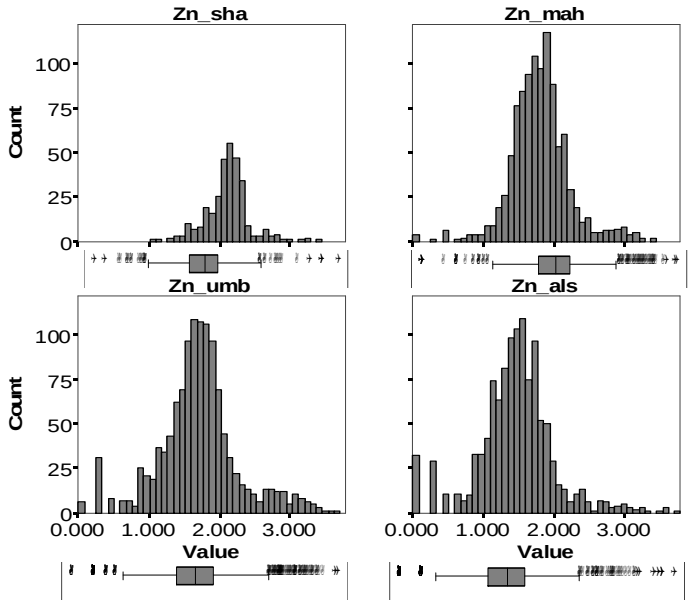

Figure 3-22 Frequency histogram and box-plot of Zn on log transformed data. Outliers and extreme values on high end on both box plot and histogram show anomalous values. For a better representation see Appendix A. als=Alaska, umb=Umboe, mha=Mahangura and sha=Shamrock.

Table 3-6 Summary statistics of zinc (Zn) on log transformed data

Area	Number of samples	Minimum value (ppm)	Maximum value (ppm)	Geometric mean (ppm)	lower quartiles Q1 (ppm)	upper quartiles Q3 (ppm)	threshold (ppm)
Alaska	1143	1.0000	6287.0000	28.9	16	53	164
Umboe	1189	1.000	4438.000	51.1	27	88	271
Mhangura	1032	1.000	2667.000	64	37	98	281
Shamrock	312	12.000	2590.000	131.1	98	183	438

The geochemical map of Zn shows anomalous values found within arkose, basic igneous rock and dolomite (Figure 3.23). Concentrations of Zn anomalies occur in the Piriwiri Group rocks of phyllite, graphitic phyllite and slate in Umboe area. In Mhangura, anomalies are scattered in granite and arkosic rocks. There occur spatial association between the anomalous concentration of Cu and Zn in all areas (Figure 2.23).

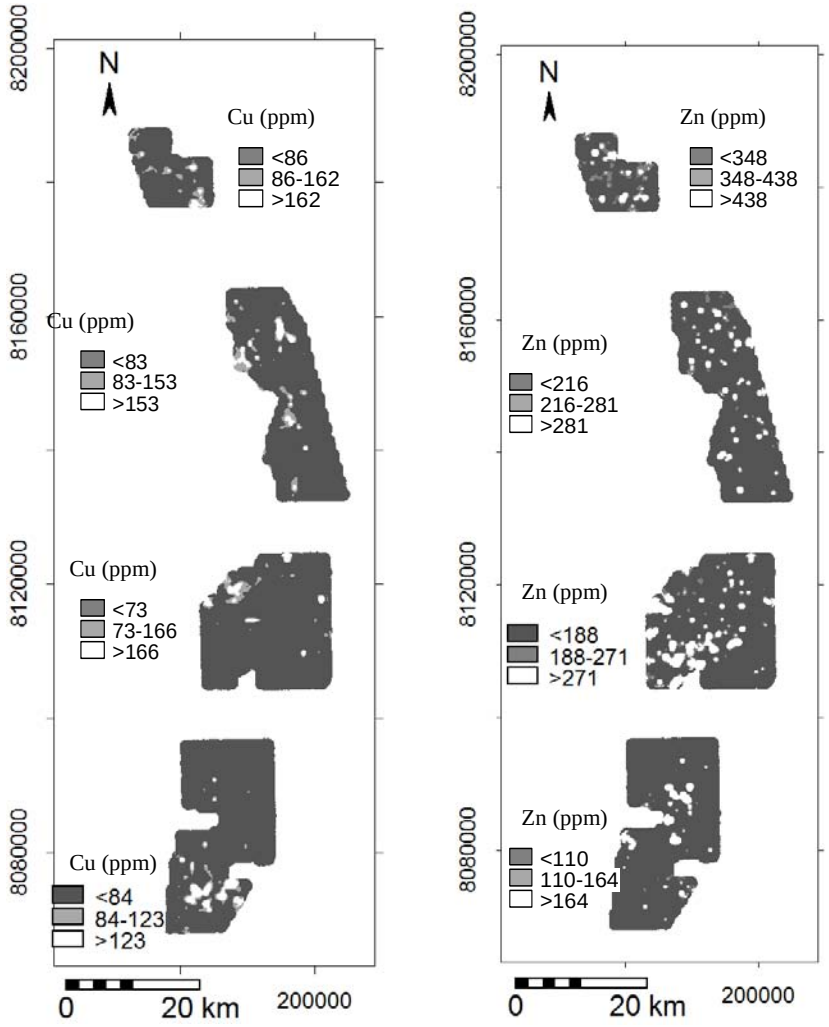

Figure 3-23 Geochemical anomaly map a) Copper (Cu); and b) Zinc (Zn). Magondi Belt, UTM Zone 36S projection, WGS 84 Datum.

Distribution of Pb

The frequency histogram and box plot of lead (Pb) in all areas show at least two populations (Figure 3-24) According to the graphical representations and calculation made on the datasets, no samples have Pb values above the threshold (Table 3.6, Figure 3.24). There are no outliers representing anomalous values on the box plots.

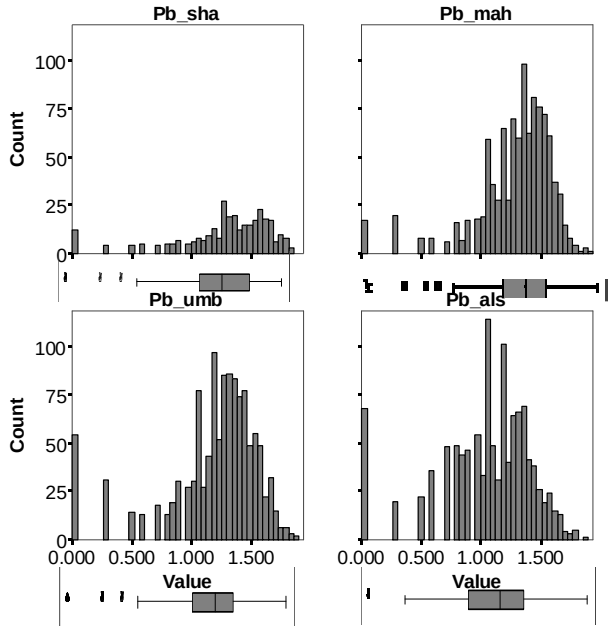

Figure 3-24 Frequency histogram and box-plot of Pb on log transformed data. For a better representation see Appendix A. als=Alaska, umb=Umboe, mha=Mahangura and sha=Shamrock.

Table 3-7 Summary statistics of lead (Pb) on log transformed data

Area	Number of samples	Minimum value (ppm)	Maximum value (ppm)	Geometric mean (ppm)	Standard Deviation (ppm)	lower quartiles Q1 (ppm)	upper quartiles Q3 (ppm)	threshold (ppm)
Alaska	1143	1.0000	73.0000	11.2	2.5	7	21	73
Umboe	1189	1.000	78.000	27.95	2.5	12	29	80
Mhangura	1032	1.000	78.000	19.3	2.1	14	32	86
Shamrock	312	1.000	72.000	19.2	2.5	14	38	110

Distribution of iron (Fe)

The frequency histogram of log transformed data of Mhangura represents one population. At least two populations are present in the Alaska, Shamrock and Umboe datasets (Figure 3.25). About 5.4, 10.6, 8.2 and 11.9 % threshold values of Fe were computed from summary statistics for Alaska, Umboe, and Mhangura and Shamrock areas, respectively (Table 3.8). Only the Alaska datasets contains values above threshold (Figure 3.25). Out of the total samples of Alaska, five samples are anomalous for Fe. The box plot of Alaska also shows few outliers representing anomalous Fe values (Figure 3.25). The anomalous Fe values are found in south central part of Alaska (Figure 3-26).

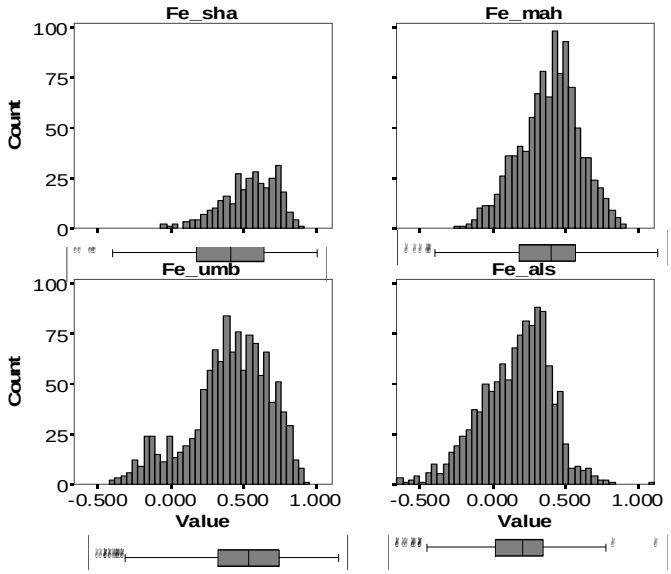

Figure 3-25 Frequency histogram and box-plot of Fe on log transformed data showing anomalous values of Alaska on extreme end. For a better representation see Appendix A. als=Alaska, umb=Umboe, mha=Mahangura and sha=Shamrock.

Table 3-8 Summary statistics of iron (Fe)

Area	Number of samples	Minimum value (%)	Maximum value (%)	Geometric mean (%)	lower quartiles Q1 (ppm)	upper quartiles Q3 (ppm)	threshold (ppm)
Alaska	1143	0.2200	13.0000	1.4	1	2.1	5.4
Umboe	1189	0.390	8.580	2.5	1.8	4	10.6
Mhangura	1032	0.570	7.990	2.5	1.8	3.4	8.2
Shamrock	312	0.890	8.250	3.5	2.7	5	11.9

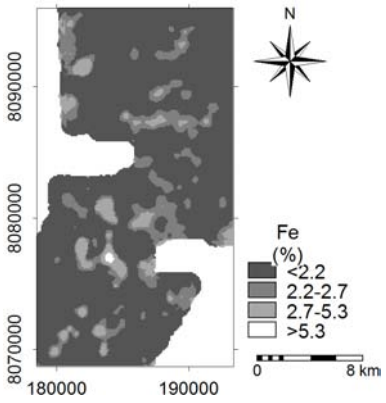

Figure 3-26 Fe anomaly map of Alaska, Magondi Belt, UTM projection, WGS 84 Zone 36S. Bright area indicates anomalous concentration.

Distribution of Cobalt (Co)

The log transformed data of Co shows distribution close to normal with few small values at the low end (Figure 3.27). Threshold values of 25, 46, 38 and 46 ppm are computed from the Alaska, Umboe, and Mhangura and Shamrock datasets, respectively (Table 3.9). Only one sample in each of the Umboe and Shamrock datasets has Co value above the threshold. Two samples in the Alaska datasets are anomalous. There is no sample which shows Co values above the threshold in Mhangura. In both areas of Alaska and Umboe, the Co anomalies lie on the basic igneous rocks.

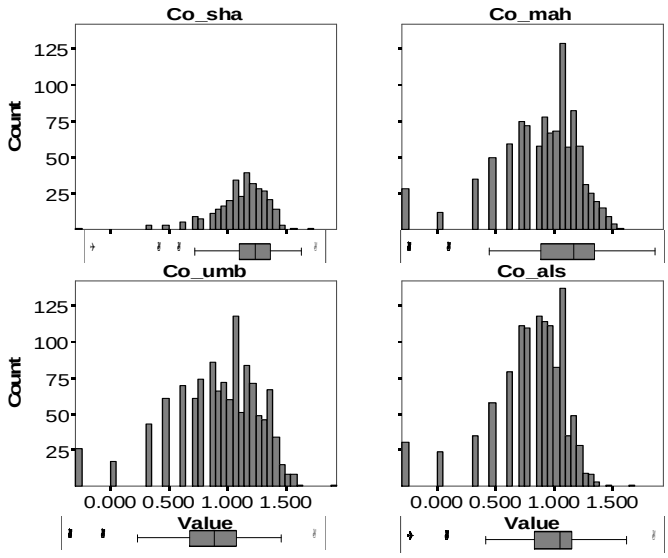

Figure 3-27 Frequency histogram and box-plot of Co on log transformed data showing very little anomalous concentration on high end. The box plot on Mhangura shows no anomaly. For a better representation see Appendix A. als=Alaska, umb=Umboe, mha=Mahangura and sha=Shamrock.

Table 3-9 Summary statistics of Cobalt (Co) computed based on equation [B]

Area	Number of samples	Minimum value (ppm)	Maximum value (ppm)	Geometric mean (ppm)	lower quartiles Q1 (ppm)	upper quartiles Q3 (ppm)	threshold (ppm)
Alaska	1143	.5000	47.0000	6.6	5	10	25
Umboe	1189	.500	85.000	8.7	6	16	46
Mhangura	1032	.500	38.000	7.9	5	13	38
Shamrock	312	.500	50.000	12.9	10	19	46

Distribution of nickel (Ni)

The frequency histograms of Ni in all four areas show normal distribution (Figure 3.28). The threshold values calculated for Alaska, Umboe, Mhangura and Shamrock are 202, 174, 189 and 149 ppm, respectively (Table 3.10). About 14 samples in the Alaska and Mhangura dataset have Ni values greater than the threshold. A total of 20 samples in Umboe datasets are anomalous. Only four samples dataset in the Shamrock are anomalous. The anomalous concentration of Ni in the Alaska, Mhangura and Umboe areas are associated with arkose and basic igneous rocks. In Alaska and Umboe, the Ni concentrations show an east west trend (Figure 3.29).

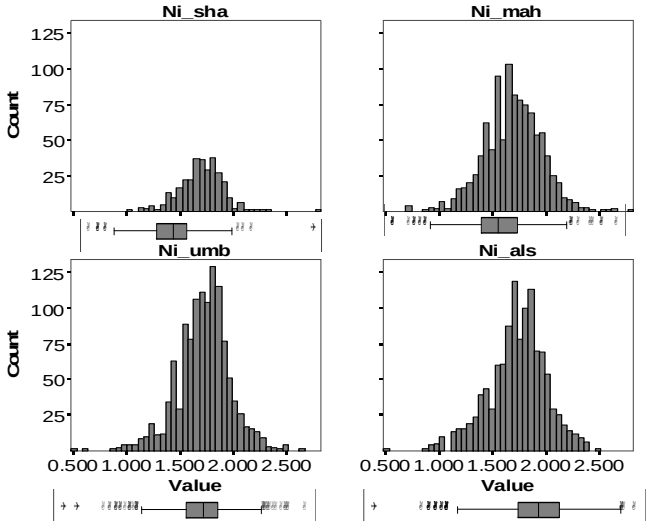

Figure 3-28 Frequency histogram and box-plot of Ni on log transformed data. Extreme values on high end indicate anomalous concentration. For a better representation see Appendix A. als=Alaska, umb=Umboe, mha=Mahangura and sha=Shamrock.

Table 3-10 Summary statistics of nickel (Ni)

Area	Number of samples	Minimum value (ppm)	Maximum value (ppm)	Geometric mean (ppm)	lower quartiles Q1 (ppm)	upper quartiles Q3 (ppm)	threshold (ppm)
Alaska	1143	3.0000	301.0000	53.4	38	79	202
Umboe	1189	3.000	447.000	52	38	72	174
Mhangura	1032	5.000	616.000	48.1	33	72	189
Shamrock	312	11.000	658.000	49.3	37	65	149

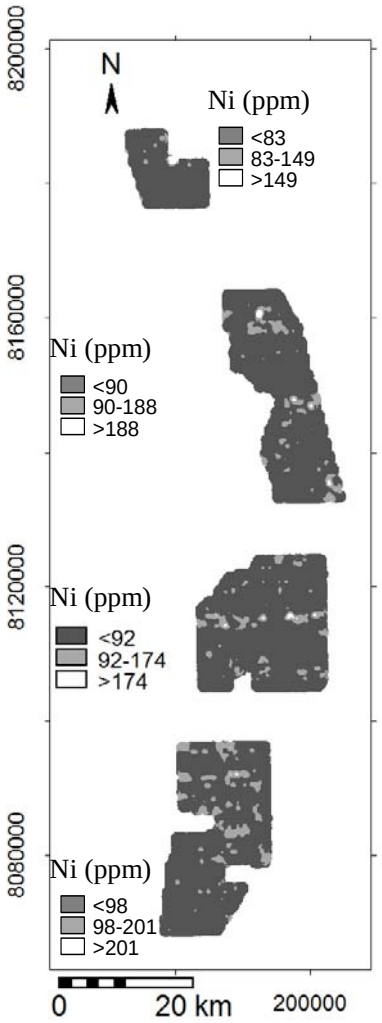

Figure 3-29 Nickel anomaly map of Magondi Belt, UTM Zone 36S projection, WGS 84.

Distribution of arsenic (As)

Seventy percent of the values in the Alaska and Mhangura dataset are below detection limit. The values of As below detection limit for Shamrock and Umboe are 86 and 58%, respectively. All the values below detection limit were removed before conducting any statistical analysis. Threshold values are chosen as 64, 55, 171, and 95 ppm As for the Alaska, Umboe, Mhangura and Shamrock areas, respectively (Table 3.11). As can be seen from the box plots on Figure 3.30 and summary statistics table below, hardly any anomalous concentrations of As are found in all four areas.

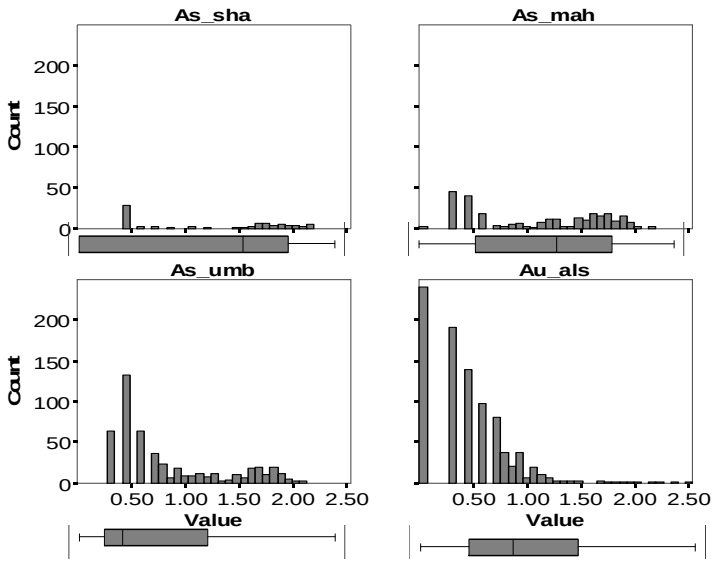

Figure 3-30 Frequency histogram and box-plot of As on log transformed data showing no outliers on extreme ends. als=Alaska, umb=Umboe, mha=Mahangura and sha=Shamrock

Table 3-11 Summary statistics of arsenic (As) computed using equation [B]

Area	Number of samples	Minimum value (ppm)	Maximum value (ppm)	Geometric mean (ppm)	lower quartiles Q1 (ppm)	upper quartiles Q3 (ppm)	threshold (ppm)
Alaska	302	2	102.0000	9.6	4	19	64
Umboe	500	2	125.000	7	3	16	55
Mhangura	274	2	151.000	12.3	3	45	171
Shamrock	79	2	151.000	17	3	76	295

Distribution of gold (Au)

Summary statistics of Au were computed after removing the censored values. About 20 % of the total samples in the Alaska, Umboe and Shamrock areas have Au values below detection limit. The Mhangura dataset contains 65% censored values. All the frequency histograms of Au are right skewed with large maximum values found on the high end (Figure 3.31). The threshold calculated for the Alaska, Umboe, Mhangura and Shamrock are: 17, 13, 15 and 19 ppb Au, respectively (Table 3.12). About 3% of the total samples in the Alaska and Umboe datasets are anomalous for Au. Only 11 samples in the Mhangura area contain Au values above the threshold. No samples in the Shamrock area contain Au value more than the threshold (Figure 3.33).

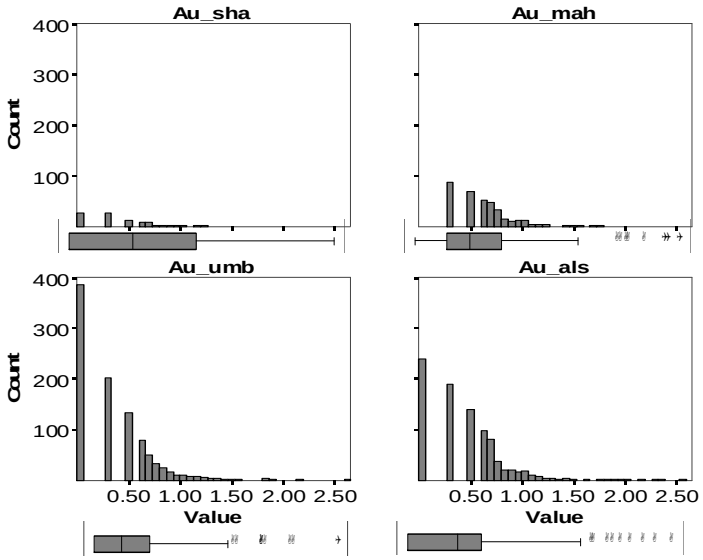

Figure 3-31 Frequency histogram and box-plot of Au.
als. =Alaska, umb=Umboe, mha=Mahangura and sha=Shamrock

Table 3-12 Summary statistics of gold (Au)

Area	Number of samples	Minimum value (ppb)	Maximum value (ppb)	Geometric mean (ppb)	lower quartiles Q1 (ppb)	upper quartiles Q3 (ppb)	threshold (ppb)
Alaska	908	1	346.0000	2.8	1	5	17
Umboe	988	1	450.000	2.2	1	4	14
Mhangura	360	1	59.000	4	3	6	15
Shamrock	92	1	18.000	2.3	1	5	19

The Au anomalies are found within arkose mostly associated with basic igneous rocks and doloritic dykes (Figure 3.33). In Umboe and Mhangura, the anomaly of gold is found along the contact with surrounding graphitic slate and slate of Piriwiri Group. The anomaly observed in granitic intrusions are found along stream bed, indicating possibilities of concentrations drained from top meta-sediments. No gold anomaly is found in Shamrock area with in gneissic rocks.

Distribution of silver (Ag)

Most of the Ag concentrations in all areas are below detection limit. About 93% of the samples in Shamrock have Ag values below detection limit. All three areas contain 76% of their samples below detection limit. Statistical analysis was done after removing these censored values. Extreme high Ag values in all datasets are concentrated at high end (Figure 3.32). From the statistical summary calculated for the datasets of Alaska and Umboe, only two samples contain Ag values above the threshold (Table 3.13). Seven samples of Mhangura have Ag values greater than the threshold. No sample in Shamrock contains Ag values above threshold (Figure 3.32). Almost all silver anomalies are found within the Deweras Group and has spatial association with copper (Figure 3.33).

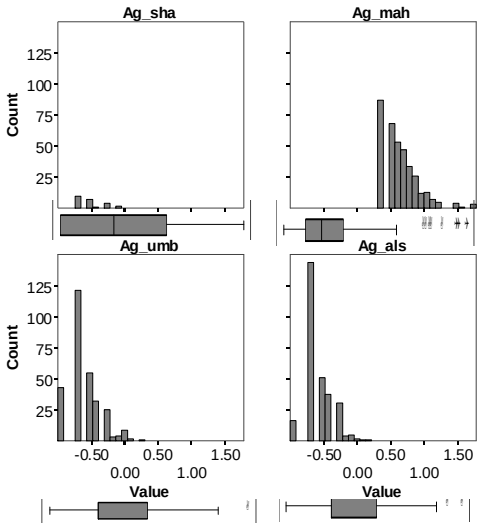

Figure 3-32 Frequency histogram and box-plot of Ag on log transformed data. Circles on box plot represent values above the threshold. Plus signs in Mhangura indicate very high anomalous values. als=Alaska, umb=Umboe, mha=Mahangura and sha=Shamrock

Table 3-13 Summary statistics of arsenic (Ag) calculated

Area	Number of samples	Minimum value (ppm)	Maximum value (ppm)	Geometric mean (ppm)	lower quartiles Q1 (ppm)	upper quartiles Q3 (ppm)	threshold (ppm)
Alaska	294	0.1	1.5000	0.2	0.2	0.4	1
Umboe	295	0.1	1.700	0.25	0.2	0.4	1
Mhangura	239	0.1	8.500	0.2	0.2	0.3	0.6
Shamrock	24	0.1	0.800	0.2	0.5	1.4	4

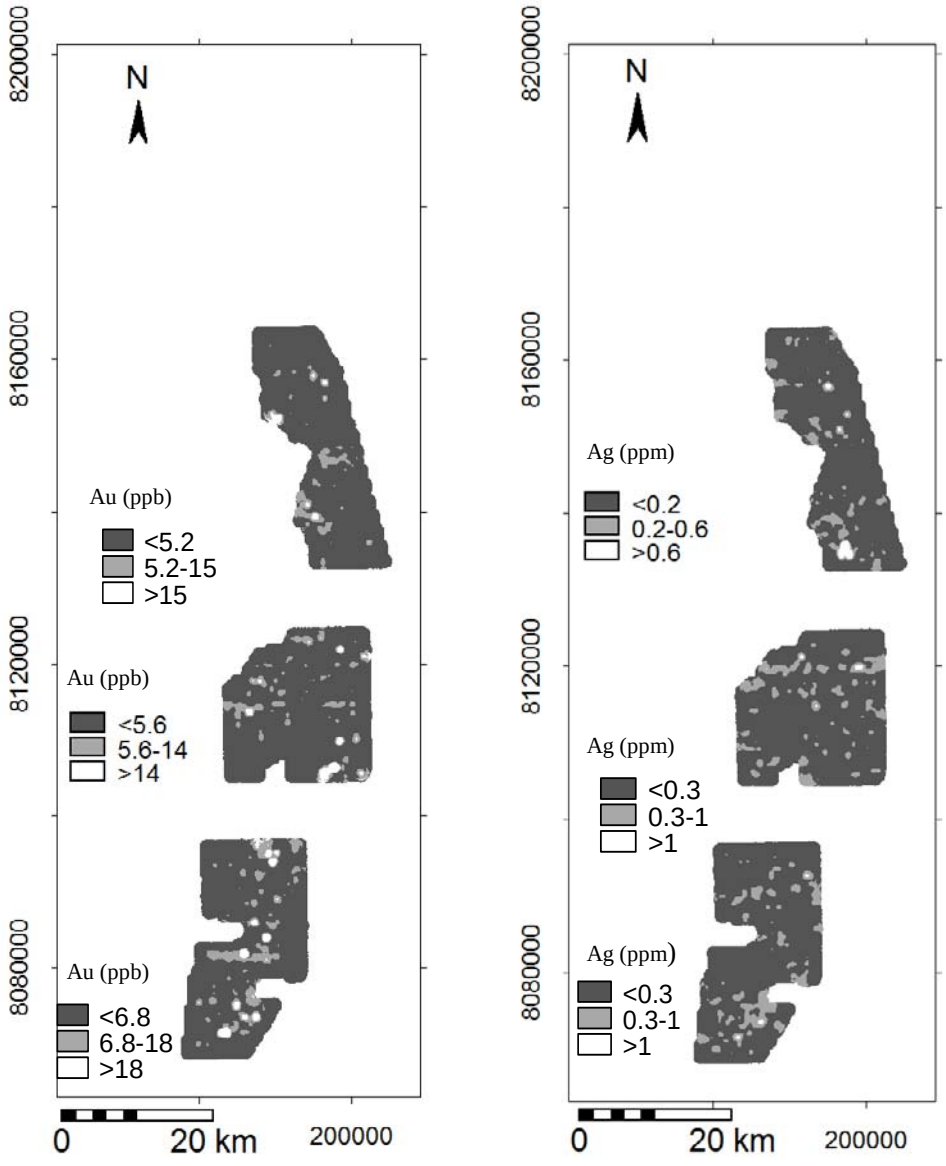

Figure 3-33 Geochemical anomaly map a) Gold (Au); and b) Silver (Ag) Magondi Belt, UTM Zone 36S projection, WGS 84.

3.3.7.2. Bivariate statistics

Investigation of bivariate relations between elements was carried out on scatter plots. The plot indicates spatial relations between the pair of elements. Scatter plots of Cu, Pb, Zn, Fe, Co and Ni in all areas indicate positive linear relations (Figure 3.34). Pb has very weak correlations with all elements in all areas. Fe and Co have a relatively strong positive correlation with other elements. Very weak positive relation of Cu with Pb and Ni exist. Copper has a relatively strong relation with Zn, Co, and Fe. In Mhangura and Umboe Cu has a relatively strong positive correlation with Zn (Figure

3.34). The relation between Co and Ni in all areas are very strong indicating close association of these elements.

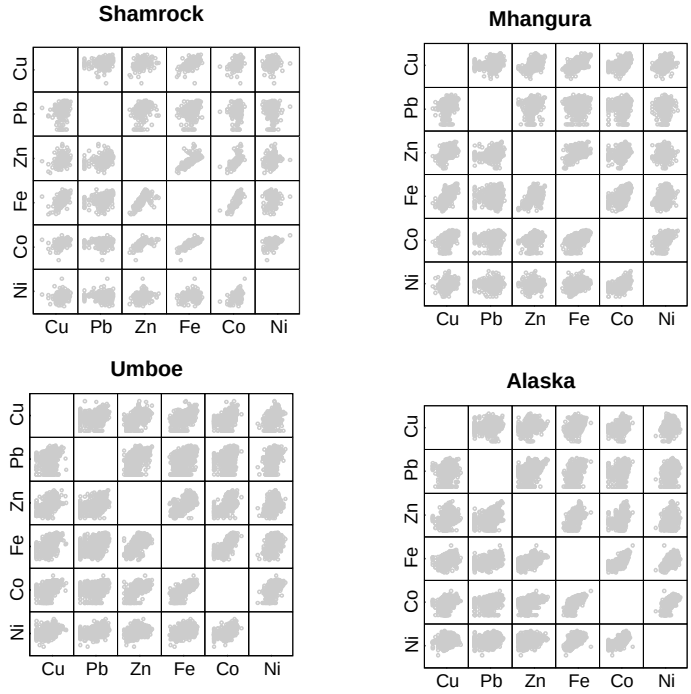

Figure 3-34 Scatter plots of elements of Shamrock, Mhangura, Umboe and Alaska areas

Pearson correlation coefficient analysis

Pearson correlation coefficient analysis is one method of assessing the element association in bivariate analysis. Pearson linear correlation coefficient calculated for each area is shown on Table 3.14. A coefficient significant at the 95% confidence level is assumed to indicate a meaningful correlation. Element correlation coefficients in the Mhangura, Umboe and Alaska areas are positive and significant at 95%. Correlation between Ni-Pb in Shamrock area is negative and the other pairs like Co-Pb, Ni-Cu and Ni-Zn are significantly positively correlated at 99% (Table 3.14). There is lack of correlation between Ni and Fe in the Shamrock area. All elements correlate positively with Cu indicating their respective concentration tends to vary together. Copper has a significant correlation with Fe, Co and Zn in all areas and is very strong in the Shamrock, Mhangura and Umboe areas. Fe has a very strong correlation with all elements except with Ni in Shamrock and Pb in Mhangura. The existence of correlation between Fe and these elements may suggest a scavenging effect of Fe (Table 3.14).

Table 3-14 Pearson linear correlation coefficient of Shamrock, Mhangura, Umboe and Alaska geochemical datasets. (*= 95% confidence level; **= 99% confidence level)

Shamrock

	Cu	Pb	Zn	Fe		Ni
Cu	1					
Pb	0.22(**)	1				
Zn	0.39(**)	0.27(**)	1			
Fe	0.58(**)	0.35(**)	0.67(**)	1	1	
Co	0.43(**)	0.13(*)	0.62(**)	0.81(**)	0.33(**)	
Ni	0.14(*)	-0.06	0.13(*)	0.05		1

Mhangura

	Cu	Pb	Zn	Fe	Co	Ni
Cu	1					
Pb	0.27(**)	1				
Zn	0.48(**)	0.24(**)	1			
Fe	0.70(**)	0.16(**)	0.55(**)	1		
Co	0.51(**)	0.21(**)	0.36(**)	0.57(**)	1	
Ni	0.28(**)	0.10(**)	0.20(**)	0.34(**)	0.45(**)	1

Umboe

	Cu	Pb	Zn	Fe	Co	Ni
Cu	1					
Pb	0.42(**)	1				
Zn	0.49(**)	0.42(**)	1			
Fe	0.66(**)	0.46(**)	0.63(**)	1		
Co	0.54(**)	0.40(**)	0.54(**)	0.78(**)	1	
Ni	0.34(**)	0.40(**)	0.35(**)	0.43(**)	0.54(**)	1

Alaska

	Cu	Pb	Zn	Fe	Co	Ni
Cu	1					
Pb	0.14(**)	1				
Zn	0.26(**)	0.35(**)	1			
Fe	0.29(**)	0.47(**)	0.63(**)	1		
Co	0.30(**)	0.32(**)	0.39(**)	0.65(**)	1	
Ni	0.14(*)	0.30(**)	0.32(**)	0.54(**)	0.59(**)	1

3.3.7.3. Multivariate

The method of multivariate analysis is to identify statistical relationships between variables. Analysis of inter element correlations was conducted to differentiate mineralization related element associations. Principal component analysis was conducted on six elements (Cu, Pb, Zn, Fe, Co and Ni). During the analysis log transformed data were used to make a Gaussian distribution. Elements like As, Ag and Au are not incorporated in the analysis, since both have more than half of their values below detection limit.

Principal component analysis

Principal component analysis (PCA) is one of the methods that can help reveal simpler patterns within a complex set of variables. In mineral exploration, the most common application of these multivariate analysis methods is to characterize and map inter-relationships within high volume surface geochemistry datasets. Components may reflect the geological and geochemical processes indicative of mineralization, lithology and alteration. The principal component analysis calculated for six elements in four areas are shown in Table 3.15. The percentage of variance of each six component and the loadings gives the ratio, expressed as a percentage of the variance accounted for by each component to the total variance in all of the variables represented.

Table 3-15 Principal component analysis of elements in Shamrock, Mhangura, Umboe and Alaska

Mhangura	PC1	PC2	PC3	PC4	PC5	PC6
Cu	0.82	0.11	-0.19	-0.29	0.32	-0.30
Pb	0.39	0.72	0.57	-0.01	0.03	0.08
Zn	0.70	0.25	-0.34	0.55	-0.16	-0.09
Fe	0.85	-0.06	-0.27	-0.13	0.11	0.41
Co	0.77	-0.23	0.18	-0.26	-0.50	-0.08
Ni	0.54	-0.56	0.50	0.30	0.22	-0.01
Variance%	48.72	16.08	13.99	9.23	7.40	4.58

Shamrock	PC1	PC2	PC3	PC4	PC5	PC6
Cu	0.69	-0.04	-0.05	0.71	0.12	0.05
Pb	0.4	-0.62	0.66	-0.07	-0.07	0.04
Zn	0.8	-0.04	-0.11	-0.32	0.49	0.01
Fe	0.92	-0.13	-0.17	-0.04	-0.22	-0.23
Co	0.86	0.26	-0.15	-0.2	-0.3	0.2
Ni	0.26	0.81	0.52	0.02	0.04	-0.07
Variance %	49.02	18.85	12.92	10.91	6.58	1.71

Alaska	PC1	PC2	PC3	PC4	PC5	PC6
Cu	0.43	0.86	-0.10	0.23	0.12	-0.02
Pb	0.60	-0.21	0.57	0.51	0.02	0.07
Zn	0.71	0.11	0.36	-0.54	0.15	0.19
Fe	0.88	-0.01	0.07	-0.15	-0.17	-0.40
Co	0.80	-0.06	-0.37	0.06	-0.39	0.23
Ni	0.71	-0.34	-0.45	0.09	0.42	-0.01
Variance %	49.76	15.15	13.45	10.74	6.60	4.29

Umboe	PC1	PC2	PC3	PC4	PC5	PC6
Cu	0.75	-0.30	0.07	0.49	0.29	0.05
Pb	0.66	0.26	0.68	0.01	-0.18	0.03
Zn	0.76	-0.27	0.01	-0.52	0.27	.059
Fe	0.88	-0.21	-0.14	-0.01	-0.24	-0.33
Co	0.85	0.01	-0.33	.017	-0.31	0.28
Ni	0.65	0.68	-0.24	0.00	0.24	-0.07
Variance %	58.23	12.24	11.02	8.50	6.77	3.23

The data variability in the individual areas accounted by PC1 is about 50%, representing the background population of the study area and reflects the combined effect of lithological, mineralogical and chemical controls. The high positive values on elements in this component probably represent scavenging of the elements by Fe (chemical control). The high loadings of Co and Ni probably indicate the presence of mafic-ultramafic rocks (lithological effect). Sulphide mineralization such as sphalerite (ZnS), chalcocite (Cu_2S) and galena (PbS) can also contribute to the high loadings of Zn, Cu and Pb (mineralization effect).

The PC2 of the Shamrock data has high positive loading (0.81) on Ni, moderately positive loadings on Co, but moderately low negative loadings on other elements. This component could be explained as background geology of mafic-ultamafic rocks represented by Ni-Co association. In the Mhangura dataset, PC2 has data variability of 16% containing high positive loading on Pb (0.72) associated with moderate positive loading on Zn and negative loadings on Ni and Co. This antipathetic relation probably indicates the occurrences of Pb and Zn anomaly due to Pb and Zn mineralization associated in mafic and ultramafic rocks. PC2 of the Umboe area contains high positive loadings on Ni, relatively moderate positive loading on Pb and negative loadings on Cu, Zn and Fe. This may indicate the existence of Ni anomaly due to mineralization (garnierite) or the presence of mafic-ultramafic rocks in the area. Data variability of 15.15% is accounted by PC2 on the Alaska dataset. Its significance could be interpreted as Cu mineralization in the study area. The high loading on Pb in PC3 of all four areas probably suggested the presence of Pb anomaly due to Pb mineralization (galena). In Shamrock and Mhangura, the PC3 has high loadings on both Pb and Ni probably indicating Pb and Ni anomaly represented by Pb and Ni mineralization (galena and garnerite). The antipathetic relation on Ni-Co and Pb-Zn on PC3 of Alaska suggest the presence of Pb and Zn anomaly in ultramafic rocks which is represented by Ni and Co association. The same relations also occur between Cu-Co and Zn-Ni in PC4 of Mhangura data probably representing anomalies of these elements in the area. The high positive loading on Cu in PC4 of the Shamrock and Umboe datasets suggest copper mineralization in the area. Relatively moderate positive loadings of Cu and negative

loadings on Co in PC5 of the Mhangura and Umboe datasets probably represent Cu mineralization in igneous sedimentary series (Beus and Grigorian, 1977).

Box plots of PC scores of high loadings on Cu were plotted as a first inspection of the spatial distribution of copper. Results indicate that PC scores in all areas show outliers of large values in the high end corresponding to anomaly concentration (Figure 3.35). The PC scores of each area then compared with copper, zinc, gold and silver anomaly maps of Figure 3.23 and 3.33 to identify areas of overlap which are expected to represent copper mineralization in the study area. In Alaska high concentrations of copper anomalies occur around the Hans and Angwa Mine in the south. To the north low Cu concentrations are found north of Shaklton and north-west of Avondale Mine. Copper anomalies in Umboe are located west and north of the United Kingdom Mine to the east, and south west of Norah Mine, in the north and west of the area. In Shamrock, concentrations of Cu are found around the Shamrock Mine.

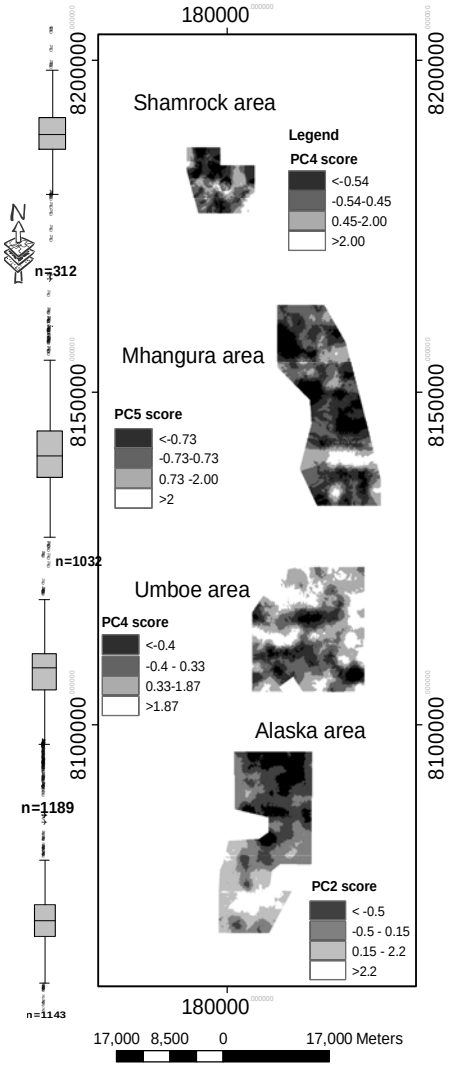

Figure 3-35 Showing PC scores and accompanying box plots indicating anomalous concentration of copper in Alaska, Umboe, Mhangura and Shamrock areas. Box plots show outliers in the high end corresponding to anomalous values of Cu. (n=number of geochemical soil samples in the area).

Geochemical interpretations

The spatial distributions of elements indicate that, most of the anomalies were found within the arkoses of the Deweras Group. Some anomalies were also found along the surrounding boundaries of arkoses with granite, slate and phyllite. The univariate analysis revealed that out of nine elements, six elements, (Cu, Zn, Ni, Co, Au and Ag) show anomalous values in most of the datasets. Only Alaska has anomaly of Fe. No anomaly of Co is encountered in Mhangura. The Absence of Au and Ag anomalies in Shamrock area suggest no mineralization of these elements in gneissic rocks. Zn, Ni, Au and Ag have a spatial relation with Cu indicating their close association. Copper has remarkable strong positive relation with Zn, Co and Fe and weak relation with Ni and Pb. The positive linear relations of copper in both areas might indicate same origin and type of mineralization hosted in particular types of rocks, in this case arkose and basic igneous rocks of the Deweras Group.

The first component in the principal component analysis contains high loadings on all elements. The relatively high loading of elements with Fe in this component probably indicates the possible scavenging of elements with coprecipitation with iron hydroxide. High loadings of Ni and positive loading on Co in PC2 of Shamrock could be due to the presence of mafic-ultamafic rocks represented by Ni-Co association. Antipathetic relation between Pb-Zn and Ni-Co, in Mhangura and Ni-Pb and Cu-Zn in Umboe, also corresponds to same rock containing Pb-Zn and Cu mineralization (Table 3.15). PC2 can therefore be used as one of the component to map ultramafic rocks of the study area. The score of this component overlaps most of the basic igneous rocks and shows western extension of meta-ultramafic rocks in Mhangura area. In Umboe, high PC2 scores coincide with anomalous concentration of Ni. PC2 of the Alaska data, PC4 of the Umboe and Shamrock datasets and PC5 of the Mhangura have high loadings on Cu probably representing the mineralization in the area. The plots of scores of the components representing Cu anomalies show areas on Cu mineralization. These components were overlapped with the copper anomaly map of Figure 3.23. The resulting map was overlaid with the Au and Ag anomaly maps of Figure 3.33 to determine potential areas for mineralization (Figure 3.36).

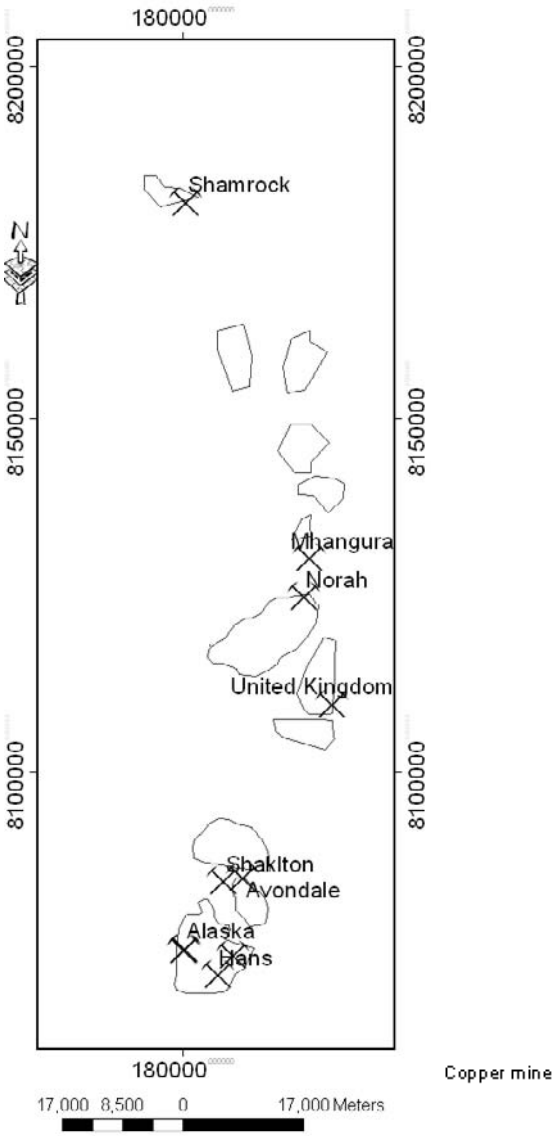

Figure 3-36 Copper anomaly map of Magondi Belt. Polygons represent copper anomaly zone.

4. Data integration for Geological mapping

Image enhancement and transformations enabled visual interpretations to be carried that allowed the identification of lithological and structural features in the previous chapter. Integrating of individual images data further provided additional information to lthological interpretation. Various integration techniques were employed to improve the visual appearance of multi-spectral data. To acquire more information and integrate different data, images were variously fused (van Genderen and Pohl, 1994; Schetselaar, 2006). Image integration techniques involved fusion of multi-spectral bands with high spatial resolution data like panchromatic image (Schetselaar, 2006) Lithological contrast can often be reflected in topography. Multi-spectral images fused with SRTM data could easily enhance the lithological contact along the topographic difference (van Genderen and Pohl, 1994). Merging color composite images with DEM results in a number of image features, which have reflectance and topographic signals in image data. In geology, DEM is used to visualize the geomorphologic characteristic of the terrain in relation with underlying geology (van der Meer, 2006). 3D visualization and geospatial analysis (Jones *et al.*, 2006) and Intensity-Hue-Saturation (IHS) transform are also used to combine a large number of geospatial data into a single model (Schetselaar, 1998).

4.1. Combining images with digital elevation model (DEM)

The best band combination of multi-spectral Landsat TM and ASTER, which were interpreted in the previous chapter are now fused with SRTM and ASTER DEM to further enhance and improve the lithological interpretation. Images were first normalized and color composite images of 4 5 3 and 7 4 2 (RGB) of Landsat TM and ASTER, respectively, were integrated with shaded relief images. As a result of combined spectral and terrain features, the lithological and structural features were well discriminated (Figure 4.1). The lithological contacts were clearly deciphered because of their topographic differences. Contacts were enhanced by sharp color boundaries. With the exception of the central part, which cover and occupies low topography, most of the units were clearly identified. In both fused images, gneiss and granite in the north, phyllite and slate in the west and dolomite in the east show rough textures. Phyllite, graphitic phyllite, slate, granite and gneiss were well discriminated on ASTER image (Figure 4-1a and b). In this area, strong foliation trends, folds and NE trending lineaments are interpreted. The lineaments, possibly faults, are interpreted on gneiss, phyllite, dolomite and quartzite. To the southwest, the rocks exhibit prominent tight folding structures. This rock unit was mapped as undifferentiated phyllite, slate and quartzite. The unique geomorphologic features help differentiate this rock from the surrounding slate. According to the field observation datasets (Appendix B), this lithology was mapped as feldspar-bearing quartzite. A relatively smooth, low topography and variegated pixels corresponds to soil covered agricultural land in the central part of the area.

4.2. Combining with high resolution image

The PCA analysis of Landsat TM conducted on previous chapter identifies lithologic features. Here, in order to increase the spatial resolution of Landsat TM image the bands were resampled to the pixel size of high resolution panchromatic image of Landsat band 8. Principal component analysis (PCA) and intensity hue saturation (IHS) images can be used to merge Landsat spectral images to high resolution panchromatic image (Rigol and Chica-Olmo, 1998; Owusu *et al.*, 2006; Schetselaar, 2006). Adding band 8 to PCA enhanced the resolution of the PC image and further increases the interpretability (Figure 4.1c). The resulting image shows a clear structural features and lithologic contacts.

To the southwest, a folded rock unit, which was not seen on enhanced images in the previous chapter, is now clearly discriminated (Figure 4.3). This rock unit is classified as feldspar bearing quartzite based on literature review and field observation dataset (Appendix B).

4.3. Intensity-Hue-Saturation (IHS) transformation and fusion

IHS images are well perceived by human eyes than RGB, since blue color is less sensitive to the human eyes than red and green (van Roij, 2006). IHS color composite often adds more color to an image and helps to discriminate lithological features.

Three steps are followed in IHS fusion and transformation in order to further enhance the color composite image (Schetselaar, 1998). The first step is transforming the three bands to IHS. This is followed by replacing the intensity component with the original band-image and finally transforms the H; S using inverse IHS transforms which brings back the image to RGB. Color composite image of Landsat TM 5 4 3 (RGB) was used for IHS transformation. The first band was replaced by high resolution panchromatic image, band 8. The resulting image was enhanced and shows clear lithological contacts and structural features. The western part of the area which was mapped as undifferentiated quartzite, phyllite, graphitic slate and slate are now differentiated (Figure 4.1d). The dark bluish pixel was one of the identified units. This rock unit according to field observation datasets is described as feldspar bearing quartzite (Appendix B). Slate, graphitic slate and dolomite could also be identified in the image.

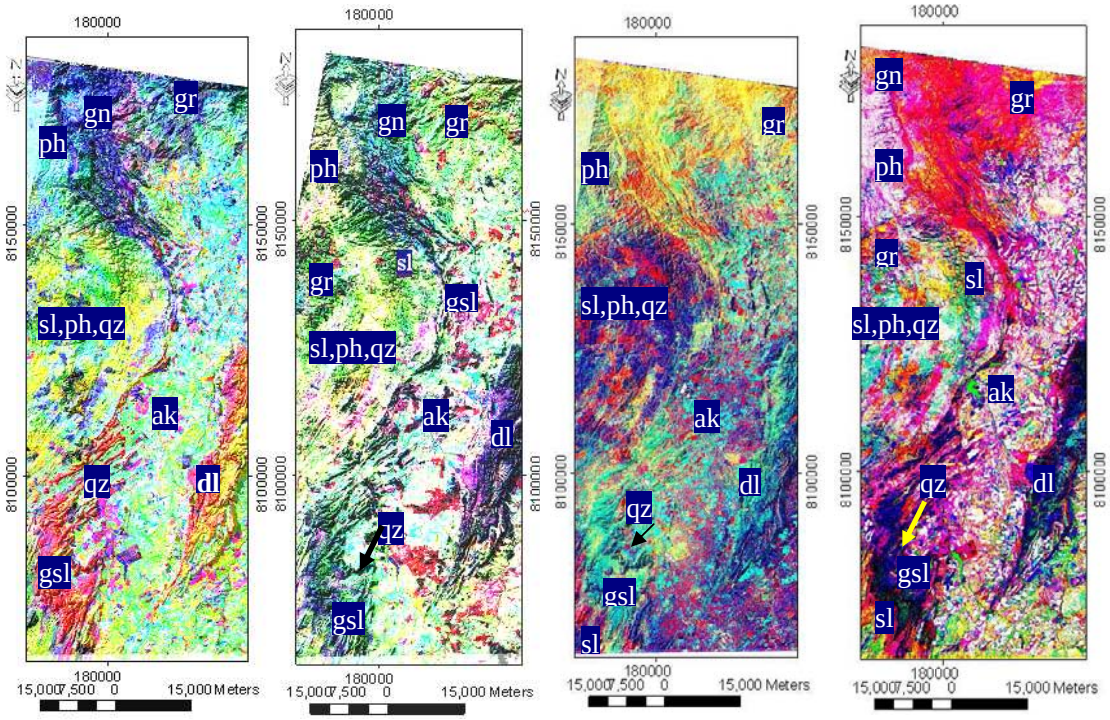

Figure 4-1 Integrated color composite normalized multispectral images a) DEM fused with Landsat TM 4, 5, 3 RGB b) DEM fused with ASTER 7, 4, 2 RGB; c) PC image 2, 3, 4 RGB fused with Landsat TM, high resolution panchromatic image d) Landsat TM 4, 5, 3 RGB transformed to IHS and fused with high resolution panchromatic image (band 8); (qz= quartzite, dl= dolomite, sl = slate, ph = phyllite, gsl = graphitic slate, gr = granite, gn = gneiss).

4.4. Compilation of interpreted images and lithological boundaries

As part of integration exercise compilations of the various interpreted images with existing geological data were done to update the geological map of the study area. Lithological boundaries recognized from image interpretations were supported by available geological maps and field observation datasets (Appendix B). In areas where extensive soil cover occurs, interpretations obtained from high resolution aeromagnetic data supported the extraction of additional information in the southern portion of the area. The nomenclatures of rock units (on compiled geologic map) were adopted from the geological maps and datasets available on previous work (Surveyor-General, 1985; Carballo Lopez, 1998; Kambewa, 1998). Segment layers extracted from all datasets were overlapped and lithological and lineament boundaries were digitized to produce on updated geological map of the study area.

Lithologic units, which were identified by their specific spectral, topographic and magnetic signal, were discussed and compared with the old geological map (Table 4.1).

4.4.1. Biotite and hornblend para gneiss (gn)

This rock unit was mapped as Precambrian gneiss of various age and origin in the existing published geological map (Surveyor-General, 1985). On the various images used and interpreted, the unit was recognized by its rough texture, parallel drainage pattern, relatively vegetated and occupying high topography (Table 4.1). The boundary with phyllite is clearly identified throughout the interpreted images. Interpretation of its contact with basic igneous rock is possible only in the fused images. PC and band ratio images of Landsat TM bands 3/1 (iron oxide) and 5/7 (clay) show strong reflectance on weathered surfaces due to iron bearing and kaolonized minerals (biotite and feldspar).

4.4.2. Meta-ultramafic rock (ul)

Meta ultramafic rocks reported as talc and serpentine-bearing are mapped in the eastern parts of the area on the published geological map of Zimbabwe (Surveyor-General, 1985). Although not visible in any of the interpreted images, the soil geochemistry revealed the presence of ultramafic rocks interpreted by Co and Ni association in PC2 (Table 3.15).

4.4.3. Granite (gr)

Rocks of granitic intrusions occupy the northwestern, south-eastern and north-eastern parts of the study area. Except in the south-east, which is mostly covered by soil, in most of the interpreted images, the rocks exhibit rough texture, dendritic to sub-parallel drainage pattern, scarce vegetation and occupy high terrain. PC and ratio images of 3/1 (iron) and 5/7 (clay) enhance the rock unit (Figure 3.7 and Figure 3.11). Strong reflectance in spectral region on band 5 and band 4 and major absorption on band 7 and 6 of Landsat TM and ASTER, respectively, indicate the rock is highly kaolinized (Table 4.1). The south-eastern granite was mapped partly as metasediment and metavolcanics, slates, quartzite and dolomite (Figure 3.3). Although this unit is difficult to discriminate due to soil cover, the field observation datasets show that the unit is entirely covered by granite (Appendix B).

4.4.4. Doloritic dykes (dk)

This unit was mapped as intrusive igneous rocks as dolorite and gabbro in the northern parts of the study area (Figure 3.3). It was also reported to occur within the Deweras Group associated with basic igneous rocks and arkose in the central part of the study area (Carballo Lopez, 1998). The unit was also interpreted from analytical signal of total field magnetics (Figure 3.18).

4.4.5. Basic igneous rocks (ig)

Basic igneous rocks, like the doloritic dykes above, were interpreted from total field magnetic data. (Figure 3.17 and 3.18) (Telford *et al.*, 1990). Interpretation of this unit on multispectral Landsat TM

and ASTER images is possible in areas where there exist exposures. Discontinuous, NE trending, some times folded and linear like features are seen in the central part (Figure 4.1c). The color composite images of ASTER and fused images also enhanced the rock unit in the northern part of the area (Figure 3.10a, and 4.1a). Here, the unit occupies high topography, rough texture and has sub-parallel drainage pattern (Table 4.1).

4.4.6. Arkose (ak)

This unit occupies the central part of the study area where extensive agricultural activities takes place. The unit was mapped as metasediment and metavolcanics (Figure 3.3) (Surveyor-General, 1985). Due to thick soil cover, the interpretation in the southern area is only possible by using high resolution aeromagnetic data. The analytical signal of total field magnetics reveal an intermediate magnetic signal of the rock unit (Telford *et al.*, 1990) (Figure 3.17b and 3.18). In the north central part, the unit is well discriminated from all interpreted images.

4.4.7. Dolomite (dl)

The unit was mapped as slate, quartzite and dolomite (Figure 3.3) in the published geological map. Except in the south central part, dolomite was well discriminated in all interpreted images. It shows low reflectance in all bands except band 4 in Landsat TM and equivalent band 3 of ASTER. It has rough texture, folded and faulted and occupies a relatively high topography (Figure 4.1 and 4.2). Clear contact with the surrounding lithology is enhanced by sharp color boundaries. Interpretations of analytical signal total field magnetics also confirms the occurrence of dolomite associated with arkoses and basic igneous rocks (Figure 3.17b and 3.18). Its low magnetic signal (Telford *et al.*, 1990) makes it possible to discriminate from the other units. Image classification conducted on both Landsat TM and ASTER image was well identified the unit (Figure 3.14).

4.4.8. Phyllite (ph)

This unit was mapped as part of undifferentiated slate, quartzite and phyllite (Figure 3.3) (Surveyor-General, 1985). Its significant difference in topography and increased reflectance makes this unit different from the undifferentiated rocks (Figure 4.1 and 4.2). It occupies the northwestern parts of the area and is clearly discriminated in all interpreted and classified images. It has relatively smooth/fine texture, characterized by parallel to sub-parallel drainage patterns and occupy high topography (Figure 4.1 and 4.2).

4.4.9. Graphytic slate (gsl)

This unit is also mapped as part of undifferentiated rocks. Its relatively strong reflectance in spectral region on Landsat TM band 3 and band ratio of 3/1 distinguishes the unit from the other

undifferentiated rocks (Table 4.1). This spectral characteristic of the rock indicates the composition of iron oxide due to alteration or weathering of iron bearing minerals such as biotite. Rough texture, significant relief and strongly developed foliation, folds and faults make it distinct from other rocks (Figure 4.1a-d). According to previous works and the existing published map, this unit is associated with dolomite and quartzite (Stagman, 1978; Surveyor-General, 1985). It has similar spectral signature with dolomite in the southeastern part, suggesting that the unit consists of dolomite and quartzite (Stagman, 1978; Surveyor-General, 1985) (Figure 4.2). Classification of ASTER image discriminate the unit from dolomite (Figure 3.14).

4.4.10. Slate, phyllite and quartzite (sl, ph, qz)

This undifferentiated unit occurs in the western part of the area. In all interpreted images, the unit is represented by variegated pixels, rough texture, contain strongly developed foliation and occupies a relatively high topography (Figure 4.1 and 4.2). Due to similar relief, texture and mixed spectral signature, it is difficult to distinguish between the rocks in this unit (Figure 3.14).

4.4.11. Feldspar bearing Quartzite (qz)

This rock unit, like the other Piriwiri Group rocks, was mapped as undifferentiated slate, phyllite and quartzite. The boundaries of this can be delineated on the DEM. The fused images suggest that unit is tightly folded (Figure 4.1a-d). Its low reflectance in all bands, rough texture, significant relief and folding structure allow this unit to be distinguished from the other rock unit.

4.5. Geological structures interpreted from integrated images

Lineaments interpreted from the DEM are further supported by features extracted from the fused images. A general NE trend of lineaments in the south, which turn to the NW, corresponds with folded like structural features. This feature is clearly seen on graphitic phyllite, arkose and basic igneous rocks (Figure 4.2). To the north, the rock units are highly fractured indicating NE and NW trending regional lineaments, probably faults. Strong foliations, faults and folded structures are clearly seen on quartzite, graphitic slate and dolomites (Figure 4.2). Here, tight, asymmetric folds with axial plane trending NE-SW were interpreted. Similar folded structure in Piriwiri Group rocks with axial plain trending NS and NNE were reported in the study area (Stagman, 1978).

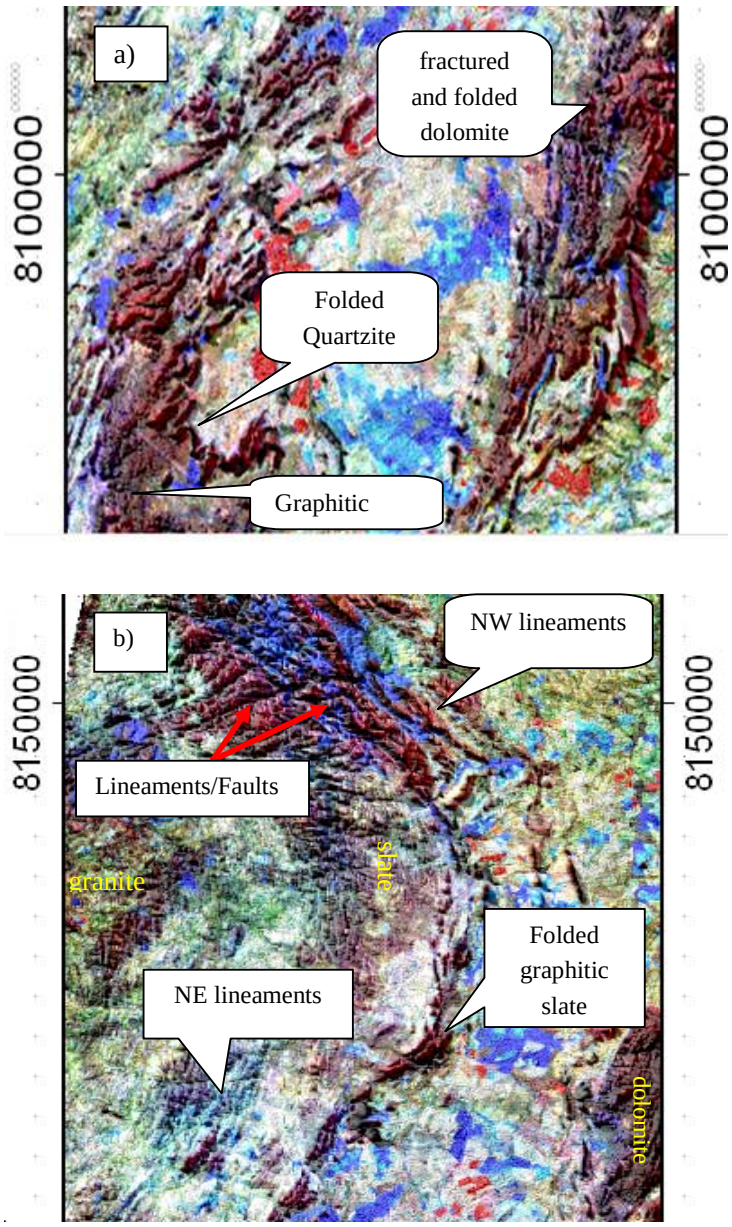

Figure 4-2 Color composite 3 6 11 RGB ASTER, fused with DEM showing interpreted structural features; a) tightly folded quartzite and dolomite; b) NE and NW trending foliations faults and folds.

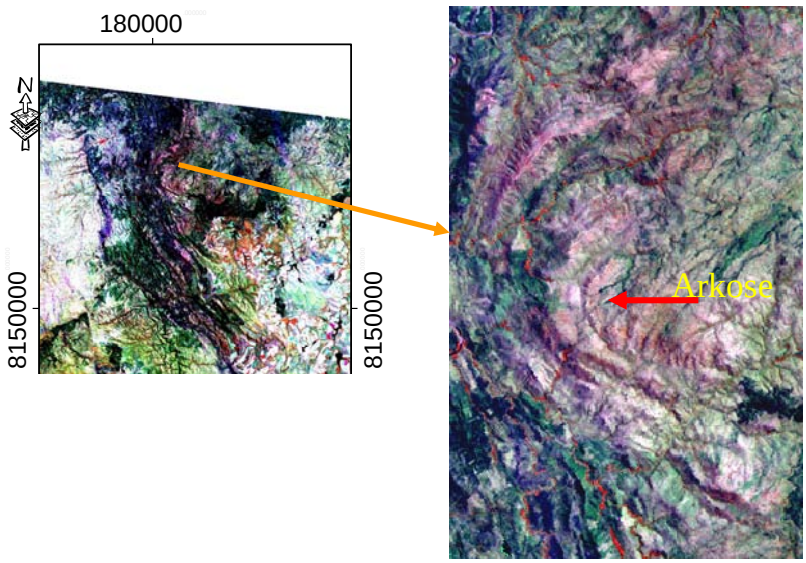

Figure 4-3 Color composite 453 RGB indicating interpreted folded igneous rocks and arkose in the northern parts of the area.

4.6. Updated geological map

Integration of geological information derived from RS, geophysical and geochemical datasets within GIS is possible (Arnold Ivan Johnson, 1992). GIS provided the opportunity to integrate and compare data having different formate and scale. The various enhanced and interpreted images were ovarlaid and the extracted segment boundaries and lineaments were digitized. Interpreted images representing windows of various enhanced and fused datasets are shown on Figure 4.4. The interpretation results of fused and multispectral images, DEM and total field magnetics were combined with the results of enhanced images to produce the updated geological map (Figure 4.5). The characteristic feature of each lithologic unit with respect to spectral, vegetation cover, geologic structure, landform and magnetic signal are summarized in Table 4.1. The lithological units in the pubished geological map are listed together with the description of features for comparision.

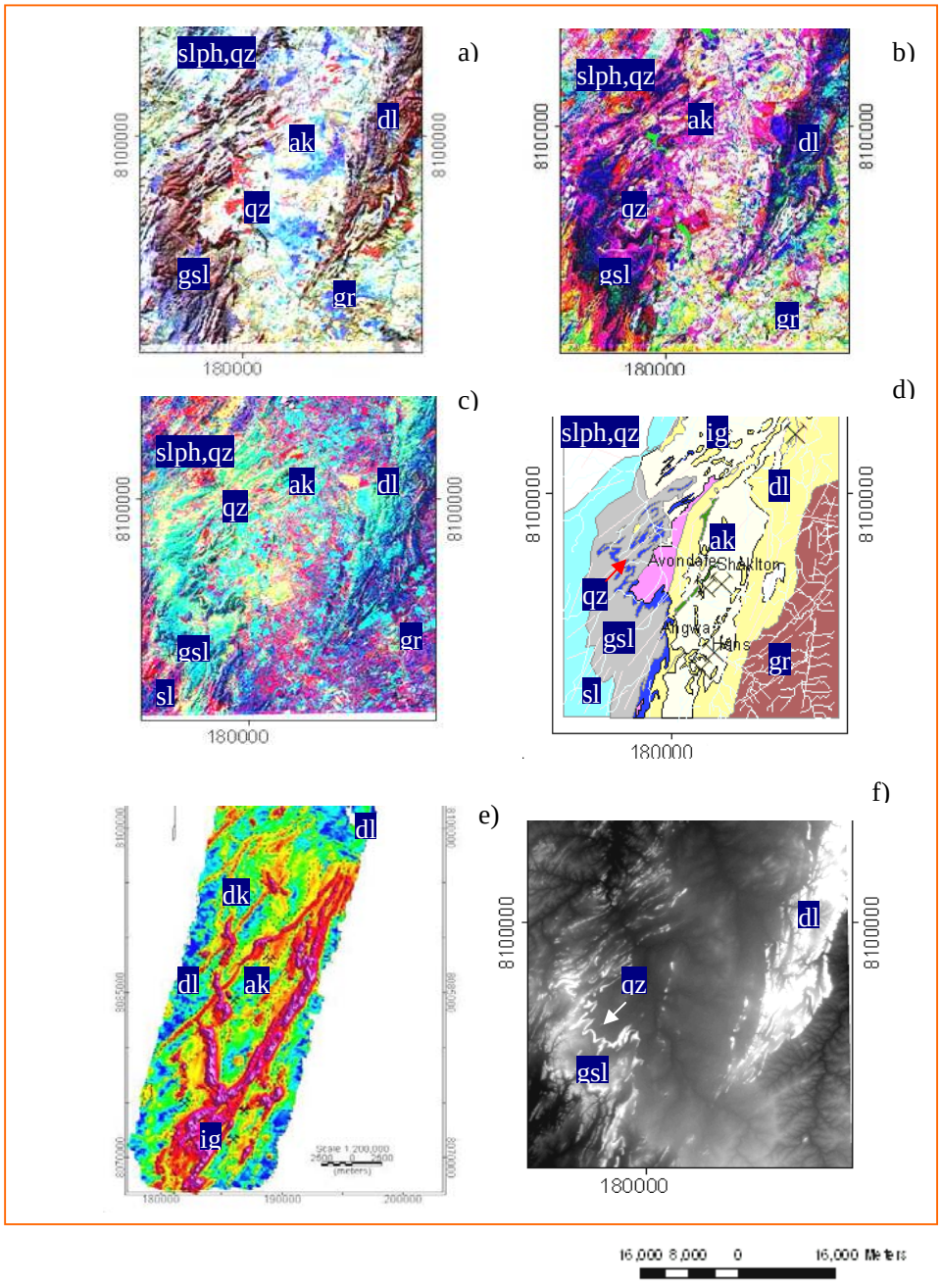

Figure 4-4 Interpreted images showing windows of southern portion of the study area a) Landsat 453 RGB fused with DEM b) IHS image fused with high resolution panchromatic image c) PC bands 12 3 (RGB) fused with high resolution panchromatic image d) interpreted geology e) analytical signal of total magnetic field;; f) SRTM DEM. (ig = basic igneous rocks ak = arkose, ph = phylite, gsl = graphitic slate, sl = slate, gr = granite; qz = quartzite)

Table 4-1 Interpreted lithology and their characteristic features

Rock type	vegitation	Drainage	Land form	Spectral characteristics	Magnetic signiture	structure	Old geological map
Slate	Sparse	Sup-parallel	Moderate slop to flat	Major absorption in 2.17-2.21 µm (bands 5 and 6)	low	Strongly developed foliation	Mapped as phylite, slate and quartzite
Quartzite, (feldspathic quartzite)	Sparse	Parallel and dendritic	Moderate slop	Absorption in 2.17-2.21 µm	-	no	Mapped as one unit /metasediments and metavolcanics
Graphitic slate	no	Parallel and sub-parallel	Moderate slop	Reflectance in TM band 3 and ratio 3/1(0.6-0.8 µm)	-	Strongly developed foliation, folds and faults	"
Phyllite slate and quartzite	Sparse	Sub-parallel	Moderate slop to flat	Major absorption in 2.17-2.21 ; 0.85-0.92 µm /band 4µm/clay	-	Strongly developed foliation	"
Phyllite	-	Parallel - Sub_parallel	Moderate slop	Strong reflectance in all bands		no	Mapped as one unit /metasediments and metavolcanics
Dolomite	Sparse	Dendritic, parallel and Sub-parallel	High relief moderate slope	Reflectance on ratio 5/7 major absorptions 2.30-2.40 µm (bands 8 and 9 /Mg-OH	low	Strongly developed foliation, fold and faults	Mapped as metasediments/slate, quartzite and dolomite
arkose	Sparse	Dendritic and Sub-parallel	flat	Major absorption in 2.17-2.21 /clay; 0.85-0.92 µm /band 4µm/	moderate	Strongly developed foliation/southern part soil cover	Mapped as Metasediments and metavolcanics
Basici gneous rocks	Moderate to sparse	Dendritic and Sub-parallel	Steep to moderate and flat (south)	Absorption in 0.85-0.92 µm /band 4 (Fe3+)	high	Strongly developed foliation, folds and faults	"
Doloritic dyke	Sparse	-	moderate	Absorption in 0.85-0.92 µm /band 4 (Fe3+)	Very high	no	Intrusive igneous rocks
Granite	no	Paralle-subparallel		Absorption in 0.85-0.92 µm / and Strong reflectance band 5 and ratio 5/7 (2.17-2.21 µm) clay	-	faults	granite
Biotite and hornblend para-gneiss	Dense-moderate	Dendritic and Sub-parallel	Steep to moderate slop	Major absorption in 2.17-2.21 /clay; 0.85-0.92 µm/Fe+3 /band 4µm/clay	-	-	Gneiss of various ages

4.7. Validation of updated geological map

The updated geological map of the study area was validated with the field observation datasets, which consists of 135 locations of geological sample points and observations (Appendix B). Most areas covered by gneiss and all areas of grits are not included within the multispectral images. These lithological units were adapted from the old geological map (Surveyor-General, 1985) and were not included in the validation.

The map was crossed with the raster map created for the observation points to determine the percentage of correctly interpreted lithologies with respect to the ground truth obtained from the observation point. A confusion matrix made for the updated geological map versus the field observation data indicates rock units such as dolomite, quartzite and undifferentiated rock unit (phyllite, quartzite and slate), have the highest classification accuracy (Table 4.2). This is because only four observation points of undifferentiated rock unit were obtained for validation. The high value of dolomite and quartzite are due to the fact that these units were well interpreted in the multispectral images. The low values are indicated on rocks of the Piriwiri Group and doloritic dykes. The rocks of Piriwiri Group were mapped as undifferentiated slate, graphitic slate, phyllite and quartzite. These rocks have similar spectral and topographic signal and are difficult to discriminate. There were also difficulties in differentiating doloritic dykes from basic igneous rocks because of similarities in magnetic signal. All the above mentioned factors probably influence the overall accuracy of the results which was calculated to be 76% (Table 4.2).

4.8. Comparison with the old geological map

The updated geological map was also crossed with old geological map to indicate the propertion of improved lithologies with respect to the older one (Table 4.3). About 90% of the alluvium (al) in old geological map were reclassified into arkose (ak), dolomite (dl), basic igneous rocks (ig), and phyllite (ph) in the new and updated geological map (Table 4.3 and Figure 4.5). The undifferentiated units, phyllite slate and quartzite (ph,sl,qz), which were mappped as one unit, were also subdivided into slate (21%) and phyllite (15%). About 18% of dolomite in the old geological map was reclassified as graphitic slate (gsl), quartzite (qz) and arkose (ak). The arkose unit in the old geological map was subdivided into phyllite (14%), dolomite (13%), basic igneous rocks (8%), and granite (25%). Only 13% and 4% of gneiss in the old geological map were subdivided into arkose and basic igneous rocks respectively.

Table 4-2 Confusion matrix results for updated geological map versus ground Control/field observation data

Updated lithology	**Field observation data**											
	slate	Slate quartzite and dolomite	quartzite	Graphitic slate	Phyllite, slate and quartzite	phyllite	Dolomite	arkose	Basic igneous rocks	Doloritic dyke	granite	Total
slate	400			199								599
Slate quartzite and dolomite		100									1000	1100
quartzite			374	29								403
Graphitic slate				200								200
Phyllite, slate and quartzite					400							400
phyllite						400						400
Dolomite							2441	32				2473
arkose	300	100		271		100		3703	678	105		5257
Basic igneous rocks								98	506	16		620
Doloritic dyke										95		95
granite						100		201	100		2103	2504
Total	700	200	374	699	400	600	2441	4034	1284	216	3103	14051
Classification accuracy %	57	50	100	28.6	100	66	100	91	39	44	67	76

Table 4-3 Cross table for old geological map and updated geological map of Magondi Belt (ig = basic igneous rocks, ak = arkose, ph = phylite, gsl = graphitic slate, sl = slate, gr = granite, qz = quartzite, sst grits and sandstone, al=alluvium)

Updated	old lithological map									
lithology	al	sst	sl,qz,dl	ph,sl,qz	dl	ak	dk	gr	gn	Total
al	4969									4969
sst		8496								8496
sl				226714		13114	7781	1289	99	248997
sl,qz,dl			22660							22660
qz				6	25802	743				26312
gsl				11016	127584	504				139104
ph,sl,qz				551334						551334
ph	4743			159563	385	60904	473	9838	1327	236883
dl	6681				1120138	56132		797	2	1183750
ak	39380			17086	122919	147618	5468	44674	255	377400
ig	4240	66			21513	34934	76	15908		
dk						4306				
gr		20		40162	71829	105925	21876	275997	5004	515809
gn	228			66566	461			94		67121
Total	60241	8582	22660	1072447	1490170	424180	35674	348597	6687	

4.9. Summary of geological integration

The capability to interpret and integrate diverse geological datasets in updating the geological map was tested in the Magondi Belt, the research area. Accordingly, the geological map is updated based on the interpretation and integration of digital multispectral remote sensing images and high resolution aeromagnetic datasets. Color composite, band ratio and PC images of Landsat TM and ASTER, identified lithological features on exposed terrain. Nomenclature of interpreted rock units are adapted from the existing geological map and field observation datasets (Appendix B). The ground truth information datasets were overlaid on interpreted images to give the correct name and outline the lithological boundary. Major lithological units such as dolomite, gneiss, graphitic slate, and phyllite are easily discriminated on all enhanced images.

Integration of multispectral images with DEM combine spectral as well as terrain signals of features, resulting additional information for the interpretation of lithology and lineaments. The granitic intrusions, gneissic and basic igneous rocks of the northern area are enhanced and clearly identified as a result of integration spectral data with DEM. Visualization of 3D image also helped to show the geomorphologic characteristic of the terrain in relation with the underlying geology. Here, topographic difference together with spectral signatures of the rocks helped in identifying the rock units in the western and eastern parts of the area. Phyllite, granite, gneiss, and graphitic slate in the west, and dolomite and granite in the east are well identified by their topographic relief.

IHS and PC color composites add more color to an image. Integration of these color composites with the high resolution panchromatic

Landsat image provide additional information for the lithological interpretation. The lithological units, which were mapped as undifferentiated slate, quartzite, and phyllite are now differentiated by the help of combined IHS and high resolution panchromatic image of Landsat TM (band 8). Relatively low topography and brown pixels and rough texture on both fused images discriminate slate from the undifferentiated rocks. Graphitic slate shows high absorption in all bands except in Landsat TM band 3 and ASTER band 4. Landsat TM band ratio image 3/1 also discriminate the rock unit. PC color composite images 2 3 4 (RGB) of Figure 4-3 fused with the high resolution panchromatic image also enhanced the folded rock unit, quartzite in the southwestern parts of the area. This unit, like phyllite, slate and graphitic slate were mapped as one undifferentiated unit in the old geological map. Discrimination of this unit is only possible with the help of integrated and fused images (Figure 4.1, 4.3 and 4.4).

All segments interpreted from the various images and ground truth geological datasets were digitized, overlaid and integrated in GIS to produce the updated geological map (Figure 4.5).

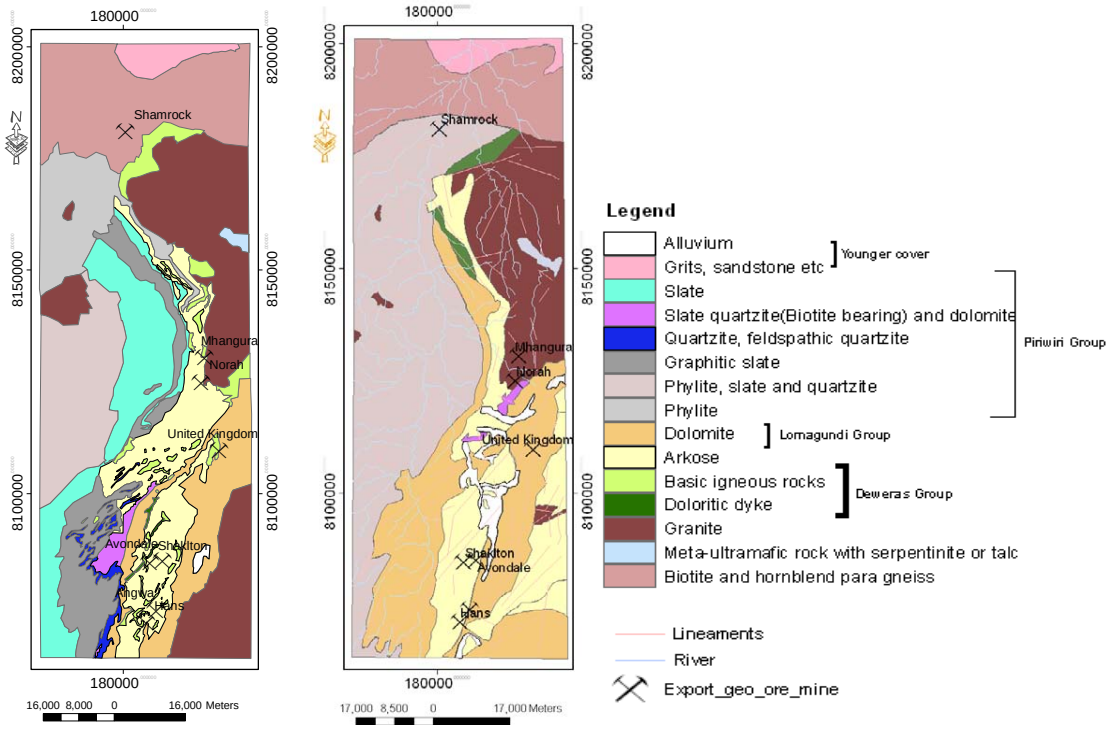

Figure 4-5 Geological maps of Magondi BeltCompiled updated geological map of the research area. (UTM Zone 36S projection WGS 84 Datum).

5. Spatial data integration for predictive modeling of mineral potential

Mineral exploration involves consecutive stage of activities starting from small scale to large scale, eventually leading to the selection of potential areas for identification of ore deposits (Bonham-Carter, 1994). Based on evidence like, geological, geochemical geophysical and locations of known mineral occurrences, favourable areas are selected for future exploration. The conventional methods of selection, evaluation and combination of evidences by physically superimposing maps to determine the overlap relationship are now greatly improved by using various GIS models. Evidential Belief Functions (EBFs) is one of the methods for spatial analysis and integration of various geological datasets. This method is applied to integrate geological datasets of the research area to produce a mineral potential map. The EBFs for mineral potential mapping demonstrated by Carranza and Hale (2003) is used here to predict mineral potential of the study area. This method is applied to areas, like Magondi Belt, where there are known mineral deposits but the number of deposits may be inadequate to generate statistically significant result by using statistical data-driven methods like weight of evidence. For this, knowledge-driven modelling can be applied together with mathematical data-driven modelling to produce a mineral potential map.

5.1. Evidential Belief for mapping mineral potential

The Dempster-Shafer evidential belief function theory is based on work on the generalization of Bayesian lower and upper probabilities. The lower and upper probabilities represent the belief and plausibility respectively, in which a particular proposition is supported by a given body of evidence (Shafer, 1976). The functions, belief and plausibility can be interpreted as probabilities in the traditional probabilistic framework (Chang-Jo and Fabbri, 1993; An *et al.*, 1994a). The following discussion of EBFs is adopted from the explanations of Carranza and Hale (2003).

The EBFs are *Bel* (degree of belief), *Dis* (degree of disbelief), *Unc* (uncertainty) and *Pls* (plausibility). *Bel* and *Pls* represent lower and upper probabilities respectively, that spatial evidence supports the proposition (Figure 5.1). Thus, *Pls* is greater than or equal to *Bel*. *Unc* is equal to *Pls-Bel* and represents doubt of ones belief in the proposition based on a given spatial evidence; *Unc* = 0 when *Bel* = *Pls*. *Dis* on the other hand is belief that proposition is false based on a given spatial evidence which is equal to 1-*Pls.* Therefore, the addition of *Bel, Dis* and *Unc* is equal to one (Bel+Dis+Unc=1). In addition, if *Bel*=0, then *Dis* should be equal to zero; this indicates that there is no disbelief with out belief, but there can only be uncertainty. If *Unc* =0 then *Bel*+*Dis* = 1, as in probability approach. Functions at *Bel*, *Unc*, and *Dis* are the EBFs used to combine spatial evidences according to Dempster's rule (Dempster, 1968).

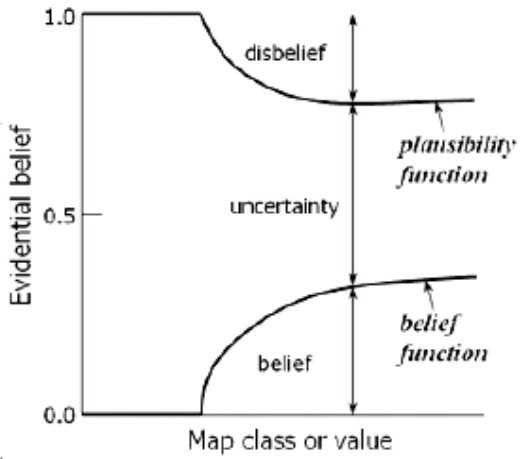

Figure 5-1 Schematic relationships of EBFs (adopted from Carranza and Hale, 2003).

Estimation of EBFs can either be knowledge-driven or data driven. Knowledge-driven estimation of EBSs requires expert knowledge of the proposition being evaluated. When expert knowledge is lacking, EBFs can be estimated based on given spatial data described by Chung and Fabri (1993) and An and Bonham Carter (1994) (Chang-Jo and Fabbri, 1993; An *et al.*, 1994a) When location of both mineralized and unmineralized zones are known data driven estimation procedures of Chung and Fabri, (1993) and An *et al.*, (1994) are useful (Chang-Jo and Fabbri, 1993; Chung and Fabbri, 1993; An *et al.*, 1994b). When locations of mineralized and unmineralized zones are only partially known, data-driven estimation procedures proposed by Carranza and Hale, 2003 is useful. This procedure is adopted for the study area.

Assume a spatial evidence map of an area T with N (T) total number of pixel. It is necessary to first determine the spatial coincidence between certain pixels in a map of training data (mineral occurrences) and certain pixel in a map of spatial evidence. To do this attributes of spatial evidence maps Xi(i=1,2,….,n) representing continuous variables must be first classified into C_{ij}(j=1,2,…,m) classes of attribute. By overlaying binary map of training data on each multi-class spatial evidence map, the number of C_{ij} pixel overlapping spatially with mineral deposit D pixels [i.e., $N(C_{ij})\cap N(D)$] and number of C_{ij} pixels not overlapping spatially with D pixels [ie., $N(C_{ij})$-$N(C_{ij} \cap D)$] can be determined.

According to Carranza and Hale, (2003), EBF's can be estimated as follows: The degree of belief, $BelC_{ij}$, that a mineral deposit exists, is

$$Bel_{C_{ij}} = \frac{W_{C_{ij}D}}{\sum_{j=1}^{m} W_{C_{ij}D}} \qquad \textit{(Eq.1)}$$

$$\text{where } W_{C_{ij}D} = \frac{\frac{N(C_{ij} \cap D)}{N(C_{ij})}}{\frac{N(D) - N(C_{ij} \cap D)}{N(T) - N(C_{ij})}}. \qquad \textit{(Eq.1a)}$$

Where the numerator is the conditional probability that a target mineral deposit exists given the presence C_{ij}; that means a target mineral deposit occurs in C_{ij}. The denominator is the conditional probability that a target mineral deposit exists given the absence of C_{ij}; meaning a target mineral deposit occurs outside C_{ij}. Thus, Wc_{ijD} is the weight of C_{ij} in terms of target mineral deposits being more present than absent in C_{ij} as may be expected due to chance.

A weight $WC_{ij}\bar{D}$ for C_{ij} in data set *D* for the proposition *Dis* (disbelief that a mineral deposit exists based on *D)* is defined as:

$$Dis_{C_{ij}} = \frac{W_{C_{ij}\overline{D}}}{\sum_{j=1}^{m} W_{C_{ij}\overline{D}}} \qquad \textit{(Eq.2)}$$

$$\text{where } W_{C_{ij}\overline{D}} = \frac{\frac{N(C_{ij}) - N(C_{ij} \cap D)}{N(C_{ij})}}{\frac{N(T) - N(D) - [N(C_{ij}) - N(C_{ij} \cap D)]}{N(T) - N(C_{ij})}}. \qquad \textit{(Eq.2a)}$$

Where the numerator is the conditional probability that a target mineral deposit does not exist given the presence of C_{ij}; it means simply that a target mineral deposit does not occur in C_{ij}. The denominator is the conditional probability that a target mineral deposit does not exist given the absence of C_{ij}; that is a target mineral deposit does not occur outside attribute C_{ij}. Thus, $WC_{ij}\bar{D}$ is the weight of C_{ij} in terms of target mineral deposits being more absent than present in C_{ij} as may be expected due to chance.

For data driven estimation of belief and disbelief (Equation 1 and 2), demonstrated by Carranza and Hale (2003), the spatial relationship between classes of layers of an evidential map should be taken into consideration besides the spatial relationship between evidential layer and target deposit.

Note that, if for C_{ij} calculated $Wc_{ij}D=0$, which means that $Belc_{ij} = 0$, then the corresponding calculated WC_{ij} should be re-set to zero so that the corresponding $DisC_{ij}=0$ according to (Figure 5-1).

$$Uncc_{ij}=1-Belc_{ij}-Disc_{ij} \quad (Eq.3)$$

$$Plsc_{ij}= Belc_{ij} + Uncc_{ij} \text{ or } Plsc_{ij} =1- Disc_{ij} \quad (Eq.4)$$

Maps of EBFs of spatial evidence Map X_1 can be combined with maps of EBFs of spatial evidence mapX_2 according to Dempster's (1968) rule of combination in order to generate an integrated map of EBFs. The formula for combining maps of EBFs of two spatial evidence maps are the following ((Carranza and Hale, 2003), adopted from Wright and Bonham-Carter, 1996):

$$Bel_{X_1X_2} = \frac{Bel_{X_1}Bel_{X_2} + Bel_{X_1}Unc_{X_2} + Bel_{X_2}Unc_{X_1}}{\beta} \quad (Eq.5)$$

$$Dis_{X_1X_2} = \frac{Dis_{X_1}Dis_{X_2} + Dis_{X_1}Unc_{X_2} + Dis_{X_2}Unc_{X_1}}{\beta} \quad (Eq.6)$$

$$Unc_{X_1X_2} = \frac{Unc_{X_1}Unc_{X2}}{\beta} \quad (Eq.7)$$

Where $\beta=1-Belx_1Disx_2-Disx_1Belx_2$, which is a normalizing factor to ensure that *Bel+Unc+Dis=1*. Only maps of EBFs of two spatial evidence can be combined each time; other maps of EBFs representing $X_2,\ldots.X_n$ are combined one after another by repeated applications of Eq.5-7. Final combination of maps of EBFs results in integrated degree of belief, degree of disbelief, degree of uncertainty and degree of plausibility for the proposition based on given spatial evidences

5.2. Deposit recognition criteria and spatial datasets

The Magondi Belt is a known source of metamorphosed, stratabound, sediment-hosted Cu-Ag deposit (Master, 2003). The rocks of the Magondi Belt were deposited in the Magondi Basin. The Deweras, Lomagundi, and Piriwiri Groups are the major sedimentary rocks deposited between c.2.16 and 2.0 Ga (Woldai *et al.*, 2006). The evolution of the Magondi Basin between these ages, and the deposition of the sediments are shown in Figure 2.8, section 2.5. The Deweras Group is the major host rock of strata-bound copper mineralization. The sediments were deposited in continental alluvial fan, aeolian dune, flat, lacustrine fan-delta and playa lake environments (Master, 2003). Mineralization was formed diagenetically by saline basin (Master, 1998; Master, 2003; Woldai *et al.*, 2006). Ore mineralizations consist of disseminated bornite and chalcopyrite in wackes and arkosic granulestones, and chalcocite-bornite and chalcopyrite in anhydrite-barite bearing rock (Master, 2003). Zonation of the sulphides along strike and from top to bottom of the ore bodies occur from bornite to bornite-chalcopyrite to chalcopyrite and pyrite. The mineralizing fluids probably originated as reduced basin brines that evolved into oxidizing brines through reaction with sulphate evaporites. The evolved brines, carrying Cu and Ag (leached from red beds) as chloride complexes, moved along the permeable footwall granule stones and precipitated sulphides on encountering the reduced wackes. Some mineralizations are in the form of replacements of digenetic pyrite nodules.

Basic igneous rock, metadolerite sill, intruded the sediments containing the ore zones. The sill contained xenoliths of the host rock. Axial planar fractures in the competent sill filled with Cu-sulphide-bearing quartz-carbonate-microcline-hematite/magnetite veins that originated by pressure solution in the mineralized wall rock metasediments. Some of these veins are up to 2 m thick and were mined together with the disseminated sedimentary ore (Master, 2003).

The distribution of silver in the Norah deposit is closely associated with mineralization of copper. Mineralogically, silver occurs as both solid solution in bornite and chalcocite, and as native silver in concentrated diagenetic pyrites (Master, 2003). Reddish hematite alteration accompanied by silicification and microclinization of arkosic arenites, is the characteristic feature of the footwall of ore bodies (Carballo Lopez, 1998). According to Carballo Lopez, 1998, these zones have ellipsoidal concentrations and bands of magnetite.

Folding, fracturing and boudinage of earlier veins together with emplacement of new veins accompanied later deformation events, the last of which is dated at 548 ± 140 Ma (Master, 2003). The anticlinal axis, N-S and NW-SE faults are associated with mineralization (Carballo Lopez, 1998; Kambewa, 1998; Woldai *et al.*, 2006). The ore deposit around Norha, has been severely tectonised, and is intensely disrupted by wrench, normal and thrust faults of various ages.

Based on the above characteristic features of strata-bound, sediment hosted Cu-Ag deposit of the research area; the following geological conceptual model can be summarized:

- The major host rock for Cu mineralization is arkose, which is permeable enough to pass mineralizing fluids and allow precipitation in the reduced environment. Anhydrite and thinly bedded anhydrite-bearing dolomite in Norha Formation of the Deweras Group, (Section 2.3.3), probably acted as a reducing agent during mineralization.
- NW-SE faults could be pathways for the mineralizing fluids (Carballo Lopez, 1998; Kambewa, 1998).
- The magnetic anomaly map which interpreted the host rock could also indicate fracture filled magnetic minerals such as magnetite and pyrrhotite in the mineralized zone.
- Geochemical anomalies obtained from soil samples taken from the overlaying host rock, could be considered as indicator of mineralization.

Based on the recognition criteria mentioned above, spatial evidences were selected from southern parts of the study area (Figure 5.2). This area is the only area where high resolution aeromagnetic survey was conducted and 99% of the known Cu deposits occur. Lithological units and NW trending faults were extracted from updated geological map (Figure 5.2a and Figure 5.2b). The interpreted analytical signal total field magnetics was taken as magnetic anomaly map (Figure 5.2c). Interpolated PC4 scores, calculated on Alaska and Umboe datasets (Figure 5.2d) were considered as geochemical anomaly map.

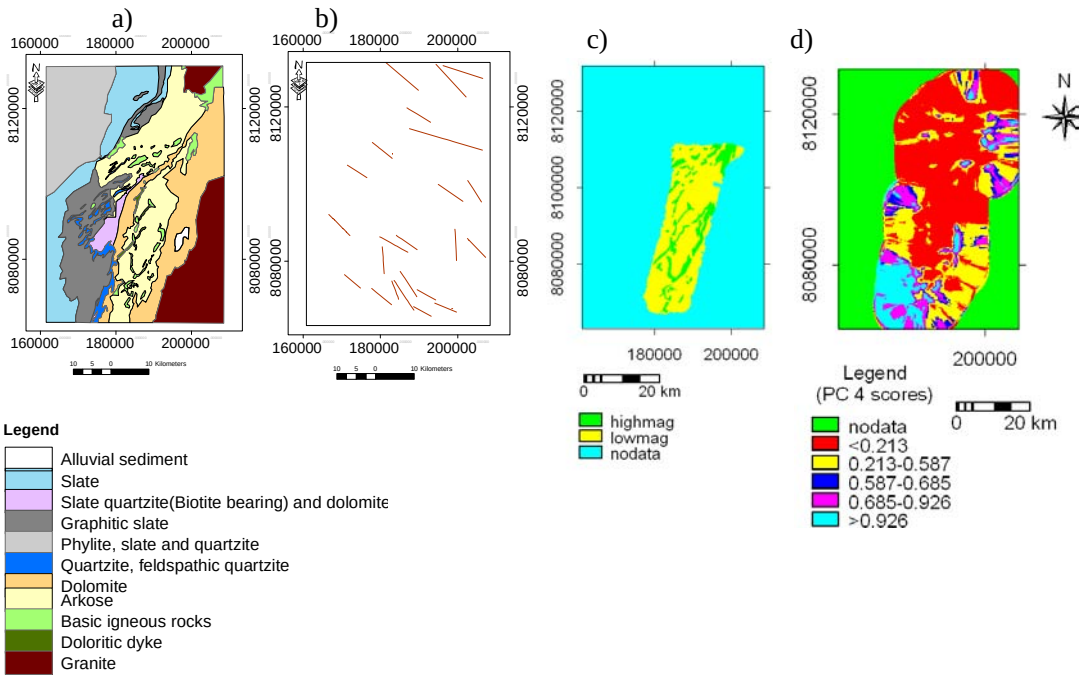

Figure 5-2 Spatial evidence maps a) lithological units, b) NW fault, c) magnetic anomaly map and d) PC4 score representing concentration of Cu in Alaska and Umboe area; UTM Zone 36S projection, WGS 84 Datum.

5.3. Estimation and integration of EBFs

Spatial evidence maps representing continuous variables were first classified using percentile intervals of values. Areas which have no values were reclassified as "no data". The resulting multiclass spatial evidential maps were crossed with binary map of known copper deposit. The number of class pixels N (C_{ij}), sum of all class pixels N (T), number of class pixels that overlap with deposit pixels (N ($C_{ij} \cap D$) and total number of deposit pixels N (D) were first calculated (Table 5.1). EBFs estimation based on equations in section 5.1 (Equations 1-3) were performed to quantify the spatial association between the deposit and spatial evidences (Table 5.1).

Based on the values calculated on Table 5.1, attribute maps of EBFs are created. The created belief functions; belief, disbilief and uncertanity maps of lithological units, magnetic anomaly, PC4 scores and proximity to NW faults are shown in Figure 5.3-6. Only arkose, dolomite and granite have spatial association with Cu deposits. Zones of high degree of belief are mainly related to lithological units of arkoses and dolomite. (Figure 5.3). These rocks have low degree of disbelief and uncertainty as compared with the other units. This suggests that presence of these lithologic units can be used as indicator of potential areas for copper mineralization. Zones of high degree of belief, low degree of disbelieve and uncertainties are belonging to areas underlain by high magnetic anomalies (Table 5.1 and Figure 5.4). Areas occupied by high PC4 score (>0.926) corresponds to high degree of belief, low degree of disbelief and uncertainty (Table 5.1 and Figure 5.5). This suggests geochemical anomalous areas of copper are more prospective to find strata bound copper mineralization provided that the other recognition criteria are fulfilled. High degree of belief is also related to proximity class of NW fault between 0.00- 790m (Table 5.1 and Figure 5.6). This indicates the possible potential zone within this distance.

The belief function maps of strata-bound copper mineralization were integrated by repeated use of Equation 5.7, Section 5.1. The combined evidential belief function maps estimate new belief function maps representing the degree of belief, disbelief, uncertainity and plausibility (Figure 5.7A-D). The plausibility map was created by using Equation 4 (Figure 5.7). Spatial evidences representing, belief functions of lithology, PC4 scores and NW fault were first integrated and the results were compared with further integration with magnetic anomaly map. The belief and plausibility maps show potentially favourable zones.

5.3.1. Test of correctness of EBFS

Test of correctness conducted on EBFs maps indicate that sum of bel+dis+unc for most pixels is 1.00. The pixel values in the test map vary from 1.000 to 1.0001 for all four evidential maps. The test conducted on the integrated EBFs map indicate values 0.9998 to 1.0001 (Figure 5.7E). This suggests that error for the estimation and integration of EBFs is ± 0.0003 which can be considered as very low and therefore, estimation and integration of EBFs can be considered to have been performed properly.

Table 5-1 Estimation of EBFs for class of values in maps of deposit recognition criteria for strata bound Cu-Ag potential, Magondi Belt. (EBFs of PC scores are calculated in descending order.

Lithological units	***N(Cij)***	***N(T)***	***N(Cij∩D)***	***N(D)***	***Bel***	***Dis***	***Unc***
Alluvial sediment	1228	330031	0	19	0	0	1
Arkose	71602	330031	10	19	0.53	0.33	0.1411
Basic igneous rocks	5814	330031	0	19	0	0	1
Dolomite	53113	330031	6	19	0.32	0.33	0.3526
Doloritic dyke	549	330031	0	19	0	0	1
Granite	45744	330031	3	19	0.15	0.33	0.5163
Graphitic slate	39161	330031	0	19	0	0	1
No data	10217	330031	0	19	0	0	1
Quartzite, feldspathic quartzite	6751	330031	0	19	0	0	1
Quartzite, phylite, slate	47980	330031	0	19	0	0	1
slate	41930	330031	0	19	0	0	1
Slate quartzite(Biotite bearing) and dolomite	5942	330031	0	19	0	0	1
Magnetic anomaly map	***N(Cij)***	***N(T)***	***N(Cij∩D)***	***N(D)***	***Bel***	***Dis***	***Unc***
High magnetic anomaly	11737	330031	2	19	0.55	0.33	0.1158
Low magnetic anomaly	46042	330031	5	19	0.38	0.33	0.2874
No data	272252	330031	12	19	0.06	0.33	0.6068
Score of PCA/geochemical anomaly	***N(Cij)***	***N(T)***	***N(Cij∩D)***	***N(D)***	***Bel***	***Dis***	***Unc***
No data	132045	330031	2	19	0.02	0.2	0.7789
<0.213	98972	330031	7	19	0.16	0.2	0.6368
0.213-0.587	49585	330031	5	19	0.24	0.2	0.5579
0.587-0.685	9861	330031	0	19	0	0	1
0.685-0.926	19808	330031	2	19	0.22	0.2	0.5792
>0.926	19760	330031	3	19	0.35	0.2	0.4472
Proximity to NW fault/fracture (km)	***N(Cij)***	***N(T)***	***N(Cij∩D)***	***N(D)***	***Bel***	***Dis***	***Unc***
No data	1	330031	0	19	0	0	1
0.00-0.793	32708	330031	4	19	0.22	0.14	0.6395
0.793-1.529	32965	330031	2	19	0.1	0.14	0.7636
1.529-2.265	32386	330031	1	19	0.05	0.14	0.8136
2.265-3.020	33704	330031	3	19	0.15	0.14	0.7101
3.020-3.794	32509	330031	1	19	0.05	0.14	0.8138
3.794-4.627	33083	330031	3	19	0.15	0.14	0.7069
4.627-5.633	33514	330031	5	19	0.29	0.14	0.5726
5.633-6.969	32729	330031	0	19	0	0	1
6.969-9.389	33230	330031	0	19	0	0	1
9.389-21.799	33202	330031	0	19	0	0	1

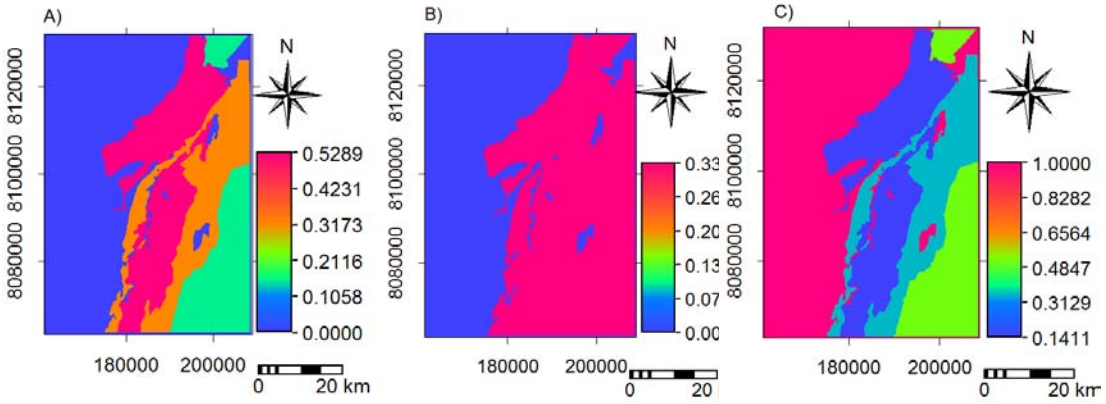

Figure 5-3 Attribute map of EBFs for lithological unit classes A) belief map B) disbelief map and C) uncertainty map, UTM Zone 36S projection, WGS 84 Datum.

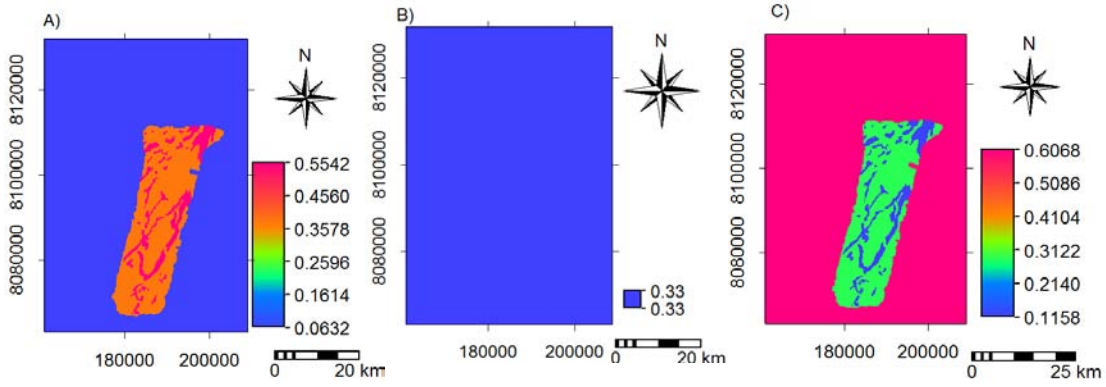

Figure 5-4 Attribute maps of EBFs for magnetic anomaly classes A) belief map B) disbelief map and C) uncertainty map, UTM Zone 36S projection, WGS 84 Datum.

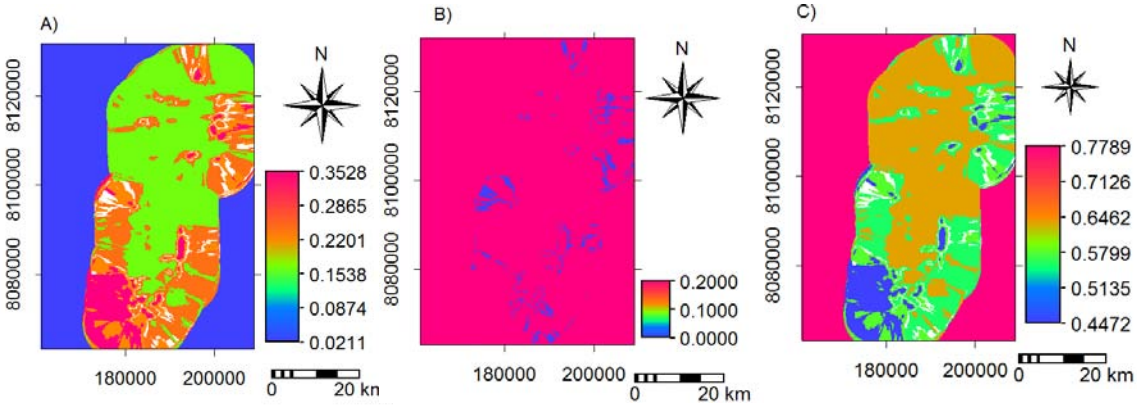

Figure 5-5 Attribute map of EBFs for pc scores classes A) belief map B) disbelief map and C) uncertainty map, UTM Zone 36S projection, WGS 84 Datum.

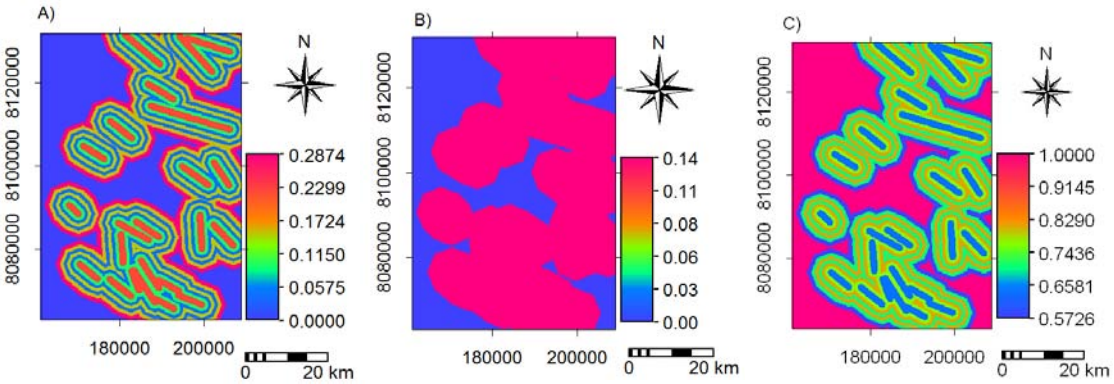

Figure 5-6 Attribute maps of EBFs for proximity to NW fault classes A) belief map B) disbelief map and C) uncertainty map, UTM Zone 36S projection, WGS 84 Datum.

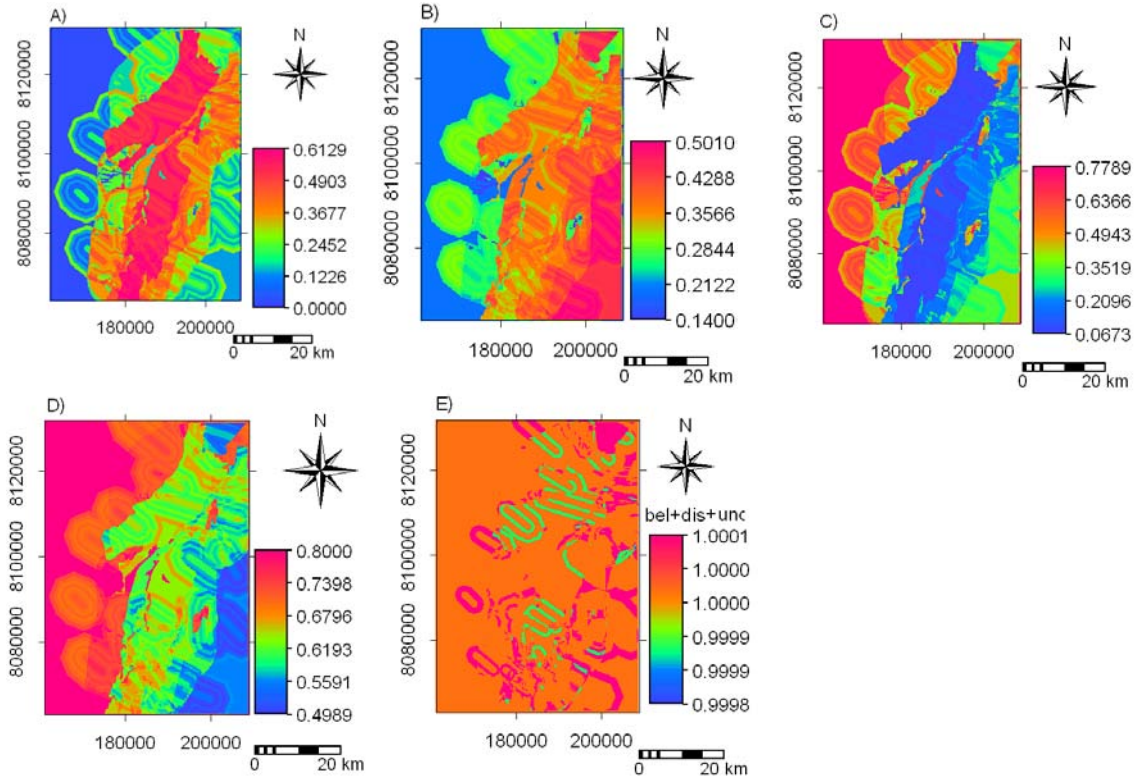

Figure 5-7 Integrated EBFs maps of strata-bound Cu potential showing A) belief map; B) disbelief map; C) Uncertainty map and D) plausibility map, E) Test of correctness of estimation and integration of EBFs. UTM Zone 36S projection, WGS 84 Datum. (bel=belief, dis=disbelief, unc=uncertainty)

5.4. Classification and validation of mineral potential map

The integrated belief maps without evidence of magnetic anomaly was first used to generate stratabound copper potential map. Integrated map with evidences of magnetic anomaly was then produced to compare the results. A threshold probabilities were defined to convert the belief maps

into favourability of mineral potential map. Percentile values 50, 75, 90 and 100% were used to classifay the integrated belief map into low, moderate, high and very high potential. Here the approperate threshold values 80th percentile were used to classifay zones which are geologically favourable and unfavourable zones for strata-bound copper mineralization. The classified potential maps were further classified in to binary favourability maps (Figure 5.8). The favorability map without evidences of magnetic anomaly outlined potential zones for for strata bound copper mineralization in the central parts of the study area (Figure 5.8A). The classified map with evidences of magnetic anomaly strengthen the first classification and identified more potential zones within the boundaries of magnetic anomaly (Figure 5.8B). About 4.68 and 4.98% of the total area were classified without and with magnetic anomaly map in favopurable potential zone for strata-bound mineralization, respectively (Table 5.2).

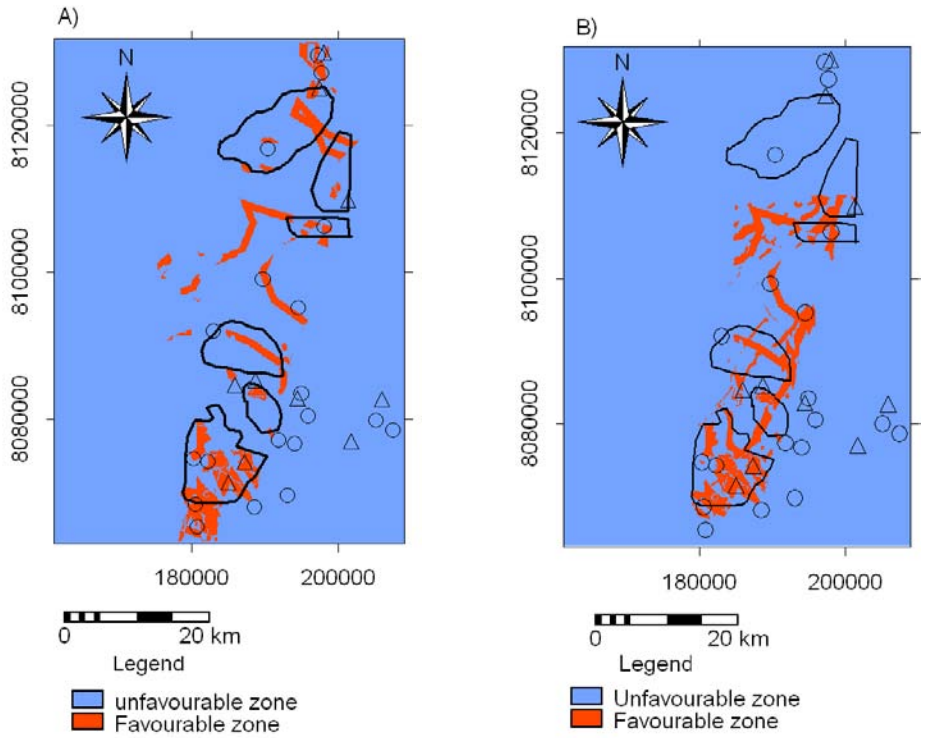

Figure 5-8 Predictive map of strata-bound copper deposit potential A) using spatial evidences lithology, PC4 and NW fault B) using all spatial evidences including magnetic anomaly. Small circles and triangles represent locations of large and small scale known Cu deposits and occurrences used in training and validation data respectively; polygons represent geochemical Cu-anomaly zones, Magondi Belt, UTM Zone 36S projection, WGS 84 Datum

The favorability copper potential map were crossed with known copper deposits and occurrences to determine number of validation deposit pixels in the favourable zones. The result indicates that at least 58% and 31% of known Cu deposit pixels in potential map without magnetic and with magnetic evidences are correctly delineated by the predicted geologically favourable zones, respectively (Table 5.2). Prediction rate was also calculated based on validation data of small scale copper deposits and occurrences, which were not used in EBFs. The result indicate that 60% and 40% of the deposits are correctly delineated by the favourable zones without and with magnetic anomaly, respectively (Table

5.3). of the out of 10 small scale deposits of potential map without magnetics and 4 out ofcoincide with the predicted potential zone. This implies, 60%

Table 5-2 Validation of predictive strata-bound copper potential map using Known Cu deposit, South Magondi-Belt

Classified potential map without magnetic anomaly	Proportion of potential zone %	Number of Known Cu-deposit used as training data Total =19	Success rate %
Unfavourable zone (without)	95.32	8	42
Favourable zone (without)	4.68	11	58
Unfavourable zone (with)	95.02	13	68.5
Favourable zone (with)	4.98	6	31.5

Table 5-3 Validation of predictive strata-bound copper potential map using small scale Cu deposit/occurrences, South Magondi-Belt

Classified potential map with and with out magnetic anomaly	Number of small scale deposit used as validation data Total =10	prediction rate %
Unfavourable zone (without)	4	40
Favourable zone (without)	6	60
Unfavourable zone (with)	6	60
Favourable zone (with)	4	40

The predictive map crossed with geochemical soil copper anomally indicates that at least 12% and 19% of the geochemical anomaly zones are overlapped with the favourable potential zones without and with magnetic anomaly, respectively (Table 5.4).

Table 5-4 Validation of predictive strata-bound copper potential map using geochemical soil Cu anomaly, South Magondi-Belt

Classified potential map	geochemical Cu anomaly Total npix=1714	prediction rate %
Unfavourable zone (without)	1510	88
Favourable zone (without)	204	12
Unfavourable zone (with)	1383	81
Favourable zone (with)	331	19

5.5. Summary of spatial data integration for predictive modeling of mineral potential

Evidential belief function using data driven approach has provided a good result in mapping strata-bound copper potential of the research area. To predict where mineral deposits of interest might occur, it is necessary to study spatial association between known deposit occurrences and certain geological features that control their occurrence. GIS-based predictive modeling such as evidential belief functions (EBFs), involves analysis of spatial associations between multi-layered geological features and known deposit occurrences to predict where deposits of interest are likely to occur.

A total of 19 copper mineral deposits were used in the predictive mapping of mineral potential. EBFs function, belief, disbelief and uncertainties were created for spatial evidences of lithologic units, proximity to NW faults, magnetic and geochemical anomalies. Among the lithologic units, arkose and dolomite are important spatial evidence of strata-bound Cu potential. The linear structure, NW trending faults/ fractures are also the most significant spatial evidence of mineral potential. The magnetic anomaly and the geochemical soil Cu anomaly PC4 scores (>0.926) have similar spatial evidence to the copper potential. From the integrated belief functions map, it can be seen that zones of intermediate to high degree belief, low degree of disbelief and intermediate to low degree of uncertainty, areas are underlain by arkoses and dolomite. These rocks are host rocks of the strata-bound Cu mineralization in the study area (Carballo Lopez, 1998; Kambewa, 1998; Master, 2003; Woldai *et al.*, 2006). The plausibility map also indicates high degree, indicating potentially mineralized areas. On the classified binary predictive mineral potential map, with magnetic anomaly evidences, the proportion of favourability zone increased by 0.3%. This implies that integration and classification of evidential maps with magnetic anomaly map improves potentially favourable zone for strata-bound Cu deposit. Favourability zones in the central and northern parts of the area are characterized by high degree of belief and low degree of uncertainty of evidences of proximity classes

of NW faults. One of the known large scale mine, Norah, in the north is situated on this fault line probably indicating structurally controlled mineralization (Carballo Lopez, 1998; Kambewa, 1998; Master, 2003). Zones of high degree of belief, low degree of disbelief and low degree of uncertainty of evidences of anomalous geochemical signature provide a strong support to high favourable zone in the southern parts of the area. This area is contact zone underlain by arkose, basic igneous rocks and dolomite, which contain folds and faulted structures. Test conducted on integrated EBFs map indicated that error for the estimation and integration of EBFs is ± 0.0003, which can be considered as very low and, therefore, estimation and integration of EBFs can be considered to have performed properly.

Validations conducted on the binary predictive map without magnetic anomaly evidence indicates that the favourable potential zone correctly delineate 12% of the Cu-anomaly, 58% of the 'model' deposits and 60% of the 'validation' deposit. Validations conducted on binary predictive map with magnetic anomaly evidence indicates that the favourable potential zone correctly delineate 19% Cu anomaly map, 31.5% of the 'model' deposits and 40% of the 'validation' deposit. The result implies that the binary potential map with magnetic anomaly evidence map improves the proportion of favourability zone as compared to the binary map without magnetic anomaly. This indicates a satisfactory result which implies the usefulness of the model for further exploration of undiscovered strata-bound copper deposit in the northern parts of the study area.

6. Conclusion and Recommendation

6.1. Conclusion

Spatial data processing, analysis and integration using remote sensing and GIS applications were useful in updating the geological map and predicting mineral potential map of the study area. During the processes of image interpretation, old geological maps were used as a base map to extract information on major lithologic units. Multispectral image enhancement and interpretations were important in identifying and delineating lithological units including host rocks for strata-bound mineralization in the study area. Image classifications were also helped in mapping major lithologic units. ASTER image better classified the lithologic units as compared with Landsat TM. The low classification accuracy on both images were probably due to similarities in rock units, extensive soil cover, vegetation and topography, which made the surface feature spectrally less separable. The high resolution aeromagnetic data were help in identifying geologic features on areas where extensive soil covers occur. Analytical signal and vertical derivatives of total field magnetics were helped in extracting subsurface information to delineate host rocks and structural features, which are responsible for mineralization. DEM generated from ASTER and SRTM images were used in extracting major geological structures associated with mineralization. The NW-SE faults were found an important spatial evidence for Cu mineralization. Images fused with DEM were helped in further enhancing and increased interpretation of geological features. Integration of all interpreted images helped in classifying lithologic units and updates the geological map of the study area. The geological map was validated and a total accuracy of 76% was obtained.

Geochemical data processing and interpretation of principal component analysis were helpful in identifying anomalous zones for strata-bound Cu-Ag-Au mineralization in the study area. Scores of principal component (PC4) were used as one of evidential maps in predicting mineral potential of the study area. Large scale known Cu deposit map were used in quantifying the spatial associations between the deposit and geological features.

The theory of EBFs for mineral potential mapping was found to be the best method to predict mineral potential map of the study area. Deposit recognition criteria were the basis for extracting spatial evidences based on the characteristic features of strata-bound Cu-Ag-Au mineralization in the study area and elsewhere in similar regions. Data driven approach were used to quantify the spatial association between the known mineral deposit and geological features in Magondi Belt. A total of 19 copper mineral deposits were used in the predictive mapping of mineral potential. EBFs function, belief, disbelief and uncertainties were created for spatial evidences of lithologic units, proximity to NW faults, magnetic and geochemical anomalies. Among the lithologic units, arkose and dolomite were found to be important spatial evidence of strata-bound Cu-Ag-Au potential. These rocks are host rocks of the strata-bound Cu mineralization in the study area. EBFs maps containing spatial evidence were integrated to produce favourability map. Test conducted on integrated EBFs map indicated that error for estimation and integration of EBFs is ± 0.0003, which can be considered as

very low and, therefore, estimation and integration of EBFs can be considered to have performed properly. The total area predicted under favourability zone in predictor maps with and without magnetic anomaly is 4.98% and 4.68% respectively. This indicates that the binary potential map with magnetic anomaly evidence could improve the proportion of favourability zone. Validations conducted on the binary predictive map without magnetic anomaly evidence indicates that the favourable potential zone correctly delineate 12% of the Cu-anomaly, 58% of the 'model' deposits and 60% of the 'validation' deposit. Validations conducted on binary predictive map with magnetic anomaly evidence also indicate that the favourable potential zone correctly delineate 19% the Cu anomaly, 31.5% of the 'model' deposits and 40% of the 'validation' deposit. This indicates a satisfactory result which implies the usefulness of the model for further exploration of undiscovered strata-bound copper deposit in the northern parts of the study area where similar evidences occur.

6.2. Recommendation

- The predictive model has indicated potential areas in the southern parts of Magondi Belt. Similar techniques are recommended for the northern area of the belt where same spatial evidences occur.
- High resolution aeromagnetic data has found to map subsurface geological features and improve the prediction of strata-bound Cu potential zone. This survey is recommended in the northern parts of the area to map subsurface geology in soil covered area and predict potential areas for strata-bound Cu mineralization.
- The Piriwiri Group rocks reported to host massive sulphide deposit. Application of theory of Evidential Belief (EBFs) is recommended to predict such type of mineralization in the research area.

7. Reference

An, P., Moon, W., and Bonham-Carter, G. (1994a) An object-oriented knowledge representation structure for exploration data integration. *Natural Resources Research*, **3**, 132-45.

-. (1994b) Uncertainty management in integration of exploration data using the belief function. *Natural Resources Research*, **3**, 60-71.

Andrada de Palomera, R.P. (2004) Application of remote sensing and geographic information systems for mineral predictive mapping, deseado massif, southern Argentina, p. 73. ITC, Enschede.

Arnold Ivan Johnson, C.B.P., James L. Fulton. (1992) *Geographic information systems (GIS) and mapping- practices and standards*. 348 p. ASTM International.

Beus, A.A., and Grigorian, S.V. (1977) *Geochemical exploration methods for mineral deposits*. 287 p. Applied Publishing, Wilmette.

Bonham-Carter, G.F. (1994) *Geographic information systems for geoscientists: Modelling with GIS*398 p. Pergamon, Kidlington etc.

Bounessah, M., and Atkin, B.P. (2003) An application of exploratory data analysis (eda) as a robust non-parametric technique for geochernical mapping in a semi-arid climate. *Applied Geochemistry*, **18**, 1185-95.

Carballo Lopez, E. (1998) Integration of aeromagnetic thematic mapper and geochemical data for mineral exploration in the makonde district, Zimbabwe, p. 107. ITC, Delft.

Carranza, E.J.M., and Hale, M. (2002) Mineral imaging with landsat thematic mapper data for hydrothermal alteration mapping in heavily vegetated terrane. *International Journal of Remote Sensing*, **23**.

-. (2003) Evidential belief functions for data - driven geologically constrained mapping of gold potential, Baguio district, Philippines. *In: Ore Geology Reviews, 22(2003)1-2, pp. 117-132*.

Carranza, E.J.M., Mangaoang, J.C., and Hale, M. (1999) Application of mineral exploration models and gis to generate mineral potential maps as input for optimum land use planning in the philippines. *In: Natural Resources Research, 8(1999)2, pp. 165-173*.

Chang-Jo, F.C., and Fabbri, A.G. (1993) Representation of geoscience information for data integration. *In: Nonrenewable Resources, (1993), pp. 122-139.*

Chavez, P.S.e., Marino, C.M.e., and Schowengerdt, R.A.e. (1994) *Recent advances in remote sensing and hyperspectral remote sensing : 27 - 29 september 1994, rome*. 238 p. The International Society for Optical Engineering (SPIE), Bellingham.

Chung, C.-J., and Fabbri, A. (1993) The representation of geoscience information for data integration. *Natural Resources Research*, **2**, 122-39.

Crôsta, A.P., and Rabelo, A. (1993) Assessing of landsat tm for hydrothermal alteration mapping in central western brazil *Proceedings of Ninth Thematic conference geologic remote sensing Pasadinea*, p. 1053-61, California, USA.

Dempster, A.P. (1968) Generalization of bayesian inference. *In: Journal of the royal statistical society, series B, 30(1968), pp. 205-247*.

Foody, G.M., and Mathur, A. (2004) Toward intelligent training of supervised image classifications: Directing training data acquisition for svm classification. *Remote Sensing of Environment*, **93**, 107-17.

Fraser, S.J., and Green, A.A. (1987) A software defoliant for geological analysis of band ratios. *International Journal of Remote Sensing*, **8**.

Govett, G.J.S. (1976) *Rock geochemistry in mineral exploration*. 461 p. Elsevier, Amsterdam etc.

Hahn, L. (2002) On the stratigraphy of the palaeoproterozoic deweras and lomagundi groups (magondi supergroup) in zimbabwe. *South African Journal of Geology*, **105**, 193-204.

Harris, J.R., Sanborn, M., Panagapko, D.A., Skulski, T., and Parker, J.R. (2006) Gold prospectivity maps of the red lake greenstone belt: Application of gis technology *Source: Candaian Journal of Earth Science*, **43** 865-93.

Hewson, R.D., Cudahy, T.J., Mizuhiko, S., Ueda, K., and Mauger, A.J. (2005) Seamless geological map generation using aster in the broken hill-curnamona province of australia. *Remote Sensing of Environment*, **99**, 159-72.

Isabirye Mugaddu, E. (2005) Integration of various remotely sensed data for geological mapping in the jinja area, uganda, p. 101. ITC, Enschede.

Jones, R.R., McCaffrey, K.J.W., Clegg, P., Wilson, R.W., Holliman, N.S., Holdsworth, R.E., Imber, J., and Waggott, S. (2006) Integration of regional to outcrop digital data: 3d visualisation of multi-scale geological models. *Computers & Geosciences*, In Press, Accepted Manuscript.

Kalinowski, A., and Oliver, a.S. (2004) Aster mineral index processing manual. *Geoscience Australia*.

Kambewa, C. (1998) Use of gis in exploration for sediment hosted copper deposits in the makonde basin, zimbabwe, p. 168. ITC, Delft.

Le Thi Chau, H. (2001) Integrating landsat etm7, aerial photographs and field data for geological mapping : The tabernas basin, southeast spain, p. 61. ITC, Enschede.

Lillesand, T.M., and Kiefer, R.W. (1987) *Remote sensing and image interpretation*. 721 p. Wiley & Sons, New York etc.

Lips, A.L.W., Lawrence, C., Rowan, John, and Mars, C. (2002) Lithologic mapping in the mountain pass, california area using advanced spaceborne thermal emission and reflection radiometer (aster) data

Majaule, T., Hanson, R.E., Key, R.M., Singletary, S.J., Martin, M.W., and Bowring, S.A. (2001) The magondi belt in northeast botswana: Regional relations and new geochronological data from the sua pan area. *Journal of African Earth Sciences*, **32**, 257-67.

Master, S. (1991) The origin and controls on the distribution of copper and precious metal mineralization at the mhangura and norah mines, **Phd**, p. 382. Witwatersrand university South Africa

-. (1998) Mineral deposits studies group meeting, university of greenwich, 5-6 january *New developments in understanding the origin of the Central African Copperbelt*, University of Greenwich.

-. (2003) Norah mine, zimbabwe: A polydeformed and metamorphosed stratabound cu-ag deposit. In J.G. (RAU), H.H. (AARL), and C.M. (RAU), Eds. *Mineralogy and Geochemistry of Base Metal Deposits in Southern Africa – Implications for Exploration and Beneficiation*, p. 56, RAU, Auckland Park, South Africa.

Master, S., Ferraz, M.F.F., Woldai, T., and Zeil, P. (1996) Gis integration of data from the magondi copperbelt and the highbury meteorite impact structure in zimbabwe. *In: Conf. on the application of remotely sensed data and GIS in environmetal and natural resources assessment in Africa, Harare, Zimbabwe, March 15-22, 1996, pp 151-154.*

Master, S., Henry, G., and Borg, G. (1989) Geochemistry and mineralogy of banded iron-formation-hosted gold mineralization in the gwanda greenstone-belt, zimbabwe - a discussion. *Economic Geology*, **84**, 194-7.

Munyanyiwa, H., and Maaskant, P. (1998) Metamorphism of the palaeoproterozoic magondi mobile belt north of karoi, zimbabwe. *Journal of African Earth Sciences*, **27**, 223-40.

Owusu, E.A., Woldai, T., Barritt, S.D., Carranza, E.J.M., and Hale, M. (2006) Spatial association of gold deposits with remotely - sensed faults, south ashanti belt, ghana. *In: AARSE 2006 : Proceeding of the 6th AARSE international conference on earth observation and geoinformation sciences in support of Africa's development, 30 October - 2 November 2006, Cairo, Egypt. Cairo : The National Authority for Remote Sensing and Space Science (NARSS), 2006. ISBN 1-920-01710-0. 8 p.*

Porwal, A.K., Hale, M.p., and Carranza, E.J.M.p. (2006) Mineral potential mapping with mathematical geological models. *ITC Dissertation;130*, p. 289. ITC, Enschede.

Ranjbar, H., Shahriari, M., and Honarmand. (2003) Comparison of aster and etm+ data for exploration of porphyry copper mineralization: A case study of sar cheshmeh areas, kerman, iran.

Reimann, C., and Filzmoser, P. (2000) Normal and lognormal data distribution in geochemistry: Death of a myth. Consequences for the statistical treatment of geochemical and environmental data. *Environmental Geology*, **39**, 1001-14.

Reimann, C., Filzmoser, P., and Garrett, R.G. (2005) Background and threshold: Critical comparison of methods of determination. *Science of The Total Environment*, **346**, 1-16.

Ren, Dianwei, ABDELSALAM, and Mohamed, G. (2001) Optimum, index factor (oif) for aster data: Examples from the neoproterozoic allaqi suture. *The Geological Society of America (GSA)*

Rigol, J.P., and Chica-Olmo, M. (1998) Merging remote-sensing images for geological-environmental mapping: Application to the cabo de gata-níjar natural park, spain. *Environmental Geology*, **34**, 194-202.

Sabins, F.F. (1987) *Remote sensing : Principles and interpretation*. 449 p. W.H. Freeman, New York.

Schetselaar, E.M. (1998) Fusion by the ihs transform : Should we use cylindrical or spherical coordinates. *International Journal of Remote Sensing*, **19**.

-. (2006) Geological data integration. *ILWIS application*, Enschede, The Netherlands.

Shafer. (1976) A mathematical theory of evidence. 297.

Stagman, J.G. (1978) *An outline of the geology of rodesia*. 126 p. Salisbury, Kidlington etc.

Surveyor-General. (1985) Provisional geological map of zimbabwe : 1:1.000.000 : Africa. Suryveyor-General, Government of Zimbabwe, Salisbury.

Telford, W.M., Geldart, L.P., and Sheriff, R.E. (1990) *Applied geophysics*. 770 p. Cambridge University Press, Cambridge.

Thurmond, A.K., Abdelsalam, M.G., and Thurmond, J.B. (2006) Optical-radar-dem remote sensing data integration for geological mapping in the afar depression, ethiopia. *Journal of African Earth Sciences*, **44**, 119-34.

Treloar, P.J. (1988) The geological evolution of the magondi mobile belt, zimbabwe. *Precambrian Research*, **38**, 55-73.

van der Meer, F.D. (2006) Remote sensing and gis techniques applied to geological survey. *ILWIS application*, Enschede, The Netherlands.

van Genderen, J.L., and Pohl, C. (1994) Image fusion of optical and microwave satellite data for earth sciences applications. *In: UN, CINA, ESA workshop on microwave remote sensing aplications, Beijing, China, 14-18 September 1994, pp. 1-7*.

van Roij, A. (2006) *Integration of airborne geophysical data and spaceborne multispectral data for geological mapping and mineral potential mapping in a poorly exposed region : A case study of the kibi area, ghana*. 126 p. Utrecht University (UU), ITC, Utrecht,Enschede.

Woldai, T., Pistocchi, A., and Master, S. (2006) Validation and sensitivity analysis of a mineral potential model using favourability functions. *In: Applied GIS, 2(2006)1, art.2 19 p.*

Yusta, I., Velasco, F., and Herrero, J.M. (1998) Anomaly threshold estimation and data normalization using eda statistics: Application to lithogeochemical exploration in lower cretaceous zn-pb carbonate-hosted deposits, northern spain. *Applied Geochemistry*, **13**, 421-39.

Appendices

Appendix A Frequency histograms and box-plots of elements in Magondi Belt (als=Alaska, umb=Umboe, mha=Mahangura and sha=Shamrock)

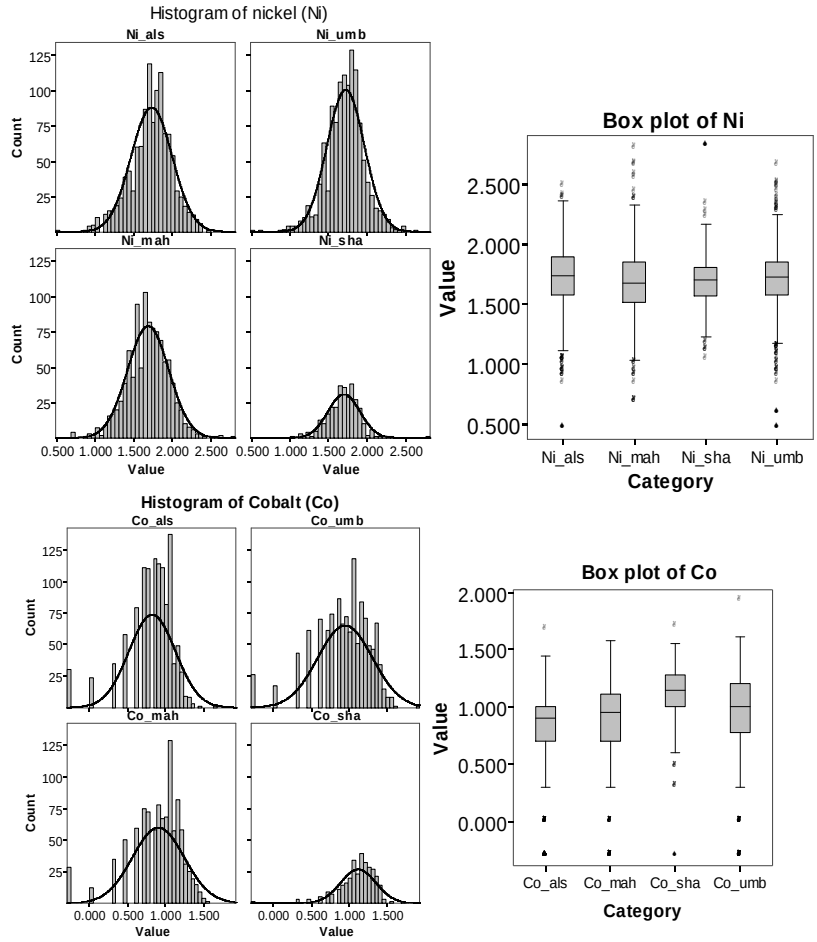

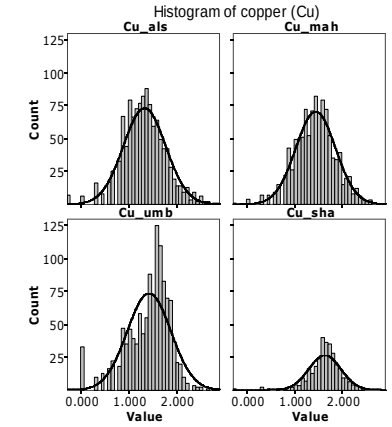
Histogram of copper (Cu)
Cu_als
Cu_mah
Cu_umb
Cu_sha
Count
Value

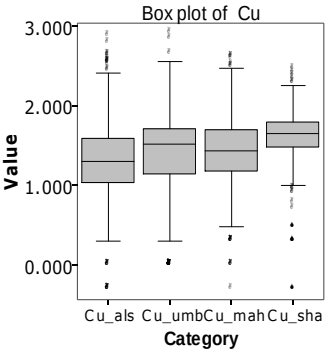
Box plot of Cu
Value
Cu_als
Cu_umb
Cu_mah
Cu_sha
Category

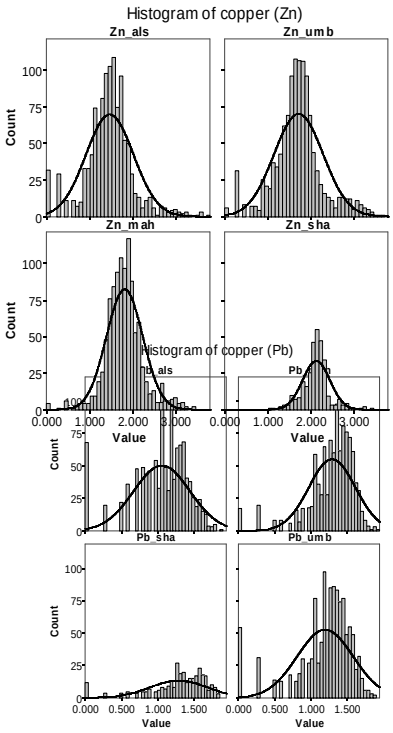
Histogram of copper (Zn)
Zn_als
Zn_umb
Zn_mah
Zn_sha
Histogram of copper (Pb)
Pb_als
Pb_mah
Pb_sha
Pb_umb
Count
Value

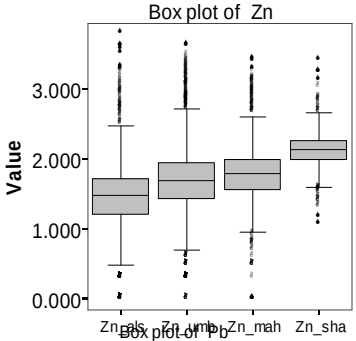
Box plot of Zn
Value
Zn_als
Zn_umb
Zn_mah
Zn_sha
Category

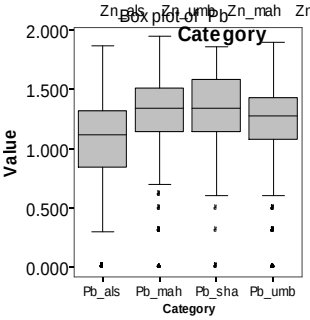
Box plot of Pb
Value
Pb_als
Pb_mah
Pb_sha
Pb_umb
Category

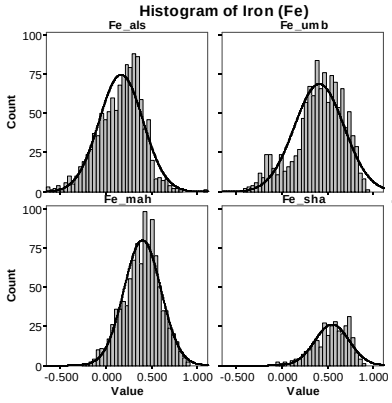
Histogram of Iron (Fe)
Fe_als
Fe_umb
Fe_mah
Fe_sha
Count
Value

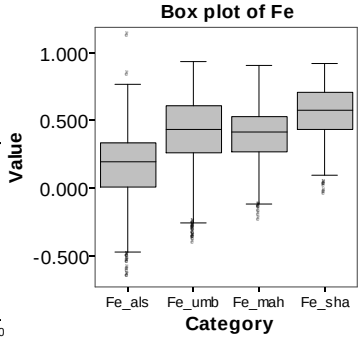
Box plot of Fe
Value
Fe_als
Fe_umb
Fe_mah
Fe_sha
Category

Appendix B Field observation dataset

observ_pt	X_Coordinate	Y_Coordinate	Observation/ Rock_name	Strik_Dip of foliation	Geologic Structure	Mine
200	177335.4852	8185241.602	Biotite and hornblend para gneiss	60w/40		
221	178744.2261	8186024.568	Biotite and hornblend para gneiss	80/30		
222	180037.6628	8186873.501	Biotite and hornblend para gneiss	52/74		
223	180484.7084	8181004.988	Biotite and hornblende para gneiss			Shamrock_mine
225	184879.8922	8168100.681	Granite			
226	182178.411	8168246.988	Granite			
227	188955.4083	8167835.872	Granite	64/52		
228	186706.5774	8170036.25	Granite			
229	183896.0571	8168110.938	Granite			
230	189612.1949	8170026.858	Granite			
231	192401.6793	8165177.266	Granite			
232	191741.598	8163230.323	Granite			
233	188469.0343	8171848.376	Basic igneous rocks	37/52		
234	189575.8536	8172912.243	Granite			
235	192255.7421	8176140.27	Granite	70/45		
236	188492.9267	8161624.514	Granite			
237	190407.8172	8162075.595	Granite	45w/50		
238	189713.2375	8159321.502	granite	60w/48		
239	187231.3514	8158548.216	phyllite	60w/78		
240	190776.6774	8155073.936	Phylite	40w/45		
241	192650.3858	8155141.833	Arkose	45w/75		
241	194042.0354	8150303.978	arkose		anticline	
243	181287.298	8103085.204	Arkose	66/60		
245	182154.0808	8104549.722	Arkose	48/58		
665	183537.6245	8104717.376	basic igneous rocks		syncline	
754	183016.3142	8101804.315	Graphitic slate	15/83		
976	186621.9559	8097946.381	Doloritic dyke	37/52		
775	186621.9228	8097946.401	Doloritic dyke	543/87		
887	188798.3015	8101714.186	Dolomite	75/18		
932	192662.1893	8104690.554	Dolomite	24/10		
512	188707.8236	8102447.654	Arkose	60/40		
654	187141.922	8107095.637	Basic igneous rocks	57/53		
110	188608.2312	8107091.802	Basic igneous rocks	52/72		
731	190670.123	8107095.392	Arkose	72/28		
553	192662.1963	8104690.519	Dolomite	24/10		
676	191938.759	8108128.631	Basic igneous rocks	37/50		
432	194217.0599	8109061.347	Arkose	80/44		
188	194791.239	8110628.212	Arkose	83/17		
1001	193008.052	8110334.711	arkose		syncline	
511	191870.3826	8090021.259	Arkose	28/58		
988	191870.4042	8090021.298	Arkose	28/85		
289	191701.5888	8089001.89	Basic igneous rocks	28/80		
523	188689.0243	8085142.901	Arkose			Avondale_mine
779	185882.3066	8084563.811	Arkose			Shaklton_mine
659	194703.7194	8082156.876	Dolomite	45/75		

239	183140.7584	8079497.75	Arkose		anticline	
712	183501.947	8078259.123	Arkose	38/82		
899	182319.5141	8077757.359	Arkose	48w/33		
550	181628.6593	8078064.634	Arkose			
190	181589.916	8079149.352	Arkose	52/25		
268	182887.7687	8082738.554	Doloritic dyke		anticline	
194	182714.1724	8083663.091	Arkose	42/22		
366	194633.9609	8078957.419	Dolomite	45/80		
1020	191434.9408	8077062.818	Dolomite		anticline	
656	193236.0785	8077492.866	Dolomite	45/85		
440	190061.9432	8074671.538	Arkose	45/80		
428	187257.7292	8074024.682	Arkose			Angwa_mine
6280	185032.8833	8071282.588	Arkose			Hans_Mine
773	184696.9334	8075528.248	arkose		syncline	
419	183597.9022	8074021.625	Basic igneous rocks	58/83		
1002	192721.9104	8124492.716	Slate	38/45		
122	192458.3745	8118634.855	Arkose	60		
1030	197346.932	8124979.026	Arkose			Norah_Mine
2825	203138.4184	8123059.882	Basic igneous rocks	25		
1216	206580.3789	8124569.788	Dolomite		syncline	
1830	203898.8831	8117542.693	Dolomite		syncline	
2725	205304.1243	8116994.37	Dolomite		syncline	
335	201338.8978	8109748.25	Dolomite			United_Kingdom
871	197190.8375	8111923.67	Basic igneous rocks	70/66		
980	199827.0981	8096574.438	Dolomite		syncline	
621	198434.8294	8092895.428	Dolomite		syncline	
1200	196253.0636	8088415.278	Dolomite		syncline	
1919	196905.073	8087609.658	Dolomite		syncline	
634	197637.6448	8087596.21	Dolomite		syncline	
436	202290.8447	8078623.756	Granite			Chinhoyi
774	198121.7973	8130458.429	Arkose			Mhangura_Mine
284	195167.6377	8141204.321	Basic igneous rocks	31/84		
659	194087.8378	8141304.124	Arkose	35/70		
301	179200.1649	8089200.348	Slate quartzite(Biotite bearing) and dolomite			
447	183112.0668	8087805.405	Arkose	32/60		
987	188638.2248	8108222.451	Arkose	73		
661	192587.4735	8115912.706	Arkose		anticline	
671	194619.6116	8118153.202	Arkose		anticline	
2003	195137.3635	8112124.321	Arkose		anticline	
805	183551.9954	8082702.078	Doloritic dyke			
979	170524.4564	8090784.49	Quartzite, feldspathic quartzite			
3054	177394.3731	8082641.187	Quartzite, feldspathic quartzite			
2836	181784.3705	8105389.439	Quartzite, feldspathic quartzite			
1040	182593.627	8102431.476	Quartzite, feldspathic quartzite			
5459	177904.1661	8094396.676	Quartzite, feldspathic quartzite			
4064	185668.9662	8107390.906	Arkose			
551	170234.6583	8096647.043	Graphitic slate			
2854	195425.9632	8103208.877	Dolomite			

3300	197415.4367	8106461.234	Arkose			
440	188056.4943	8113247.38	Arkose			
117	192642.3067	8123734.719	Slate			
752	182219.7194	8108112.247	Arkose			
337	183295.0024	8157147.695	Slate			
1028	190189.7925	8170425.154	Granite			
1022	199059.0661	8169755.761	Granite			
180	203695.5304	8191420.89	Biotite and hornblend para gneiss			
999	203580.4129	8157973.13	Meta-ultramafic rock with serpentinite or talc			
1016	175137.221	8163121.373	Phyllite			
2823	197791.4365	8132865.952	Arkose			
892	196240.998	8139133.608	Basic igneous rocks			
541	197309.4312	8143733.964	Basic igneous rocks			
3390	197309.4312	8143733.964	Basic igneous rocks			
645	197309.4312	8143733.964	Basic igneous rocks			
782	191704.5359	8153230.21	Arkose			
893	193575.0597	8165282.556	Granite			
566	186218.9276	8171941.241	Basic igneous rocks			
671	172566.9818	8137241.898	Phylite, slate and quartzite			
1101	168936.4625	8107134.232	Phylite, slate and quartzite			
80	174033.5685	8155333.059	Slate			
430	179696.4277	8163722.48	Arkose			
54	185149.5513	8138344.481	Slate			
870	187876.1131	8117993.216	Graphitic slate			
7550	192280.5591	8130373.605	Graphitic slate			
9870	181374.3119	8153234.777	Graphitic slate			
32	163546.7924	8151137.422	Phylite			
930	163756.5279	8173579.123	Phylite			
81	167741.5028	8163302.082	Granite			
900	186617.7	8123452.333	Graphitic slate			
553	205703.6327	8066364.916	Granite			
422	202977.0708	8091323.444	Granite			
6650	207381.5169	8097825.245	Granite			
6630	169419.387	8069114.522	Graphitic slate			
554	165434.4121	8066597.696	Slate			
5550	164385.7344	8088619.926	Slate			
4300	193538.9723	8198962.558	Grits, sandstone etc			
59	181793.7829	8198752.822	Grits, sandstone etc			
71	185569.0224	8174627.677	Basic igneous rocks			
2987	175501.7172	8126380.043	Phylite, slate and quartzite			
5400	166692.8252	8126380.043	Phylite, slate and quartzite			
19	166483.0897	8142949.149	Granite			

Field observations a) Location of sample point; b) Dip and strike of foliations, anticline and synclines.